



Electromagnetic methods in
geothermal exploration.
1D and 3D inversion of TEM and
MT data from a synthetic
geothermal area and the Hengill
geothermal area, SW Iceland.

Guðni Karl Rosenkjær



Faculty of Earth Sciences
University of Iceland
2011

ELECTROMAGNETIC METHODS IN
GEOTHERMAL EXPLORATION.1D AND 3D
INVERSION OF TEM AND MT DATA FROM A
SYNTHETIC GEOTHERMAL AREA AND THE
HENGILL GEOTHERMAL AREA, SW ICELAND.

Guðni Karl Rosenkjær

60 ECTS thesis submitted in partial fulfillment of a
Magister Scientiarum degree in Geophysics

Advisor
Knútur Árnason

Faculty Representative
Páll Einarsson

Examiner
Leó Kristjánsson

Faculty of Earth Sciences
School of Engineering and Natural Sciences
University of Iceland
Reykjavik, May 2011

Electromagnetic methods in geothermal exploration. 1D and 3D inversion of TEM and MT data from a synthetic geothermal area and the Hengill geothermal area, SW Iceland.
Electromagnetic methods in Geothermal exploration
60 ECTS thesis submitted in partial fulfillment of a M.Sc. degree in Geophysics

Copyright © 2011 Guðni Karl Rosenkjær
All rights reserved

Faculty of Earth Sciences
School of Engineering and Natural Sciences
University of Iceland
Sturlugata 7
101, Reykjavik, Reykjavik
Iceland

Telephone: 525 4000

Bibliographic information:

Guðni Karl Rosenkjær, 2011, Electromagnetic methods in geothermal exploration. 1D and 3D inversion of TEM and MT data from a synthetic geothermal area and the Hengill geothermal area, SW Iceland., M.Sc. thesis, Faculty of Earth Sciences, University of Iceland.

ISBN XX

Printing: Háskólaprent, Fálkagata 2, 107 Reykjavík
Reykjavik, Iceland, May 2011

Abstract

The TEM (Transient Electro Magnetic) and MT (MagnetoTelluric) methods are commonly used in geothermal exploration. The resistivity structure of the geothermal systems may be used to gain information about the temperature and other attributes of interest. Measurements have traditionally been inverted in 1D, but advances in multidimensional inversion enable routine 3D inversions of MT data in geothermal exploration.

The main objectives of this study is to investigate the inversions done for geothermal exploration. Special attention is given to the problem of static shift, that arises in MT soundings when there is inhomogeneous surface resistivity. Both synthetic data from a synthetic geothermal system with different varying surface resistivity and real data from the Hengill geothermal area are used. For all the data, joint 1D inversions of the TEM and MT data and 3D inversions of MT data without and with static shift correction, are done. The resulting models for all the inversion are compared and the results are discussed in terms of the effectiveness of the methods.

The results reveal that 3D models of the resistivity interpolated from joint 1D inversion of TEM and MT data, recover near surface resistivity structure fairly well but at depth become inaccurate. Models from 3D inversion fare better overall, recovering resistivity structures with good accuracy at all depths. The difference of models from 3D inversion of MT without and with static shift correction, is not great but correcting the static shift prior to inversion results in somewhat better models. The setup of the inversion is shown to play an important role in the resulting models. Using a different mesh and/or selecting different frequencies affects the resolution, time and the details of the inversion. It is therefore crucial to be critical of the inversion results and test the results with multiple inversions and/or forward modeling before interpretation.

Útdráttur

TEM og MT mælingar eru gjarnan notaðar við jarðhitarannsóknir. Unnt er að nota viðnáms gerð jarðhitakerfa til að fá upplýsingar um hitastig og aðrar áhugaverða eiginleika kerfisins. Í gegnum tíðina hafa mælingar verið túlkaðar með einvíðum líkanareikningum en framfarir í margvíðri úrvinnslu gerir það nú kleift að nota þrívíða líkanareikninga reglubundið við túlkun á gögnum við jarðhitarannsóknir.

Megin markmið þessa verkefnis er að rannsaka líkanareikinga sem er gjarnan notaðir við jarðhitarannsóknir. Sérstaklega er skoðuð hliðrunaráhrif í MT mælingum, sem kemur upp vegna margvíðanleika viðnáms nálægt yfirborði. Notuð eru gögn framreiknuð frá gervilíkönnum af jarðhitasvæði með mismunandi viðnámi nærri yfirborði og frá jarðhitasvæðinu í Henglinum. Öll gögnin eru túlkuð með sameiginlegum einvíðum líkanareikningum TEM og MT mælinganna og þrívíðum líkanareikningum MT mælinga án og með leiðréttingu á hliðrunaráhrifunum. Módelin frá þessum mismunandi líkanareiknum eru borin saman og niðurstöður ræddar með hliðsjón af gæðum aðferðanna.

Niðurstöður sýna að þrívíð módel brúuð frá niðurstöðum einvíðra líkanareikninga TEM og MT mælinga, endurskapa nokkuð vel viðnámsgerðina nærri yfirborði en ónákvæmni verður vart með auknu dýpi. Módel frá þrívíðum líkanareikningum endurskapa viðnámsgerð á öllu dýpi með góðri nákvæmni. Munur milli módela án og með leiðréttingu á hliðrunaráhrifum í MT mælingum er ekki mikill, en líkanareikningar þar sem hliðrunaráhrifin eru leiðrétt leiða af sér svolítið betri módel. Uppsetning á líkanareikningunum hefur áhrif á niðurstöðurnar. Ef annað líkan er notað og/eða aðrar tíðnir valdar, hefur það áhrif á upplausn, tímann og nákvæmni líkanareikninganna. Það er því mikilvægt að vera gagnrýnin á niðurstöðurnar og staðfesta endursköpuðu viðnámsgerðina með mismunandi líkanareikningum og/eða framreikningum áður en niðurstöðurnar eru túlkaðar.

Contents

List of Figures	ix
List of Tables	xiii
Acknowledgments	xv
1 Introduction	1
2 Theory of Electromagnetic methods	3
2.1 EM theory	3
2.1.1 Maxwell's equations	3
2.1.2 Boundary conditions	4
2.2 MT method	6
2.2.1 Overview	6
2.2.2 Electromagnetic waves in conductive medium	7
2.2.3 MT solution in horizontally layered earth	10
2.2.4 Impedance tensor	13
2.2.5 Rotation and combinations of impedance tensor	17
2.2.6 Dimensionality measures	18
2.2.7 Real data processing	19
2.3 TEM method	22
2.3.1 Overview	22
2.3.2 The central-loop TEM	24
2.3.3 TEM solution in a horizontally layered earth	25
2.3.4 Solution for central loop TEM	27
3 Near surface induced Electromagnetic distortion	29
3.1 Static shift problem	29
3.1.1 Voltage distortion	29
3.1.2 Current distortion	31
3.1.3 Topographic distortion	32
3.2 Correction of static shift	33
3.3 Use of TEM for static shift estimations in geothermal exploration . .	37
4 Modeling of Electromagnetic data	39
4.1 Inversion of geophysical data	39

4.2	Forward and inverse modeling codes used	40
4.2.1	1D TEM and MT inversion code - TEMTD	40
4.2.2	3D TEM forward code - H3DTD	42
4.2.3	3D MT forward code - MT3Dfwd	44
4.2.4	MT 3D inversion code - MT3Dinv	46
5	Geothermal exploration with Electromagnetic methods	49
5.1	Resistivity structure of geothermal systems	49
5.2	Application of EM methods	51
5.3	Instruments and field setup	53
6	Synthetic geothermal model	55
6.1	Model design	55
6.2	Work procedure	58
6.2.1	Domain discretization	59
6.2.2	Forward modeling and error assignment	60
6.2.3	1D inversion	61
6.2.4	3D inversion	63
6.3	Results of inversion modeling	64
6.3.1	Model with homogeneous surface resistivity	64
6.3.2	Gaussian distributed surface resistivity	72
6.4	Investigation of the inversion	78
6.4.1	Domain discretization	78
6.4.2	Frequency selection	80
6.5	Discussion of inversion results	82
7	Hengill geothermal area	85
7.1	Overview of the Hengill geothermal area	85
7.1.1	Geology	85
7.1.2	Previous geophysical work	87
7.2	Setup of inversions	88
7.2.1	TEM and MT data	88
7.2.2	Joint 1D inversion	89
7.2.3	3D inversion	90
7.3	Inversion results	91
7.3.1	1D inversion models	91
7.3.2	3D inversion models without static shift correction	96
7.3.3	3D inversion models with static shift correction	101
7.4	Discussion of inversion results	106
8	Conclusion	111
	Bibliography	115

List of Figures

2.1	MT setup	7
2.2	Central loop TEM setup	23
3.1	Voltage over homogeneous domains	30
3.2	Voltage distortion in an inhomogeneous space	31
3.3	Current channeling for inhomogeneous conductivity.	32
3.4	Topographic distortion of electric fields.	33
3.5	Comparison of 1D inversion results of static shifted data.	34
3.6	Determinants of static shifted data.	35
5.1	Figure of general resistivity and alteration	50
6.1	Iso-elevation maps of the synthetic geothermal model.	56
6.2	Cross sections of the synthetic geothermal model.	57
6.3	Surface resistivity of 2 models used.	58
6.4	Location of TEM and MT soundings for synthetic models	61
6.5	Joint 1D inversion results for a sounding.	62
6.6	Real part of xy data from joint 1D inversion for synthetic model with homogeneous surface resistivity.	65

LIST OF FIGURES

6.7	Real part of xy data from 3D inversion for synthetic model with homogeneous surface resistivity, no static shift correction.	66
6.8	Real part of xy data from 3D inversion for synthetic model with homogeneous surface resistivity, static shift corrected.	67
6.9	Maps of xy and yx static shift multipliers for a synthetic geothermal system with homogeneous surface resistivity.	68
6.10	Iso-elevation maps comparing the results of inversion models from Section 6.3.1.	69
6.11	W-E cross sections comparing the results of inversion models from Section 6.3.1.	70
6.12	S-N cross sections comparing the results of inversion models from Section 6.3.1.	71
6.13	Real part of xy data from joint 1D inversion for synthetic model with Gaussian distributed surface resistivity.	72
6.14	Real part of xy data from 3D inversion for synthetic model with Gaussian distributed surface resistivity, no static shift correction. . .	73
6.15	Real part of xy data from 3D inversion for synthetic model with Gaussian distributed surface resistivity, static shift corrected.	73
6.16	Maps of xy and yx static shift multipliers for a synthetic geothermal system with Gaussian distributed surface resistivity.	74
6.17	Iso-elevation maps comparing the results of inversion models from Section 6.3.2.	75
6.18	Cross sections comparing the results of inversion models.	76
6.19	Cross sections comparing the results of inversion models.	77
6.20	Cross sections comparing the results of inversion models for different meshes	79
6.21	Cross sections comparing the results of inversion models for different selection of frequencies.	82

7.1	Topographic map of the Hengill area, with geological surface features	86
7.2	Contour map of the Hengill area, showing MT sounding and cross section location	89
7.3	Iso-elevation maps of 1D inversion results Hengill.	92
7.4	S-N cross sections of 1D inversion results.	93
7.5	W-E cross sections of 1D inversion results.	94
7.6	Real part of xy data from joint 1D inversion for the Hengill area. . .	95
7.7	Iso-elevation maps of 3D results for Hengill, without a static shift correction.	96
7.8	S-N cross sections of 3D results for Hengill, without a static shift correction.	97
7.9	W-E cross sections of 3D results for Hengill, without a static shift correction.	98
7.10	Real part of xy data from 3D inversion for the Hengill, without static shift correction.	99
7.11	Maps of xy and yx static shift multipliers for a synthetic geothermal system with homogeneous surface resistivity.	101
7.12	Iso-elevation maps of 3D results for Hengill, with a static shift correction.	102
7.13	W-E cross sections of 3D results for Hengill, with a static shift correction.	103
7.14	S-N cross sections of 3D results for Hengill, with a static shift correction.	104
7.15	Real XY data from 3D inversion for the Hengill, with static shift correction.	105
7.16	Comparison of observed and predicted data of the different inversion procedures, for sounding 0682721.	106
7.17	W-E cross section at 7103 Northing (km) comparing the results of inversion for Hengill.	107

LIST OF FIGURES

7.18 S-N cross section at 484 Easting (km), comparing the results of inversion models for Hengill.	108
7.19 Iso-elevation maps comparing inversion models for Hengill.	109

List of Tables

6.1 The elevation to the top, bottom and the resistivity for the layers used in the design of synthetic geothermal system. 55

6.2 Relationship of mesh size and computation time. The smallest cell, total number of cells in the inversion and the computational time are listed for all the meshes used for the inversion of the models in Figure 6.20. 78

6.3 Skin depth for the new and the original frequencies. Skin depths are calculated using Equation 2.46 for a 22 Ω m homogeneous resistivity. . 81

Acknowledgments

First, my family and friends deserve a lot of gratitude for all the support and patience that they have given me during this study. Without all this, the work would not have been possible.

I would like to thank the supervisors of my studies, Knútur Árnason, head of Geophysics at Iceland Geosurvey, and Dr. Páll Einarsson, professor in geophysics at University of Iceland. Their help and guidance has been valuable for my studies and this project.

Iceland Geosurvey (ISOR) and all the employees there get thanks for support and helpfulness with any issue arising. Gylfi Páll Hersir, Hjálmar Eysteinnsson and Ragna Karlsdóttir receive special gratitude for their patience and willingness to develop my understanding of geophysics and geothermal exploration. Beyond everybody else at ISOR, I want to thank Arnar Már Vilhjálmsson for his friendship, office sharing and all his help.

I would like to extend gratitude to Dr. Doug Oldenburg and others at the Geophysical Inversion Facility at University of British Columbia, for allowing the use of the codes for this study. The welcomeness and the facility I was provided with has made a big difference for the result of this work. Justin Granek and Dave Marchant, receive special thanks for their assistance and suggestions to improve this thesis.

This work was partly funded by a grant from Orkuveita Reykjavík Environmental and Energy Fund.

1 Introduction

The TEM (Transient Electro Magnetic) and MT (Magnetotelluric) methods are commonly used in geothermal exploration. The methods give valuable information where the resistivity structure of the geothermal systems may be connected to temperature and other attributes that are of interest. Traditionally measurements have been inverted in 1D, recovering resistivity models only varying with depth. The 1D inversion models have then been stitched together for measurements along an intersecting line, mapped at a constant elevation or interpolated into a 3D volume to give spatial information about the area. Development of multidimensional inversion algorithms and increased computer capabilities now enable routine 3D inversions of MT data in geothermal exploration. With the MT method, the problem of static shift arises due to inhomogeneous surface structures. The most common way to deal with this problem is to use a TEM sounding made in close proximity of the MT sounding to rectify the effects of the static shift in the MT sounding.

The goal of the study is to use TEM and MT algorithms developed by the Geophysical Inversion Facility at the University of British Columbia and Iceland Geosurvey to investigate inversions of these data. Data from a synthetic geothermal system and the Hengill geothermal area in Iceland will be inverted.

The goals may be categorized as

1. Discuss the problem of static shift in MT data.
2. Compare results from joint 1D inversion of TEM and MT data to 3D inversion of MT, for both synthetic and real data.
3. Investigate the effects of static shift correction to results of 3D inversion, using static shift multipliers estimated from 1D inversion to correct the MT data prior to 3D inversion.

Theoretical basis of the MT and TEM methods is discussed in Chapter 2. Solution of the MT waves in a horizontally layered earth, the concepts of impedance and apparent resistivity are derived in detail. As well, some of the steps that are necessary in processing of real data are discussed. An overview of the derivation of the TEM method is given. In Chapter 3 the problem of EM distortion, in particular the static shift problem is discussed. The different causes of the static shift and proposed

1 Introduction

methods of correction are given. Special focus is given to using TEM soundings for static shift correction of MT data as this is the common practice in geothermal exploration.

In Chapter 4 an overview of a inversion procedure is given followed by more specific descriptions of the forward and inversion codes used in this study. The resistivity structure of geothermal systems is discussed in Chapter 5, covering geologic procedures that affect the resistivity of the rocks. The application of EM methods in geothermal exploration, common instruments and their setup are also covered.

In Chapter 6 the inversion of TEM and MT data generated from a synthetic geothermal system is discussed. To test and compare the effects of static shift on MT inversion, a homogeneous and Gaussian distributed surface resistivities are considered on simple synthetic geothermal models. The designs of the models, the generation of the synthetic data and setup of the inversions are discussed first. The results of the joint 1D inversion of TEM and MT data and 3D inversions of MT data, without and with static shift correction prior to the inversions. The affects of using different meshes and frequencies is illustrated and a discussion of the results is given.

In Chapter 7 the inversions of TEM and MT data from the Hengill geothermal area are discussed. Overviews of the geology and previous work in the area are given. The setup of the inversions are discussed, followed by results of the joint 1D inversion of TEM and MT data and 3D inversions of the MT data, without and with static shift correction. The results are compared and discussed. Finally, the thesis concludes with summary and conclusion of this study in Chapter 8.

2 Theory of Electromagnetic methods

2.1 EM theory

2.1.1 Maxwell's equations

The fundamental equations of electromagnetic theory are Maxwell's equations. For a conductive medium, they are expressed as:

$$\nabla \times \mathbf{E} = -\frac{\partial \mathbf{B}}{\partial t} \quad (2.1a)$$

$$\nabla \times \mathbf{H} = \mathbf{J} + \frac{\partial \mathbf{D}}{\partial t} \quad (2.1b)$$

$$\nabla \cdot \mathbf{B} = 0 \quad (2.1c)$$

$$\nabla \cdot \mathbf{D} = q \quad (2.1d)$$

where \mathbf{B} is the magnetic flux density $[T]$, \mathbf{H} is the magnetic field $[Am^{-1}]$, \mathbf{D} is the electric displacement field $[Cm^{-2}]$, \mathbf{E} is the electric field $[Vm^{-1}]$, q is an electrical charge density $[Cm^{-3}]$ and \mathbf{J} is the electric current density $[Am^{-2}]$.

For an isotropic medium, the fields and fluxes described in Equations 2.1 have been shown to be linked by *constitutive relationships*:

$$\mathbf{B} = \mu \mathbf{H}, \quad \mathbf{D} = \epsilon \mathbf{E} \quad \text{and} \quad \mathbf{J} = \sigma \mathbf{E} \quad (2.2)$$

where σ is the electrical conductivity in $[Sm^{-1}]$, μ is the magnetic permeability $[Hm^{-1}]$ and ϵ is the electric permittivity $[Fm^{-1}]$. In the earth, σ , μ and ϵ vary with position, describing the properties of the material the EM wave is propagating

through. Commonly magnetic permeability and electric permittivity are given as

$$\mu = \mu_r \mu_0 \quad \text{and} \quad \epsilon = \epsilon_r \epsilon_0 \quad (2.3)$$

where $\mu_0 = 4\pi \cdot 10^{-7} \text{ H m}^{-1}$ and $\epsilon_0 = 8.85 \cdot 10^{-12} \text{ F m}^{-1}$ are the magnetic permittivity and dielectric permittivity of vacuum, respectively. μ_r and ϵ_r are dimensionless multipliers connecting material properties to those of vacuum.

2.1.2 Boundary conditions

Equations 2.1 govern how EM waves travel in a uniform medium. From them it is possible to derive the behavior of the fields at the boundaries between media with different electrical properties. Lets consider a boundary between two media, 1 and 2, with electrical properties as $\sigma_1, \mu_1, \epsilon_1$ and $\sigma_2, \mu_2, \epsilon_2$, respectively. The normal, \mathbf{n} , is positive across the boundary from medium 1 to 2, and the tangent, \mathbf{t} is parallel to the boundary. The superscripts of \mathbf{n} and \mathbf{t} in next equation, stand for the normal and tangential components of the fields, respectively.

A small cylinder that encloses a part of the boundary, has a surface area of A_b and thickness d_b . As the thickness approaches 0, it is fair to assume that the EM fields are close to constant on each side of the box. For a current that flows across the boundaries, in a steady state

$$J_1^n A_b = J_2^n A_b = \sigma_1 E_1^n = \sigma_2 E_2^n \Rightarrow E_2^n = \frac{\sigma_1}{\sigma_2} E_1^n \quad (2.4)$$

The electric field in Equation 2.4 is discontinuous across the boundary, due to charge build up on the boundary. The surface charge density can be calculated by integrating Equation 2.1d over the volume of the box, giving

$$\int_{V_b} \nabla \cdot \mathbf{D} dV = \int_S \mathbf{D} \cdot \mathbf{n} dS = \int_S D^n dS = \int_{V_b} q dV = Q \quad (2.5)$$

where the divergence theorem is used to simplify the volume integral and the normal Q is the total charge with in the volume V_b . There is no flux out of the sides of the cylinder since $\mathbf{D} \cdot \mathbf{n}_{side} = (0, 0, D^n) \cdot (0, 1, 0) = (0, 0, D^n) \cdot (1, 0, 0) = 0$ as only the component across the boundary is considered. Solving the integrals in Equation 2.5,

yields that

$$(\mathbf{D}_1^n - \mathbf{D}_2^n)A_b = (\epsilon_1 E_1^n - \epsilon_2 E_2^n)A_b = Q \quad (2.6)$$

By placing Equation 2.4 in Equation 2.6 yields surface charge density, q_A as

$$q_A = \frac{Q}{A_b} = E_1^n \left(\epsilon_1 - \epsilon_2 \frac{\sigma_1}{\sigma_2} \right) \quad (2.7)$$

Considering a rectangular loop, L , over the boundary with length l_L , thickness d_L and a surface area of $S_L = l_L \cdot d_L$. Integrating Equation 2.1a over the surface S_l but using Stokes theorem to write it out as a line integral around the loop L , gives

$$\int_V \nabla \times \mathbf{E} dV = \oint_L \mathbf{E} \cdot \mathbf{t} dl = \int_{l_L} E^t \cdot \mathbf{t} dl + \int_{d_L} E^t \cdot \mathbf{t} dl = -\frac{\partial}{\partial t} \int_S \mathbf{B} dS \quad (2.8)$$

The side integrals are always 0, since the dot product of the normal component and the tangent of the sides is always 0. As the thickness, d_L , approaches 0, the surface area S_L tends to 0 forcing $\int_S \mathbf{B} dS \rightarrow 0$. Equation 2.8 then becomes

$$(E_1^t - E_2^t)l_L = 0 \Rightarrow E_1^t = E_2^t \quad (2.9)$$

showing that the tangential components of the E fields are continuous at the boundary. Similarly, integrating Equation 2.1b along the loop L gives

$$\oint_L \mathbf{B} dl = (B_1^t - B_2^t)l_L = \mu \int_S J dS \quad (2.10)$$

As before, when $d_L \rightarrow 0 \Rightarrow S_L \rightarrow 0$ and $\int_S \mathbf{J} dS \rightarrow 0$. Equation 2.10 then becomes

$$(B_1^t - B_2^t)l_L = 0 \Rightarrow B_1^t = B_2^t \quad (2.11)$$

showing that the tangential components of the B fields are also continuous at the boundary.

2.2 MT method

2.2.1 Overview

The Magnetotelluric (MT) method is a passive electromagnetic (EM) exploration method that measures orthogonal components of electric and magnetic fields at the surface of the Earth. Figure 2.1 shows a typical MT setup. The naturally generated variations in Earth's magnetic field are the source field, providing a wide and continuous spectrum of EM field waves that induce currents within the earth. These induction currents contribute to the measured fields on the surface and hold information about the subsurface conductivity structure ranging from few tens of meters to hundreds of kilometers depth.

The sources of the variations in Earth's magnetic field depend on the frequency of the EM fields. For frequencies greater than 1 Hz the most significant sources are lightning discharges at the equatorial region of the Earth. The EM signals generated by lightning events, known as Sferics, propagate in a waveguide constrained by Earth's surface and its ionosphere allowing them to reach regions far away. Interaction of Earth's magnetosphere and solar winds generate EM waves with frequencies lower than 1 Hz. When encountering Earth's magnetopause, protons and electrons in the plasma of the solar wind, are deflected in opposite directions, generating an electric field. Variations in the density, velocity and intensity of the solar wind produce time varying EM fields.

The theoretical basis of the MT method was established in Tikhonov (1950) and Cagniard (1953). The essential foundations of these publications are (1) the use of the ratio of the measured fields to cancel out the unknown source field and (2) that the frequency governs the penetration of the EM waves and therefore the depth of investigation. EM responses from great depths can be obtained by measuring EM responses over a long time period. This will provide low frequency signals that may be related to resistivity at great depth. This principle is embodied in the skindepth relation

$$\delta_{MT}(f) = \sqrt{\frac{1}{f\sigma\mu\pi}} \quad (2.12)$$

and is derived in Equation 2.46. Here $\delta_{MT}(f)$ is the EM skindepth in meters for a wave of frequency f and σ and μ are the conductivity and the magnetic permeability, respectively, of the medium being penetrated. Equation 2.12 gives the depth, $\delta_{MT}(f)$, at which the EM fields have attenuated to e^{-1} of their value at the Earth's surface. In the MT method, the frequency dependent skindepth is generally con-

sidered to be the penetration depth of the EM fields into the Earth at that given frequency.

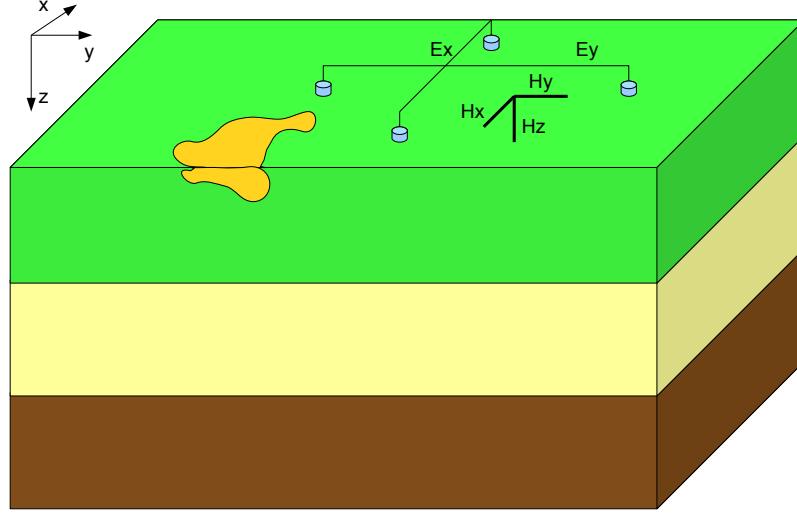


Figure 2.1: MT setup in an internal coordinate system. The setup measures electrical field in orthogonal horizontal direction and magnetic field in orthogonal vertical and horizontal direction.

Faraday's law, Equation 2.1a, describes the induction of a electric current in the Earth by a time varying magnetic field. The induced current generates an electric field as stated by Ohm's law, where the strength of the electric field depends upon the current and the conductivity of the medium that the current flows in. By measuring the magnetic and electric fields simultaneously at the same location and by using the ratio of the fields at varying frequencies, conductivity can be obtained for a wide depth range at that location. The inherent depth information in the data, ability of measuring from the surface down to tens to hundreds of kilometers and easy field application make the MT method practical and popular.

2.2.2 Electromagnetic waves in conductive medium

In a homogeneous and isotropic halfspace, using the constitutive relationships in Equation 2.2 and assuming time dependence of $e^{-i\omega t}$, Equations 2.1a and 2.1b may be rewritten as

$$\nabla \times \mathbf{E} = i\omega\mu\mathbf{H} \quad (2.13a)$$

$$\nabla \times \mathbf{H} = \sigma\mathbf{E} - i\omega\epsilon\mathbf{E} \quad (2.13b)$$

The only conductive boundary is the horizontal surface, so only a vertical component of the electric field, E_z would lead to charge build up on the surface. In the MT sounding method, the EM source waves are considered to be plane waves. A EM wave of angular frequency ω and with an angle of incidence θ_i travels through the air and approaches the surface of homogeneous earth of conductivity σ . When the wave hits the surface it is both reflected back and refracted into the halfspace at an angle of refraction θ_t . The relation between angles of the incidence and the refracted waves is given by Snell's law as

$$\frac{1}{v_0} \sin(\theta_i) = \frac{1}{v} \sin(\theta_t) \quad (2.14)$$

where

$$v_0 = \frac{1}{\sqrt{\epsilon_0\mu_0}} = c \quad \text{and} \quad v = \frac{\omega}{|k|} = \sqrt{\frac{2\omega}{\mu_0\sigma}}$$

v_0 is the velocity of an EM wave in the free air, the speed of light c . v is the velocity of an EM wave in the homogeneous halfspace, ω is the angular frequency and k is the wave prorogation constant of the EM wave. Inserting the values, Equation 2.14 becomes

$$\sin(\theta_t) = \sqrt{\frac{2\omega\epsilon_0}{\sigma}} \sin(\theta_i) \quad (2.15)$$

The frequency range for the MT method is $10^4 - 10^{-4}$ Hz and the conductivity of the subsurface rocks ranges from $10^3 - 10^{-4}$ S/m ($10^{-3} - 10^4 \Omega m$). In the following discussion it is assumed that the magnetic permeability is equal to that of vacuum. The relative dielectric permittivity values of rocks are in range of 1-100, were $\epsilon = \epsilon_r\epsilon_0$. Using the upper limits of this range gives

$$\sqrt{\frac{2\omega\epsilon_r\epsilon_0}{\sigma}} < 10^{-6}$$

As $\sin(\theta_i) \leq 1$, the angle of the refracted wave in the homogeneous halfspace is close to zero, indicating that the wave travels close to the vertical for all angles of

incidence. It can be assumed that the EM wave travels as a plane wave with a direction of travel vertically into the earth. In a halfspace, the E_z component is always 0, leading to no surface charge build up. The electrical charge density, q , is always zero within the halfspace and Equation 2.1d becomes

$$\nabla \cdot \mathbf{E} = 0 \quad (2.16)$$

Taking the curl of Equations 2.13 gives

$$\nabla \times \nabla \times \mathbf{E} = i\omega\mu \nabla \times \mathbf{H} = i\omega\mu(\sigma - i\omega\epsilon)\mathbf{E} \quad (2.17a)$$

$$\nabla \times \nabla \times \mathbf{H} = (\sigma - i\omega\epsilon)\nabla \times \mathbf{E} = (\sigma - i\omega\epsilon)i\omega\mu\mathbf{H} \quad (2.17b)$$

Using the vector identity

$$\nabla \times \nabla \times \mathbf{A} = -\nabla^2 \mathbf{A} + \nabla(\nabla \cdot \mathbf{A}) \quad (2.18)$$

and the condition from Equation 2.16, Equation 2.17a becomes

$$\nabla^2 \mathbf{E} + i\omega\mu(\sigma - i\omega\epsilon)\mathbf{E} = 0 \quad (2.19)$$

Similarly, by using the condition from Equation 2.1c, Equation 2.17b becomes

$$\nabla^2 \mathbf{H} + i\omega\mu(\sigma - i\omega\epsilon)\mathbf{H} = 0 \quad (2.20)$$

Both Equation 2.19 and 2.20 are second order differential Equations with dependence on ω and wave propagation constant of $k^2 = \omega\mu(i\sigma + \omega\epsilon)$. Using the same extreme values for the conductivity σ and the angular frequency ω as before, it holds that

$$(\omega\epsilon)_{max} = 2\pi f\epsilon_r\epsilon_0 \approx 5 \cdot 10^{-5}$$

It holds that $\sigma \gg \omega\epsilon$ and therefore neglecting the non-diffusive part of the EM wave is justified. This simplification is referred to as the quasi-static approximation

and reduces the wave propagation constant to $k^2 = i\omega\mu\sigma$. With this approximation, Equations 2.19 and 2.20 are reduced to

$$\nabla^2 \mathbf{E} + i\omega\mu\sigma \mathbf{E} = 0 \quad (2.21)$$

$$\nabla^2 \mathbf{H} + i\omega\mu\sigma \mathbf{H} = 0 \quad (2.22)$$

2.2.3 MT solution in horizontally layered earth

As for a homogeneous halfspace, an EM plane wave in a horizontally layered earth travels vertically, from layer to the next. When passing through the layers, current flows are excited within the layers, producing EM fields. The fields depend on the conductivity of the layer allowing for information about the conductivity to be derived.

Consider a layered earth of N layers, where each layer has a uniform conductivity σ_l , magnetic permeability as that of free air (μ_0), and thickness of d_l . The N^{th} layer is considered to have infinite thickness, therefore being a halfspace. The propagation of the EM wave in the earth is described with the Helmholtz Equations 2.21 and 2.22. In a Cartesian coordinate system where the x, y and z axes are positive towards the North, East and Down, respectively, and writing out the ∇^2 operator, they become

$$\frac{\partial^2 \mathbf{E}}{\partial x^2} + \frac{\partial^2 \mathbf{E}}{\partial y^2} + \frac{\partial^2 \mathbf{E}}{\partial z^2} + i\omega\mu_0\sigma_l \mathbf{E} = 0 \quad (2.23a)$$

$$\frac{\partial^2 \mathbf{E}}{\partial x^2} + \frac{\partial^2 \mathbf{H}}{\partial y^2} + \frac{\partial^2 \mathbf{H}}{\partial z^2} + i\omega\mu_0\sigma_l \mathbf{H} = 0 \quad (2.23b)$$

There are no conductivity variations in the x and y directions and the wave propagates downwards, so Equations 2.23a and 2.23b simplify to

$$\frac{\partial^2 \mathbf{E}}{\partial z^2} + i\omega\mu_0\sigma_l \mathbf{E} = 0 \quad (2.24a)$$

$$\frac{\partial^2 \mathbf{H}}{\partial z^2} + i\omega\mu_0\sigma_l \mathbf{H} = 0 \quad (2.24b)$$

where the propagation constant for l^{th} layer is $k_l^2 = i\omega\mu_0\sigma_l$. The depth to the top of the l^{th} layer is z_l and $z_0 = 0$ is the surface of the earth. Within the l^{th} layer, Equations 2.24a has a harmonic solutions of

$$E_x(z) = A_x e^{-ik_l z} + B_x e^{ik_l z} \quad (2.25)$$

$$E_y(z) = A_y e^{-ik_l z} + B_y e^{ik_l z} \quad (2.26)$$

where the first terms in Equations 2.25 and 2.26 describe electric fields that increase in amplitude with depth (travel upwards) but the second term describes fields that decrease with depth (travel downwards). The constants A and B are arbitrary and are determined using boundary conditions. Writing out the $\nabla \times$ operator in Equation 2.13a in scalar form and utilizing that the derivatives with respect to x and y are 0, gives

$$H_x(z) = -\frac{1}{i\omega\mu} \frac{\partial E_y(z)}{\partial z}, \quad H_y(z) = \frac{1}{i\omega\mu} \frac{\partial E_x(z)}{\partial z}, \quad H_z = 0 \quad (2.27)$$

Substituting the solutions in Equations 2.25 and 2.26 into Equation 2.27 yields

$$H_x(z) = \frac{k_l}{\omega\mu_0} (A_y e^{-ik_l z} - B_y e^{ik_l z}) \quad (2.28)$$

$$H_y(z) = -\frac{k_l}{\omega\mu_0} (A_x e^{-ik_l z} - B_x e^{ik_l z}) \quad (2.29)$$

Taking the ratio of the electric and magnetic fields, yields the Tikhonov-Cagniard wave impedance as

$$Z_{xy} = \frac{E_x}{H_y} \quad Z_{yx} = \frac{E_y}{H_x} \quad (2.30)$$

Substituting Equations 2.25, 2.26, 2.28 and 2.29 into Equations 2.30 yields

$$Z_{xy} = \frac{\omega\mu_0}{k_l} \frac{A_x e^{-ik_l z} + B_x e^{ik_l z}}{A_y e^{-ik_l z} - B_y e^{ik_l z}} \quad (2.31)$$

$$Z_{yx} = -\frac{\omega\mu_0}{k_l} \frac{A_y e^{-ik_l z} + B_y e^{ik_l z}}{A_x e^{-ik_l z} - B_x e^{ik_l z}} \quad (2.32)$$

In all layers, the arbitrary constants A_x , A_y , B_x and B_y depend on properties of the layer that are constant in the horizontal directions. Therefore $A_x = A_y = A_l$ and

2 Theory of Electromagnetic methods

$B_x = B_y = B_l$, yielding that $\hat{Z}_l = Z_{xy} = -Z_{yx}$ from in Equations 2.31 and 2.32. At boundaries between layers it is required that the impedance is constant. At the top of the l^{th} layer the impedance is

$$\hat{Z}_{l-1} = Q \frac{A_l e^{-ik_l z_{l-1}} + B_l e^{ik_l z_{l-1}}}{A_l e^{-ik_l z_{l-1}} - B_l e^{ik_l z_{l-1}}} \quad (2.33)$$

where $Q = \frac{\omega \mu_0}{k_l}$ is the characteristic impedance of the l^{th} layer, A_l and B_l are arbitrary constants for l^{th} layer, and z_{l-1} is the depth to the top of the layer. Similarly, at the bottom of the l^{th} layer the impedance is

$$\hat{Z}_l = Q \frac{A_l e^{-ik_l z_l} + B_l e^{ik_l z_l}}{A_l e^{-ik_l z_l} - B_l e^{ik_l z_l}} \quad (2.34)$$

where z_l is the depth to the bottom of the l^{th} layer. Dividing the denominator and the numerator of Equation 2.34 by $(A_l B_l)^{\frac{1}{2}}$ and rearranging yields

$$\hat{Z}_l = Q \frac{\left(\frac{A_l}{B_l}\right)^{\frac{1}{2}} e^{-ik_l z_l} + \left(\frac{B_l}{A_l}\right)^{\frac{1}{2}} e^{ik_l z_l}}{\left(\frac{A_l}{B_l}\right)^{\frac{1}{2}} e^{-ik_l z_l} - \left(\frac{B_l}{A_l}\right)^{\frac{1}{2}} e^{ik_l z_l}} \Rightarrow \left(\frac{A_l}{B_l}\right)^{\frac{1}{2}} = \frac{\left(\frac{B_l}{A_l}\right)^{\frac{1}{2}} (\hat{Z}_l e^{ik_l z_l} + Q e^{ik_l z_l})}{(\hat{Z}_l e^{-ik_l z_l} - Q e^{-ik_l z_l})} \quad (2.35)$$

By using the same methodology, Equation 2.33 becomes

$$\hat{Z}_{l-1} = Q \frac{\left(\frac{A_l}{B_l}\right)^{\frac{1}{2}} e^{-ik_l z_{l-1}} + \left(\frac{B_l}{A_l}\right)^{\frac{1}{2}} e^{ik_l z_{l-1}}}{\left(\frac{A_l}{B_l}\right)^{\frac{1}{2}} e^{-ik_l z_{l-1}} - \left(\frac{B_l}{A_l}\right)^{\frac{1}{2}} e^{ik_l z_{l-1}}} \quad (2.36)$$

By substituting Equation 2.35 into Equation 2.36 will yield an Equation without any constants A_l and B_l as

$$\hat{Z}_{l-1} = Q \frac{\hat{Z}_l + Q \tanh(ik_l d_l)}{Q + \hat{Z}_l \tanh(ik_l d_l)} \quad (2.37)$$

where $d_l = z_l - z_{l-1}$ is the thickness of the l^{th} layer. Equation 2.37 is known as the recursion formula and allows for calculating impedance at top of the l^{th} layer knowing the impedance at the $l+1^{th}$ layer.

At the top of the N^{th} layer the impedance is that of a halfspace. There is no upward traveling wave in this bottom halfspace, so the fields within it are

$$E_x(z) = A_x e^{ik_l z} \quad (2.38)$$

$$H_y(z) = \frac{k_l}{\omega \mu_0} (A_x e^{ik_l z}) \quad (2.39)$$

and calculating the impedance for the bottom halfspace layer yields

$$Z_N(z) = \frac{E_x(z)}{H_y(z)} = -\frac{E_y(z)}{H_x(z)} = \frac{\omega \mu_0}{k_N} \quad (2.40)$$

where $z_{N-1} \leq z \leq \infty$. This provides the impedance at the boundary between the N^{th} and $N-1^{th}$ layers. By iteratively solving the recursion Equation 2.37, the impedance at each layer boundary can be found from the bottom up. Solving the Equation $N-1$ times, will give the impedance at the surface of the earth.

2.2.4 Impedance tensor

The orthogonal electrical and magnetic fields collected in the MT soundings can be related through a complex impedance tensor \mathbf{Z} . In matrix form this relation is

$$\begin{aligned} \mathbf{E}(\omega) &= \mathbf{Z}(\omega) \mathbf{H}(\omega) \\ \begin{bmatrix} E_x(\omega) \\ E_y(\omega) \end{bmatrix} &= \begin{bmatrix} Z_{xx}(\omega) & Z_{xy}(\omega) \\ Z_{yx}(\omega) & Z_{yy}(\omega) \end{bmatrix} \begin{bmatrix} H_x(\omega) \\ H_y(\omega) \end{bmatrix} \end{aligned} \quad (2.41)$$

The impedance depends on frequency, relating the measured fields at individual frequencies. The linear relations of the fields can be written as

$$E_x(\omega) = Z_{xx}(\omega) H_x(\omega) + Z_{xy}(\omega) H_y(\omega) \quad (2.42a)$$

$$E_y(\omega) = Z_{yx}(\omega) H_x(\omega) + Z_{yy}(\omega) H_y(\omega) \quad (2.42b)$$

where the on-diagonal elements relate fields measured in the same direction whereas the off-diagonal elements relate the orthogonally measured fields.

Homogeneous earth

For a homogeneous earth, the conductivity σ (or resistivity $\rho = 1/\sigma$) is isotropic and the impedance is calculated with Equation 2.40. Rewriting the wave propagation constant as $k = \sqrt{i}\sqrt{\omega\mu_0\sigma} = \frac{1+i}{\sqrt{2}}\sqrt{\omega\mu_0\sigma}$ and substituting in Equation 2.40 yields

$$Z = \frac{\omega\mu_0}{\sqrt{\omega\mu_0\sigma}} \frac{\sqrt{2}}{1+i} = \sqrt{\frac{\omega\mu_0}{\sigma}} \frac{\sqrt{2}}{2}(1-i) = \sqrt{\frac{\omega\mu_0}{\sigma}} e^{-i\pi/4} \quad (2.43)$$

The phase angle between the E and H fields is $\pi/4$ or 45° , where the E field lags the H field. By taking the absolute value and squaring the impedance yields

$$\begin{aligned} \left| \frac{E(\omega)}{H_\perp(\omega)} \right|^2 &= \left| \frac{\omega\mu_0}{k} \right|^2 = \frac{\omega\mu_0}{\sigma} \\ \Rightarrow \rho &= \frac{1}{\sigma} = \frac{1}{\omega\mu_0} \left| \frac{E(\omega)}{H_\perp(\omega)} \right|^2 = \frac{1}{\omega\mu_0} |Z|^2 \end{aligned} \quad (2.44)$$

where \perp is an orthogonal field. The resistivity derived in Equation 2.44 is the true resistivity of the halfspace. The skindepth of an EM wave, is the depth where the amplitude of the field has decreased to e^{-1} of its amplitude at the surface. It is the reciprocal of the real part of the wave propagation constant and is calculated as

$$\delta(\omega) = \frac{1}{\Re(k)} = \sqrt{\frac{2\rho}{\omega\mu_0}} \quad (2.45)$$

When using standard units, Equation 2.45 can be reduced to

$$\delta(f) \approx 500 \sqrt{\frac{\rho}{f}} \quad (2.46)$$

with units of the skindepth in meters and where f is the frequency.

1D impedance tensor

For a 1D layered earth, the conductivity σ (or resistivity $\rho = 1/\sigma$) changes only with depth. In this case, the impedance tensor may be written as

$$\mathbf{Z}_{1D} = \begin{bmatrix} 0 & Z_n \\ -Z_n & 0 \end{bmatrix} \quad (2.47)$$

For a layered earth the apparent resistivity, ρ^{app} , is defined as

$$\rho^{app}(\omega) = \frac{1}{\omega\mu_0} |Z_n(\omega)| \quad (2.48)$$

The phase angle of the impedance is defined as

$$\Phi(\omega) = \arctan \left(\frac{\Im(Z_n(\omega))}{\Re(Z_n(\omega))} \right) \quad (2.49)$$

Both the apparent resistivity in Equation 2.48 and the phase in Equation 2.49 depend on the angular frequency, $\omega = 2\pi f$, where f is the frequency.

2D impedance tensor

For a 2D earth, the conductivity, σ (or resistivity $\rho = 1/\sigma$) changes with depth and in one horizontal direction. The other horizontal direction has no variations in conductivity and is commonly known as the electromagnetic or geoelectrical strike direction.

In Berdichevsky and Dmitriev (2008), it is shown by decomposing the E and H into normal and anomalous field components, that in a general 2D earth, the impedance tensor becomes

$$\mathbf{Z}_{2D} = \begin{bmatrix} Z_d & Z_{xy} \\ Z_{yx} & -Z_d \end{bmatrix} \quad (2.50)$$

Here, neither of the horizontal axes are aligned along the electromagnetic strike. In the impedance tensor, the diagonal elements $Z_{xx} = -Z_{yy} = Z_d$ are equal in amplitude but opposite in signs. The off-diagonal elements Z_{xy} and Z_{yx} are independent

values. However, if the impedance tensor is rotated such that the x direction is parallel and the y direction is perpendicular to the electromagnetic strike direction, the Z_{2D} impedance tensor simplifies to

$$\mathbf{Z}_{2D} = \begin{bmatrix} 0 & Z_{xy} \\ Z_{yx} & 0 \end{bmatrix} \quad (2.51)$$

The modes of the impedance tensor, can be analyzed independently. Transverse Electric (TE) mode or E-polarization is when the electric field is parallel to the electromagnetic strike and Transverse Magnetic (TM) mode or B-polarization is when the magnetic field is parallel to the electromagnetic strike. In Equation 2.51, the TE mode is $Z_{TE} = Z_{xy}$ and the TM mode is $Z_{TM} = Z_{yx}$.

Apparent resistivity can be calculated for each of the modes such that

$$\rho_{TE}^{app}(\omega) = \frac{1}{\omega\mu_0} |Z_{TE}(\omega)| \quad \text{and} \quad \rho_{TM}^{app}(\omega) = \frac{1}{\omega\mu_0} |Z_{TM}(\omega)| \quad (2.52)$$

and similarly the phase angle

$$\Phi_{TE}(\omega) = \arctan\left(\frac{\Im(Z_{TE}(\omega))}{\Re(Z_{TE}(\omega))}\right) \quad \text{and} \quad \Phi_{TM}(\omega) = \arctan\left(\frac{\Im(Z_{TM}(\omega))}{\Re(Z_{TM}(\omega))}\right) \quad (2.53)$$

3D impedance tensor

In a 3D earth model, the conductivity, σ (or resistivity $\rho = 1/\sigma$) varies in all directions, $\sigma(x, y, z)$. The impedance tensor takes the general form

$$\mathbf{Z}_{3D} = \begin{bmatrix} Z_{xx} & Z_{xy} \\ Z_{yx} & Z_{yy} \end{bmatrix} \quad (2.54)$$

All the elements in the impedance tensor in Equation 2.54 are non-zero elements. There is no direction where the diagonal elements of the impedance tensor vanish, so all the elements in the tensor need to be considered.

2.2.5 Rotation and combinations of impedance tensor

The impedance tensor as in Equation 2.41 depends on the coordinate frame of the measurement. The measurement axes have to be orthogonal, but their direction is otherwise arbitrary. A mathematical rotation can be applied to rotate the direction of the measurement axes, such that

$$\mathbf{Z}'(\omega) = \mathbf{R}(\phi)\mathbf{Z}(\omega)\mathbf{R}(\phi)^T \quad (2.55)$$

where \mathbf{Z}' is the rotated impedance, ϕ is the angle of rotation that is defined positive clockwise, and $\mathbf{R}(\phi)$ and $\mathbf{R}(\phi)^T$ are the rotation matrix and its transpose, respectively. They are defined as

$$\mathbf{R}(\phi) = \begin{bmatrix} \cos(\phi) & \sin(\phi) \\ -\sin(\phi) & \cos(\phi) \end{bmatrix} \quad \text{and} \quad \mathbf{R}(\phi)^T = \begin{bmatrix} \cos(\phi) & -\sin(\phi) \\ \sin(\phi) & \cos(\phi) \end{bmatrix} \quad (2.56)$$

In the new coordinate system, the elements of the impedance tensor \mathbf{Z}' can be written in terms of elements of the original impedance tensor as

$$Z'_{xx} = \cos^2(\phi)Z_{xx} + \cos(\phi)\sin(\phi)(Z_{xy} + Z_{yx}) + \sin^2(\phi)Z_{yy} \quad (2.57a)$$

$$Z'_{xy} = \cos^2(\phi)Z_{xy} + \cos(\phi)\sin(\phi)(Z_{yy} - Z_{xx}) - \sin^2(\phi)Z_{yx} \quad (2.57b)$$

$$Z'_{yx} = \cos^2(\phi)Z_{yx} + \cos(\phi)\sin(\phi)(Z_{yy} - Z_{xx}) - \sin^2(\phi)Z_{xy} \quad (2.57c)$$

$$Z'_{yy} = \cos^2(\phi)Z_{yy} - \cos(\phi)\sin(\phi)(Z_{xy} + Z_{yx}) + \sin^2(\phi)Z_{xx} \quad (2.57d)$$

The impedance tensor of a 1D earth (as in Equation 2.47) can be rotated by an arbitrary angle Φ by using Equations 2.57:

$$\begin{aligned} Z'_{xx} &= 0 \\ Z'_{xy} &= Z_n \sin^2(\Phi) + Z_n \cos^2(\Phi) = Z_n = Z_{xy} \\ Z'_{yx} &= -Z_n \sin^2(\Phi) - Z_n \cos^2(\Phi) = -Z_n = Z_{xy} \\ Z'_{yy} &= 0 \end{aligned} \quad (2.58)$$

The impedance tensor for 1D earth is rotationally invariant. In 1D interpretation of MT soundings, combinations of the impedance tensor elements are often used

(Ranganayaki, 1984). Park and Livelybrooks (1989) lists 3 rotationally invariant combinations

$$Z_{ave} = \frac{Z_{xy} - Z_{yx}}{2} \quad (2.59)$$

$$Z_{gma} = \sqrt{-Z_{xy}Z_{yx}} \quad (2.60)$$

$$Z_{det} = \sqrt{Z_{xx}Z_{yy} - Z_{xy}Z_{yx}} \quad (2.61)$$

where Equations 2.59, 2.60 and 2.61 are the arithmetic average, the geometric average of the off-diagonal elements and the determinant of the impedance tensor, respectively. The invariance of the of determinant can be shown as

$$\begin{aligned} (Z'_{det}(\Phi))^2 &= Z'_{xx}(\Phi)Z'_{yy}(\Phi) - Z'_{xy}(\Phi)Z'_{yx}(\Phi) \\ &= (\cos^2(\Phi)Z_{xx} + \cos(\Phi)\sin(\Phi)Z_{xy} + \cos(\Phi)\sin(\Phi)Z_{yx} + \sin^2(\Phi)Z_{yy}) \\ &\quad (\cos^2(\Phi)Z_{yy} - \cos(\Phi)\sin(\Phi)Z_{xy} - \cos(\Phi)\sin(\Phi)Z_{yx} + \sin^2(\Phi)Z_{xx}) \\ &\quad - (\cos^2(\Phi)Z_{xy} + \cos(\Phi)\sin(\Phi)Z_{yy} - \cos(\Phi)\sin(\Phi)Z_{xx} - \sin^2(\Phi)Z_{yx}) \\ &\quad (\cos^2(\Phi)Z_{yx} + \cos(\Phi)\sin(\Phi)Z_{yy} - \cos(\Phi)\sin(\Phi)Z_{xx} - \sin^2(\Phi)Z_{xy}) \\ &= (\sin^4(\Phi) + 2\sin^2(\Phi)\cos^2(\Phi) + \cos^4(\Phi))Z_{yy}Z_{xx} \\ &\quad - (\sin^4(\Phi) + 2\sin^2(\Phi)\cos^2(\Phi) + \cos^4(\Phi))Z_{xy}Z_{yx} \\ &= Z_{yy}Z_{xx} - Z_{xy}Z_{yx} \end{aligned} \quad (2.62)$$

In Equation 2.62, under a rotation by an arbitrary angle, Φ , the rotated determinant Z'_{det} is always equal to the Z_{det} showing that the determinant of the impedance tensor is rotationally invariant.

2.2.6 Dimensionality measures

For a 3D impedance tensor (as in Equation 2.41), no true electromagnetic strike can be found, since the on-diagonal elements in the impedance tensor are never equal to zero under any rotation angle. An angle of rotation Φ_0 that either minimizes the on-diagonal elements or maximizes the off-diagonal elements in impedance tensor is often used to approximate the strike direction. Rotation by the angle Φ_0 , is the direction where the impedance is closest to being that of a 2D earth model, where the diagonal elements are zero as in Equation 2.51 (Simpson and Bahr, 2005). The angle Φ_0 , is found by incrementally rotating the impedance tensor and then finding the minimum or maximum of combinations of the tensor elements, such as

$$\min(|Z'_{xx} + Z'_{yy}|) \quad \text{or} \quad \max(|Z'_{xy} + Z'_{yx}|) \quad (2.63)$$

$$\min(|Z'_{xx}|^2 + |Z'_{yy}|^2) \quad \text{or} \quad \max(|Z'_{xy}|^2 + |Z'_{yx}|^2) \quad (2.64)$$

For a true 2D earth, the method of finding the electromagnetic strike direction in Equations 2.63 and 2.64 should yield the same direction but in practice that is not always the case. For a 2D earth there are ambiguities in the calculated electromagnetic strike direction, since rotation by 90° exchanges the orientation of the principle impedance directions, x and y.

The ratio of the sum of the on-diagonal and the off-diagonal elements in the impedance tensor, is called the skew, and is calculated as

$$skew = \left| \frac{Z_{xx} + Z_{yy}}{Z_{xy} - Z_{yx}} \right| \quad (2.65)$$

The skew parameter is rotationally invariant and used as an indicator of the dimensionality of the impedance tensor. For 1D and pure 2D earth, the skew should be close to zero. Increased values indicate the presence of 3D structure.

2.2.7 Real data processing

In order to calculate impedances from the measured time series of the orthogonal EM fields at the surface, a few steps need to be taken. During the data collection the time series are amplified, filtered and converted from analog to digital format within the data collecting system. During the data processing, the series are split into segments and Fourier transformed from time to the frequency domain. Fast Fourier Transforms (FFT) are commonly used to transform the measured time series to the frequency domain (Vozoff, 1991).

Impedance estimations

When the raw time series have been transformed from the time domain to the frequency domain, Equation 2.42a relates the impedances to the measured EM fields at the surface.

$$\begin{aligned} E_x(\omega) &= Z_{xx}(\omega)H_x(\omega) + Z_{xy}(\omega)H_y(\omega) \\ E_y(\omega) &= Z_{yx}(\omega)H_x(\omega) + Z_{yy}(\omega)H_y(\omega) \end{aligned}$$

In order to calculate the impedances, cross powers of the frequency dependent electric and magnetic fields are needed. Cross power of any two frequency dependent channels $C(f_j)$ and $D(f_j)$ over the frequency band f_{j-m} to f_{j+m} is given as

$$\langle C(f_j) \bullet D(f_j) \rangle = \langle C_j, D_j \rangle = \frac{1}{2m+1} \sum_{k=j-m}^{j+m} C_k D_k^* \quad (2.66)$$

where $\langle \rangle$ is the complex cross-power, D^* denotes the complex conjugate and j signifies the f_j frequency dependence. Assuming that the impedances have small variations over the narrow frequency window (f_{j-m}, f_{j+m}) and doing a cross-power multiplication of the complex conjugates of a field B , yields

$$\langle E_x, B^* \rangle = Z_{xx} \langle H_x, B^* \rangle + Z_{xy} \langle H_y, B^* \rangle \quad (2.67a)$$

$$\langle E_y, B^* \rangle = Z_{yx} \langle H_x, B^* \rangle + Z_{yy} \langle H_y, B^* \rangle \quad (2.67b)$$

where B^* is a complex conjugate of an orthogonal pair of either the electric (E_x, E_y) or magnetic (H_x, H_y) fields. Using the magnetic fields gives

$$\langle E_x, H_x^* \rangle = Z_{xx} \langle H_x, H_x^* \rangle + Z_{xy} \langle H_y, H_x^* \rangle \quad (2.68a)$$

$$\langle E_x, H_y^* \rangle = Z_{xx} \langle H_x, H_y^* \rangle + Z_{xy} \langle H_y, H_y^* \rangle \quad (2.68b)$$

$$\langle E_y, H_x^* \rangle = Z_{yx} \langle H_y, H_x^* \rangle + Z_{yy} \langle H_y, H_x^* \rangle \quad (2.68c)$$

$$\langle E_y, H_y^* \rangle = Z_{yx} \langle H_y, H_y^* \rangle + Z_{yy} \langle H_y, H_y^* \rangle \quad (2.68d)$$

Solving for the impedances in Equations 2.68, yields the impedances as functions of cross- and auto-powers of the EM fields dependent on frequency at the surface of the earth as

$$Z_{xx} = \frac{\langle E_x, H_x^* \rangle \langle H_y, H_y^* \rangle - \langle E_x, H_y^* \rangle \langle H_y, H_x^* \rangle}{\langle H_x, H_x^* \rangle \langle H_y, H_y^* \rangle - \langle H_x, H_y^* \rangle \langle H_y, H_x^* \rangle} \quad (2.69a)$$

$$Z_{xy} = \frac{\langle E_x, H_x^* \rangle \langle H_x, H_y^* \rangle - \langle E_x, H_y^* \rangle \langle H_x, H_x^* \rangle}{\langle H_y, H_x^* \rangle \langle H_x, H_y^* \rangle - \langle H_y, H_y^* \rangle \langle H_x, H_x^* \rangle} \quad (2.69b)$$

$$Z_{yx} = \frac{\langle E_y, H_x^* \rangle \langle H_y, H_y^* \rangle - \langle E_y, H_y^* \rangle \langle H_y, H_x^* \rangle}{\langle H_x, H_x^* \rangle \langle H_y, H_y^* \rangle - \langle H_x, H_y^* \rangle \langle H_y, H_x^* \rangle} \quad (2.69c)$$

$$Z_{yy} = \frac{\langle E_y, H_x^* \rangle \langle H_x, H_y^* \rangle - \langle E_y, H_y^* \rangle \langle H_x, H_x^* \rangle}{\langle H_y, H_x^* \rangle \langle H_x, H_y^* \rangle - \langle H_y, H_y^* \rangle \langle H_x, H_x^* \rangle} \quad (2.69d)$$

Remote referencing impedance estimation

All of the Equations 2.69 contain auto-powers of the magnetic field, causing the estimates to be biased due to coherent noise. Gamble et al. (1979b,a) introduced a method to deal with the bias in the estimates of the impedances. The remote referencing method uses an additional MT sounding at a remote location, which is a sufficient distance away from the local measurement. The induced fields can be considered to be a combination of the uncontaminated signal of interest and site specific random noise. The signal of interest is considered to be correlated over long distances whereas the noise, if truly random, is uncorrelated between sites and the biasing in the estimates of the impedances should be removed. The distance between the local and remote soundings needs to be large enough such that the sources of noise are incoherent. Distance of 10 – 100km has been found to be enough for the assumption of the noise being uncorrelated to hold (Simpson and Bahr, 2005).

By using the B^* fields in Equation 2.68 as the magnetic fields from a remote reference sounding and going through the same derivation as above, yields equations for the impedances calculated with cross- and auto-powers of local and remote soundings

as

$$Z_{xx} = \frac{\langle E_x R_x^* \rangle \langle H_y R_y^* \rangle - \langle E_x R_y^* \rangle \langle H_y R_x^* \rangle}{\langle H_x R_x^* \rangle \langle H_y R_y^* \rangle - \langle H_x R_y^* \rangle \langle H_y R_x^* \rangle} \quad (2.70a)$$

$$Z_{xy} = \frac{\langle E_x R_x^* \rangle \langle H_x R_y^* \rangle - \langle E_x R_y^* \rangle \langle H_x R_x^* \rangle}{\langle H_y R_x^* \rangle \langle H_x R_y^* \rangle - \langle H_y R_y^* \rangle \langle H_x R_x^* \rangle} \quad (2.70b)$$

$$Z_{yx} = \frac{\langle E_y R_x^* \rangle \langle H_y R_y^* \rangle - \langle E_y R_y^* \rangle \langle H_y R_x^* \rangle}{\langle H_x R_x^* \rangle \langle H_y R_y^* \rangle - \langle H_x R_y^* \rangle \langle H_y R_x^* \rangle} \quad (2.70c)$$

$$Z_{yy} = \frac{\langle E_y R_x^* \rangle \langle H_x R_y^* \rangle - \langle E_y R_y^* \rangle \langle H_x R_x^* \rangle}{\langle H_y R_x^* \rangle \langle H_x R_y^* \rangle - \langle H_y R_y^* \rangle \langle H_x R_x^* \rangle} \quad (2.70d)$$

where R_x and R_y denote the H_x and H_y of the remote reference sounding, respectively. The remote referencing fields in Equation 2.70a can also be taken as the electrical fields, E_x and E_y , but using magnetic fields is the common practice as proposed by (Gamble et al., 1979b).

2.3 TEM method

2.3.1 Overview

The Transient ElectroMagnetic (TEM) sounding method is an active EM exploration method that measures EM response from eddy currents within the earth induced by a current in a loop or grounded wires on the surface. Figure 2.2 shows a central loop TEM sounding configuration. The source current is abruptly interrupted and time varying secondary fields from the induced eddy currents can be measured with an induction coil or magnetometer at the surface. The further in time after the turn-off, the deeper the eddy current propagates into the earth, allowing conductivities at different depths to be resolved.

An overview of the history of the TEM sounding method is given in (Spies and Frischknecht, 1991). The development of the TEM sounding methods started in the early 1950's. Lack of adequate instrumentation and interpretation methods hindered the widespread use of the method. It was not until the 1970's that development of instruments and methods of interpretation for the TEM soundings reached levels to gain the method wider use.

The depth to which the eddy currents can reach in earth depends on the time

from the current turn-off and the conductivity of the earth. Nabighian and Macnae (1991); Sternberg et al. (1988) show that the diffusion depth (time domain equivalent of skindepth) of the central loop TEM method is given as

$$\delta_{TEM}(t) = 1.28\sqrt{\frac{t}{\sigma\mu}} \quad (2.71)$$

where $\delta_{TEM}(t)$ is the depth in m where the ratio of the magnitude of the transient magnetic field and primary magnetic field during the current on-time is equal to e^{-1} . t is the time from the current turn-off, σ and μ are the conductivity and the magnetic permeability, respectively, of the earth. This time dependent depth approximates the depth to which the eddy currents have reached at a given time.

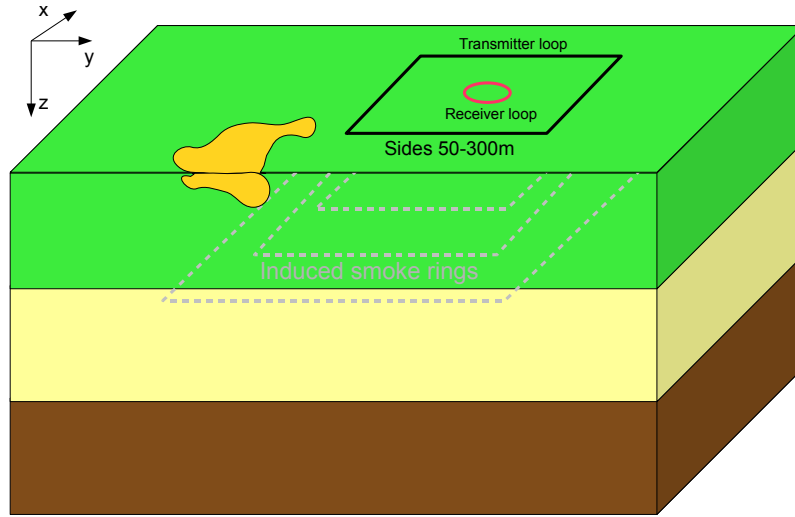


Figure 2.2: Central loop TEM setup in an internal coordinate system. Current in the source loop induces eddy currents in the earth, which response can be measured in the receiver loop.

The sources of the EM signals for TEM can both be insulated loops or grounded wires. Commonly, the current is turned on with slow a rise and a rapid turn-off, trying to mimic an instantaneous turn-off of a constant current. During the current on-time of the waveform, a primary magnetic field is generated. During the current off-time of the waveform, the primary magnetic field decays and an induction process starts. According to Faraday's law, Equation 2.1a, an electromotive force is generated depending on the decaying primary magnetic field, which induces eddy currents in the earth. The EM eddy currents decay due to Ohmic dissipation

into heat and consequently their induced magnetic fields decrease, continuing the induction process. The decaying secondary magnetic field, can then be measured by a magnetometer or as a voltage in an induction coil. Therefore the eddy currents diffuse down and outwards while the amplitude of the eddy currents decreases.

2.3.2 The central-loop TEM

It is beyond the scope of this thesis to derive the theory of the central loop TEM method, but the fundamental equations will be derived and solution the those are summarized and discussed. Árnason (1989) fully derives the theory of the central loop TEM, and the following section is based on this work.

A small horizontal coil with a varying current of $I = I_0 e^{i\omega t}$, with cross sectional area of A_s and number of wire windings n_s can be modeled as a magnetic dipole at the center point $\mathbf{x}_0 = (x_0, y_0, z_0)$ as

$$\mathbf{M} = M_0 e^{i\omega t} \hat{z} \delta(\mathbf{x} - \mathbf{x}_0) \quad (2.72)$$

where $M_0 = I_0 n_s A_s$ is the magnetic moment and $\delta(\mathbf{x} - \mathbf{x}_0)$ is the Dirac's delta function. The magnetic source has to be added to the magnetic field such that constitutive relationships becomes

$$\mathbf{B} = \mu(\mathbf{H} + \mathbf{M}) \quad (2.73)$$

In source free regions the constitutive relationship in Equation 2.2 holds and magnetization of the rocks is ignored. Using the relation in Equation 2.73, Faraday's law in Equation 2.1a becomes

$$\nabla \times \mathbf{E} = -\mu \frac{\partial \mathbf{H}}{\partial t} - \mu \frac{\partial \mathbf{M}}{\partial t} \quad (2.74)$$

For a horizontally layered earth, there is no charge density inside each layer and no charge build up occurs on the boundaries between layers. As in the MT case, Equation 2.16 holds. Taking this into account, a vector potential \mathbf{A}' is introduced such that

$$\mathbf{E} = \nabla \times \mathbf{A}' \quad (2.75)$$

Substituting Equation 2.75 into Equation 2.1b yields

$$\nabla \times \left(\mathbf{H} - \sigma \mathbf{A}' - \epsilon \frac{\partial \mathbf{A}'}{\partial t} \right) = 0 \quad (2.76)$$

where the quantity in the brackets can be written as gradient of a scalar potential ϕ' , this allows Equation 2.76 to be written as

$$\mathbf{H} = \sigma \mathbf{A}' + \epsilon \frac{\partial \mathbf{A}'}{\partial t} - \nabla \phi' \quad (2.77)$$

In the region containing the source, by substituting Equation 2.75 and 2.77 into Equation 2.74 yields

$$\nabla \times \nabla \times \mathbf{A}' + \sigma \mu \frac{\partial \mathbf{A}'}{\partial t} + \epsilon \mu \frac{\partial^2 \mathbf{A}'}{\partial t^2} - \nabla \cdot \frac{\partial \phi'}{\partial t} = -\mu \frac{\partial \mathbf{M}}{\partial t} \quad (2.78)$$

Equation 2.78, is a dynamic Equation with respect to \mathbf{A} and contains a term with the scalar potential ϕ' . By using the gauge condition for the scalar potential as

$$\nabla \cdot \mathbf{A}' = \frac{\partial \phi'}{\partial t} \quad (2.79)$$

and the identity from Equation 2.18, Equation 2.78 becomes

$$\nabla^2 \mathbf{A}' - \sigma \mu \frac{\partial \mathbf{A}'}{\partial t} - \epsilon \mu \frac{\partial^2 \mathbf{A}'}{\partial t^2} = \mu \frac{\partial \mathbf{M}}{\partial t} \quad (2.80)$$

Equation 2.80 is a dynamic Equation for the vector potential \mathbf{A}' .

2.3.3 TEM solution in a horizontally layered earth

Consider a horizontally layered earth, with $l = 0, 1, 2, \dots, N$ layers, and where each layer has a conductivity of σ_l and thickness d_l . It is assumed that within each layer that the magnetic permeability and dielectric permittivity are that of free-air, $\mu_l = \mu_0$ and $\epsilon_l = \epsilon_0$.

2 Theory of Electromagnetic methods

At a boundary between layers, boundary conditions from Equations 2.4, 2.5, 2.9 and 2.11 must be met. At a boundary between the l^{th} and $(l+1)^{th}$ layers, boundary conditions yield for the vertical component of \mathbf{A}' that

$$\sigma_l A'_l + \epsilon_0 \frac{\partial A'_l}{\partial t} - \frac{\partial^2 A'_l}{\partial z^2} = \sigma_{l+1} A'_{l+1} + \epsilon_0 \frac{\partial A'_{l+1}}{\partial t} - \frac{\partial^2 A'_{l+1}}{\partial z^2} \quad (2.81a)$$

$$\frac{\partial A'_l}{\partial x} = \frac{\partial A'_{l+1}}{\partial x} \quad \text{and} \quad \frac{\partial A'_l}{\partial y} = \frac{\partial A'_{l+1}}{\partial y} \quad (2.81b)$$

$$\frac{\partial \phi'_l}{\partial x} = \frac{\partial \phi'_{l+1}}{\partial x} \quad \text{and} \quad \frac{\partial \phi'_l}{\partial y} = \frac{\partial \phi'_{l+1}}{\partial y} \quad (2.81c)$$

Integrating conditions in Equations 2.81b and 2.81c gives

$$A'_l = A'_{l+1} \quad \text{and} \quad \phi'_l = \phi'_{l+1} \quad (2.82)$$

using the same time dependence as for the magnetic source, that is $V = Ve^{i\omega t}$ where V can be any of the time dependent EM fields or the vector or scalar functions. The source is located above the surface of the earth, in the 0^{th} layer, where conductivity is $\sigma = 0$. Equation 2.80 for the vertical component of the vector field can be written as

$$\nabla^2 A'_0 + k_0^2 A'_0 = i\omega\mu_0 \mathbf{M} \quad (2.83)$$

where $k_0^2 = \omega^2\mu_0\epsilon_0$ and \mathbf{M} is defined as in Equation 2.72. For all the layers within the earth, there is no magnetic source present. Due to this, in any of the $l = 1, 2, \dots, N$ layers in the earth, Equation 2.80 becomes

$$\nabla^2 A'_l + k_l^2 A'_l = 0 \quad (2.84)$$

where $k_l^2 = \omega^2\mu_0\epsilon_0 - i\omega\mu_0\sigma_l$ is the wave propagation constant. Equations 2.83 and 2.84 are time independent differential Equations for the vertical component of an arbitrary vector field that can be solved and connected back to the EM fields with Equations 2.75 and 2.77.

In Árnason (1989), Equations 2.83 and 2.84 are solved with the aid of Fourier transforms, converting the governing differential Equations into algebraic Equations. Equation 2.83 is solved as a combination of homogeneous and inhomogeneous differential equations, where the solution to the homogeneous part is essentially the same

as the solution to the homogeneous Equation 2.84. The solution provides a method of calculating the voltage in the receiver loop due to the magnetic fields induced by eddy currents caused by the current turn-off in the source loop.

2.3.4 Solution for central loop TEM

The solution for the voltage in the receiver loop after switching off a constant current I_0 in a circular transmitter loop can be calculated as

$$V(r, t) = \frac{2}{\pi} A_r n_r A_s n_s I_0 \frac{\mu_0}{2\pi r^3} \int_0^\infty \Re(E^e(\omega, r)) \cos(\omega t) d\omega \quad (2.85)$$

where A_r and n_r are the surface area and the number of windings in the receiver, A_s and n_s are the surface area and the number of windings in the source loop, t is the time from the current turn-off and r is the radius of the loop. Discussed in detail in Árnason (1989), the transient response in Equation 2.85 has to be calculated numerically. The electrical field E^e is an integral as well that needs to be evaluated numerically for a layered earth.

A common convention of presenting TEM data is to calculate late time apparent resistivity, similar to Equation 2.52 for MT data. The apparent resistivity can be calculated as

$$\rho_{app}(r, t) = \frac{\mu_0}{4\pi} \left(\frac{2\mu_0 A_r n_r A_s n_s I_0}{5t^{5/2} V(r, t)} \right)^{\frac{2}{3}} \quad (2.86)$$

3 Near surface induced Electromagnetic distortion

Distortion of EM fields from ideal 1D earth response due to variations in conductivity can best be described in terms of galvanic and inductive effects. In both cases we can, consider the distorted fields as a vector sum of a primary field, arising from the ideal earth model, and secondary field which is due to the distortion affects. When galvanic distortion occurs, the secondary electric field arises from electric charge build-up on boundaries of different conductivity. The primary and secondary fields are in phase and the effects from the distortion persist over all frequencies. In inductive distortion, the secondary fields arise from vortex currents within anomalous conductivity bodies. The currents are induced by time varying magnetic fields and the effects from the distortion persist over a finite range of frequencies, disappearing with lower frequency.

3.1 Static shift problem

A special case of distortion in the MT method is the static shift problem. Due to galvanic distortion arising from near surface structures, the measured electric fields for the whole frequency range are affected by a constant shift on a log scale. The effect produces apparent resistivity curves with the correct shape but they are incorrectly located on the vertical logarithmic apparent resistivity axes. Increased and decreased electric fields will result in upward and downward shift of the apparent resistivity, respectively (Jiracek, 1990). The main processes that cause static shift in MT measurements as proposed by Jiracek (1990), are discussed below.

3.1.1 Voltage distortion

A constant current flowing through a conductivity boundary yields a discontinuous electric field that depends on the conductivity contrast. Electric field measurements are done by measuring voltage differences over finite length, where the measured a

3 Near surface induced Electromagnetic distortion

voltage difference is defined as

$$V = \int_{r_1}^{r_2} \mathbf{E} dl \quad (3.1)$$

where r_1 and r_2 are points, with the distance of D between them. Equation 3.1 provides an average value of the electric field over the distance and assuming a homogeneous conductivity between the poles the electric field is a voltage difference divided by the distance between the electrodes.

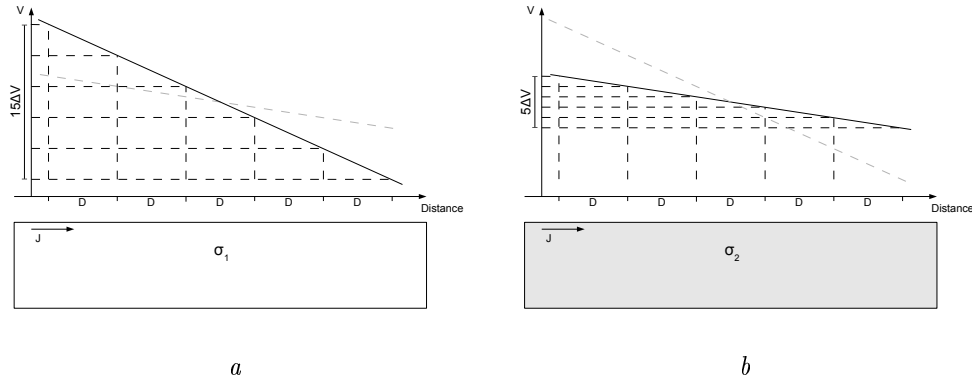


Figure 3.1: Voltage over a distance for two homogeneous half spaces of conductivity σ_1 and σ_2 in Figure a) and b), respectively.

Figure 3.1 shows two half spaces with constant conductivities of σ_1 and σ_2 . When a constant current flows in them, the voltage potential slope is constant. So all measurements of the voltage differences, when scaled with the distance will yield constant electric field. The electric field is related to the current via the Ohm's law, where $\mathbf{J} = \sigma_i \mathbf{E}$.

Figure 3.2 shows two examples of half-spaces embedded with blocks of width $2D$ of different conductivity. Figure 3.2a is a half-space of conductivity σ_1 embedded with a block of σ_2 and 3.2b is a half-space of conductivity σ_2 embedded with a block of σ_1 . The electric field are not constants, so when the voltage difference is measured over finite length it is clear that length and the relative location of the measurement reveal different voltages. Voltage difference measured over the length of $5D$ over the conductive anomaly (Figure 3.2a) yields an increased electric field compared to that of the halfspace (Figure 3.1b). Similarly, voltage measured over a resistive anomaly (Figure 3.2b) yields a decreased electric field compared to that of the electric field. The affect is more severe with dipole length in the same order

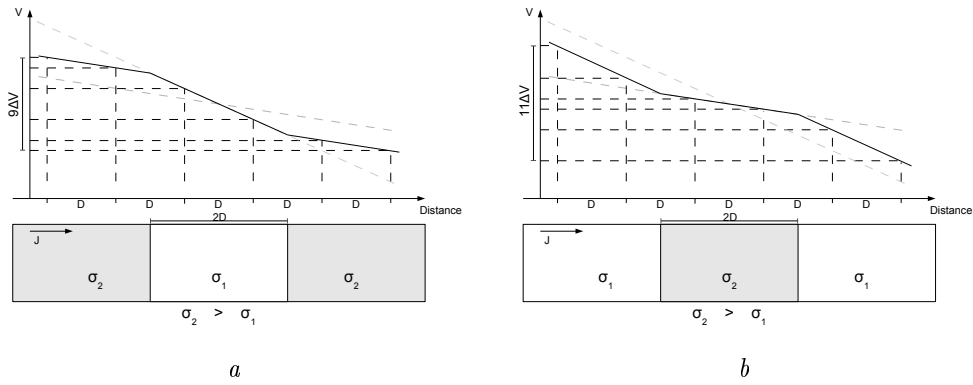


Figure 3.2: Shows voltage over a distance for an inhomogeneous space. Figure a) shows a resistive anomalous body and Figure b) shows a conductive anomalous body embedded in a halfspace. The whole black line is the voltage potential and the broken black lines indicate different potentials over a distance.

as the width of the anomaly. Increased distance between the voltage measurements filters out the effects and when it becomes much greater than the width of the anomaly the measured electric field approaches that of the half space.

3.1.2 Current distortion

When current flowing in a halfspace encounters a conductivity anomaly, the flow path is affected. The conductivity of the anomaly determines how the current is altered. Currents are channeled into a higher conductivity anomaly but are deflected from a lower conductivity anomaly.

Due to the primary electric field, charges build up on the boundaries of conductivity anomalies. The build up of charges depends on the conductivity of the anomalous region compared to its surroundings. In a resistive region, the positive charges accumulate on the side facing the primary electric field, inducing a secondary electric field in and around the conductivity anomaly. Within the resistive body, the secondary field is in the direction of the primary field (Figure 3.3 a). In a conductive anomaly, a negative charge buildup occurs on the side facing the primary electric field, inducing a secondary electric field that opposes the primary field (Figure 3.3 b). The distribution of secondary fields outside the anomalous body depends on the geometry of the primary fields. Is often said that currents are deflected away from a resistive anomaly (Figure 3.3 c) and channeled into a conductive body (Figure 3.3 d).

3 Near surface induced Electromagnetic distortion

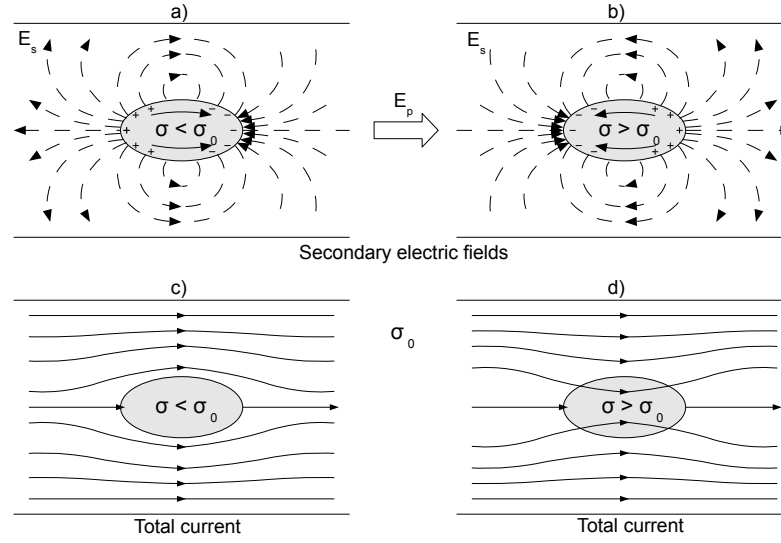


Figure 3.3: Shows current channeling and secondary induced electric fields due to an inhomogeneous conductivity. The induced secondary fields for a resistive and conductive anomalies in a) and b), respectively. The flow paths of the total current are shown in c) and d).

The total electric field is the sum of the primary and secondary fields. For the resistive anomaly (Figure 3.3 a)), it is clear that the total electric field is increased over the body, decreases from the sides, and is decreased of the ends. The total electric field around a conductive anomaly (Figure 3.3 b)), is decreased over the body, increases from the sides, and is increased of the ends.

3.1.3 Topographic distortion

Current flowing across topographic structures will be affected. The current flows into the hills and under the valleys, affecting the current density.

Figure 3.4 illustrates the galvanic effect for 2D hills and a valley of constant conductivity. The primary electric field causes charge build-up on the surface of the anomalous structures, where negative charges line the sides opposite the direction of the primary field and positive charges appear on the lee side. A secondary electric fields are induced in the hills in the opposing direction of the primary field, thus decreasing the total electric field on hills. In a valley bottom the secondary electric field is in the same direction as the primary field, increasing the electric field at the valley bottom.

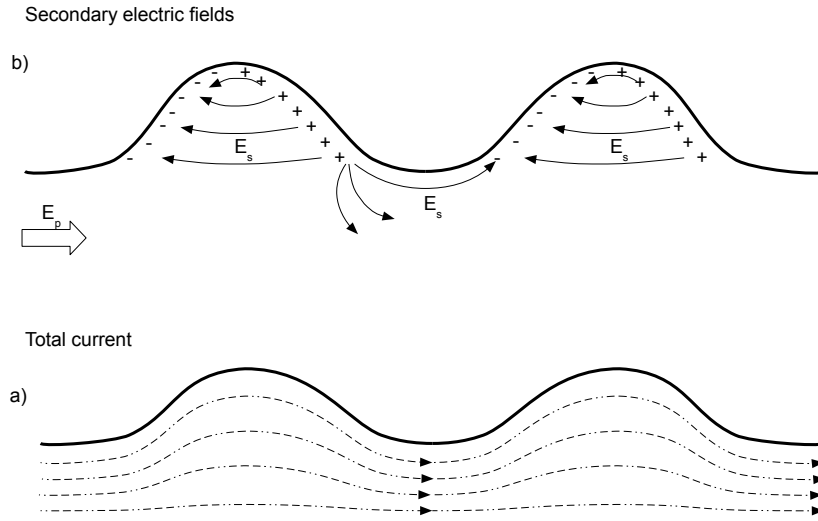


Figure 3.4: Shows total current and induced secondary electric field due to topography.

3.2 Correction of static shift

The causes of static shift can range widely, both where multiple processes and different structures give rise to unknown multipliers, S (shifts on log scale), of the apparent resistivity. In most cases those structures are not of great interest, but the interpretation of static shifted MT data will introduce errors in the results. Árnason et al. (2010), discusses that shift multiplier 0.1 in MT data, a 1D inversion will result in conductivity models that has an order of magnitude too high conductivity and 3 times too shallow depths of boundaries. This is illustrated in Figure 3.5, where forward modeled MT data for a layered earth has been multiplied with static shift multipliers of 10 and 0.1 and all of the data is then inverted. The recovered models are shown on the right side in Figure 3.5, where the inversion for the non-shifted data does well in recovering the original model. However, inversion of the static shifted data results in recovered models that are affected both in the values of resistivity and depth to the changes in resistivity. A static shift multiplier below 1 results in higher conductivities and decreased depth to boundaries and a multiplier above 1 results in lower conductivity and increased depth to boundaries.

Several ways have been proposed for correction of static shifts. The topic is widely covered in the literature, where (Jiracek, 1990, and references there in) give an overview of the static shift problem and discusses ways to account for the shift. Jiracek (1990) proposes the methods of correcting static shift and some other un-

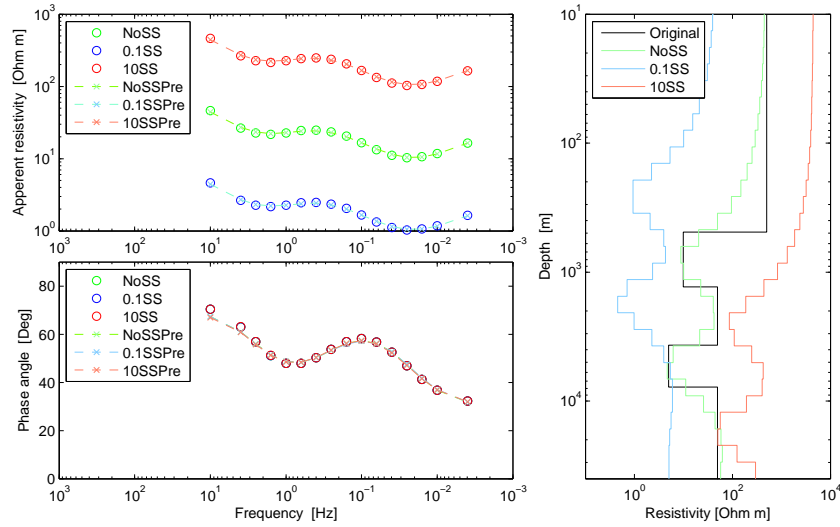


Figure 3.5: Shows 1D inversion results for data of layer model, that has been multiplied with static shift. The apparent resistivity and phase and their predictions are on the left and the resulting models on the right. The green curve is that of data without static shift, the red curve is that of data shifted by 10, blue is that of data shifted by 0.1 and the black is the original model.

wanted distortion to be classified into 6 categories that are discussed below.

Curve shift estimations

Curve shift estimates are the use of another measurement to estimate the static shift in MT measurements. TEM is commonly used for correcting static shift in MT measurements (Sternberg et al., 1988; Meju, 1996; Árnason, 2008). It has been shown that magnetic fields are relatively unaffected by near surface structures that cause static shift in MT measurements (Sternberg et al., 1988). Jointly inverting TEM and MT measurements and adding into the inversion a multiplier that estimates the shift of MT apparent resistivity curves has been found to be an effective way to deal with the static shift. The assumption that both the methods are measuring that same volume, allowing late time apparent resistivity curves from TEM soundings (Equation 2.86) to be compared to apparent resistivities of MT soundings (Equation 2.48). Magnetic transfer functions (Ledo et al., 2002) and direct current sensitives (Spitzer, 2001) have been used for static shift estimation with good results reported, but neither method is reported to be commonly used for static shift corrections in MT soundings.

Invariant combinations of the measured data

Using rotationally invariant combinations of the MT impedance has been proposed for estimation of the static shift (Jiracek, 1990). In order for the invariant combinations in Equations 2.59, 2.60 and 2.61 to be unaffected by static shift, the arithmetic and geometric averages of the static shift multipliers of the xy and yx impedance elements need to be equal to 1.

In Figure 3.6, apparent resistivity curves are shown for data from a layered model with various static shifts. In Figure 3.6a all the unshifted curves are in the same location, as $\rho_{xy} = \rho_{yx} = \rho_{det}$ for a layered earth. The static shifted xy mode, the light blue curve, is static shifted by 0.25 and the yx mode, the light red curve, is static shifted by 2. The determinant calculated from the static shifted impedances, the light green curve, is shifted by a factor of 0.71 away from the original data.

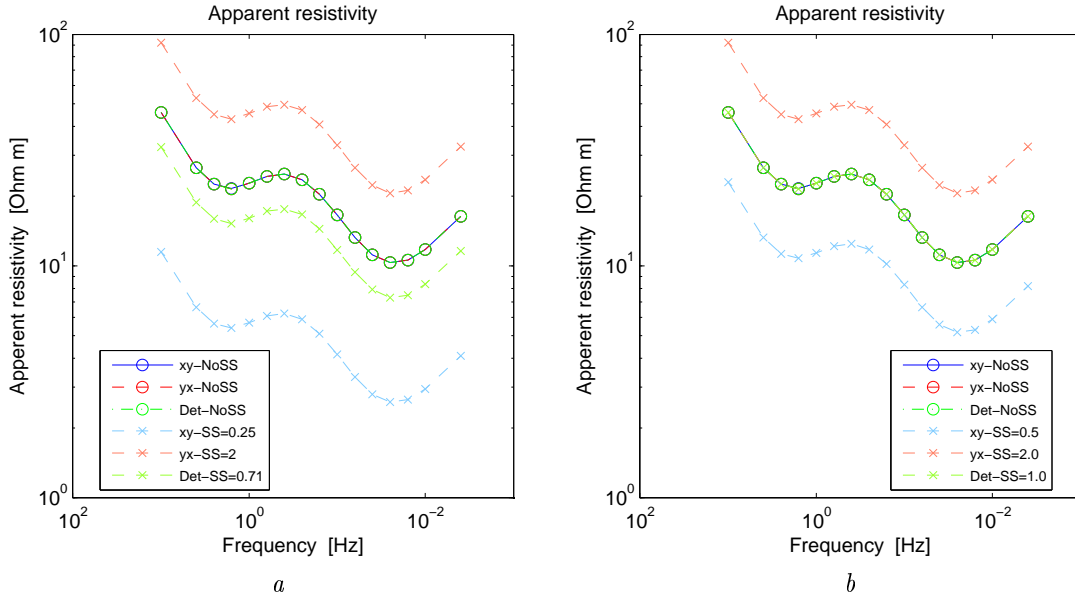


Figure 3.6: Shows apparent resistivities for data of a layered model, that has been multiplied by static shift. In a) the xy and yx modes are shifted by 2.0 and 0.25 and the determinant is static shifted by 0.71. In b) the xy and yx modes are shifted by 0.5 and 2 and the determinant by 1.0, or not shifted.

In Figure 3.6b unshifted curves are the same as in Figure 3.6a. Similarly, the static shifted xy mode, the light blue curve, is static shifted by 2.0 and the yx mode, the light red curve, is static shifted by 0.5. The determinant (the light green curve) falls onto the unshifted curves, since the xy and yx modes are shifted by equal amount on a log scale, in opposite direction. Figure 3.6 shows that static shift of the determinant, depends of the static shift of the xy and yx modes and therefore

the determinant can not be used as static shift invariant.

However, using an invariant combination gives a single mode that is a combination of the modes, so selecting a mode for interpretation becomes unnecessary. As well the invariant combinations preserve the property of true 1D measurements of being rotationally invariant.

Computer modeling

Since the causes of static shifts are of a multidimensional nature, interpreting the data to higher dimensional models provides the degree of freedom in the model to account for the static shift. The near surface of the model needs to be finely discretized to model the static shift adequately. That requires a mesh with a large number of cells, which decreases the practicality of the method. New 3D inversion codes are under constant development where the speed and feasible size of the problems are constantly being increased. Sasaki and Meju (2006) report on using 3D modeling on a synthetic example, where no static shift estimation is done. They also estimate static shift multipliers in the inversion that are statistically constrained (Sasaki, 2004). The conclusion of Sasaki and Meju (2006) is that by inverting for the static shift and conductivity simultaneously, artifacts due to static shift are reduced and the resolution of a synthetic test model is improved.

Spatial filtering

Spatial filtering of MT responses can be done with a 2D spatial wave number filters, similar to filters applied to gravity and magnetic data. The by filtering MT data with a low-pass spatial filter, filters out affects for galvanic distortion of small scale near surface conductivity structures. The electric field distortion can also be estimated by using continuous profile of electric dipoles. Variations of the electric field along the profile are sampled and a spatial low pass filter is used to filter out effects of the static shift along the profile. It relies on the assumption that the secondary electric fields along the profile is zero as the profile tends to infinity. Practical measurements use finite profile lengths, leading to a bias in the method especially if the profile ends on an anomaly (Simpson and Bahr, 2005).

Statistical averaging

The static shift of the MT soundings over a survey can be estimated using a statistical constraint on the static shift multipliers. deGroot Hedlin (1991) suggested

using regularized 2D Occam inversion, where additional static shift parameter is estimated during the inversion. Additionally it is assumed that the product of the static shift multipliers is close to 1, leading to that on average there is no static shift along the profile. Ogawa and Uchida (1996) use similar methodology, but assume that static shift multipliers have a log Gaussian distribution around zero. Sasaki (2004) expands into 3D inversion, inverting for the static shift parameter that is constrained by Gaussian normal distribution. These methods show improved recovery of models, but do not address that in most practical examples the static shift multipliers estimated by using the TEM method show a non Gaussian distribution nor have average of static shift multipliers close to 1 on a log scale.

Decomposition of the tensor data

Decomposing the impedance tensor to elements of distortion parameters and non affected impedance have been developed. The commonly used method is that of Groom and Bailey (1989), where the tensor is separated into localized 3D effects and regional 2D effects. The impedance tensor is factorized in terms of a rotation matrix \mathbf{B} , and distortion tensor, \mathbf{C} such that

$$\mathbf{Z} = \mathbf{RCZ}_{2D}\mathbf{R}^T \quad (3.2)$$

where $\mathbf{C} = g\mathbf{TSA}$, with \mathbf{T} as twist, \mathbf{S} as shear and \mathbf{A} as local anisotropy. The decomposition problem in Equation (3.2) is a ill-posed problem of 9 unknowns and 8 knowns. The solution requires numerical estimation of the elements, where noise in the data affects the accuracy of the results. Further, the method does not estimate the static shift multiplier and external estimation is required.

The assumptions used in each of these methods vary greatly and the performance is determined by how well the assumptions hold. It is therefore important to determine the appropriate method on individual survey basis, where geological features and practical demands need to be considered.

3.3 Use of TEM for static shift estimations in geothermal exploration

The geological setting of geothermal areas are complex and the areas are often associated with volcanic centers. The surface often consists of varying conductivities,

leading to high degree of static shift in MT soundings. It is a standard practice to collect TEM and MT soundings in close proximity to one another for estimation of static shift with joint 1D inversion (Eysteinnsson et al., 2010; Cumming and Mackie, 2010).

Estimations of static shift multipliers, S_{xy} and S_{yx} , can be calculated from joint inversion of the xy and yx polarizations, respectively. The impedance tensor can be corrected for static shift by matrix multiplication as in Árnason et al. (2010), that is a simple presentation of total static distortion discussed in Groom and Bailey (1989). The corrected tensor, \mathbf{Z}^c , is given by

$$\begin{bmatrix} Z_{xx}^c & Z_{xy}^c \\ Z_{yx}^c & Z_{yy}^c \end{bmatrix} = \begin{bmatrix} C_x & 0 \\ 0 & C_y \end{bmatrix} \begin{bmatrix} Z_{xx} & Z_{xy} \\ Z_{yx} & Z_{yy} \end{bmatrix} \quad \text{where } C_x = \sqrt{\frac{1}{S_{xy}}} \quad \text{and} \quad C_y = \sqrt{\frac{1}{S_{yx}}} \quad (3.3)$$

Estimating S_{xy} and S_{yx} multipliers for all the soundings that are intended to be used in the 3D inversion, then Equation 3.3 can be used for correcting the static shift. By doing this, the effects of static shift may be corrected from the MT soundings prior to the 3D inversion. The assumptions of one dimensionality of the near-subsurface and correlation of measured values for TEM and MT methods must hold when using this procedure. In the great majority of cases a model can be found with satisfactory misfit between the measured and calculated TEM and MT data. In some cases acceptable misfit in a joint 1D inversion is hard to achieve, often due to bad data or multidimensional effects, that can lead to misleading estimations. Removing data from the inversion and adjusting error estimations are commonly used procedures to improve the misfit, but they are very dependent on the choices made.

4 Modeling of Electromagnetic data

4.1 Inversion of geophysical data

The goal of any geophysical exploration is to obtain information about the subsurface, in order to find a target of interest. In some cases the measured data may be interpreted directly to provide answers to some questions about the geology and the target of interest, but often further interpretation is necessary. Coming up with a more detailed structure of the physical properties that explains the measured data is desirable.

Forward modeling is the process of computing responses for a physical property distribution, which can be 1D, 2D or 3D. Constant physical properties are assigned to each cell in a model, m , and physical relationships enable us to calculate data resulting from m . Popular ways of discretization are using rectangular or triangular meshes, but the formulation of the calculations depends on the mesh.

An inversion problem uses the forward modeling to find a physical property model where the misfit between the predicted and measured data is at a desired level. The data misfit is calculated with the misfit functional

$$\phi_d = \sum_{i=1}^N \left(\frac{d_i^{meas} - d_i^{pred}}{\sigma_i} \right)^2 \quad (4.1)$$

where N is the number of data, d^{meas} is the measured data, d^{pred} is the predicted data and σ is the standard deviation estimate of the errors for the difference of the measured and predicted data. Assigning exact errors is next to impossible, so using a simple assumption of independent Gaussian errors with a zero mean and standard deviation of σ is often used. The assignment of σ needs to account for different sources of noise, such as repeatability, surveying, and modeling errors, that have an unknown correlation. If the estimates of the standard deviations are good, then the target misfit of Equation 4.1 is equal to the number of data, N .

The difficulty of non-uniqueness arises in the inversion problem. Typically the inverse problem is largely underdetermined. This means that there are far fewer data than there are degrees of freedom in the model. Many models can produce data within the desired data misfit. Additional constraints and regularization must be introduced to be able to find a meaningful model. The choice of the regularization is an important part of the inversion. Commonly, the inversion is regularized to find a model that has a small perturbation and smooth compared to a user defined reference model. The model objective functional that is often used

$$\phi_m = \alpha_s \int_{\Omega} w_s (m - m_{ref})^2 dV + \alpha_r \int_{\Omega} w_r \left(\frac{d(m - m_{ref})}{dr} \right)^2 dV \quad (4.2)$$

m_{ref} is the reference model constructed from geological and a priori information. w_s is the smallness weighting and w_r is the directional smoothness weighting. The directions used are typically the x, y and/or z directions in the model. α_s and α_r are the trade off parameters controlling the relative importance between the smallness and the smoothness and Ω is the discretized domain. The inverse problem is defined as the minimization of a functional $\Phi(m)$, that is a combination of the data and the model functionals in Equations 4.1 and 4.2, respectively. The inversion minimizes

$$\Phi(m) = \phi_d(m) + \beta \phi_m(m) \quad (4.3)$$

where β is the trade-off parameter or Tikhonov parameter, controlling relative importance of the model functional in the objective function in Equation 4.3. The value of β is chosen such that when $\Phi(m)$ is at a minimum, $\phi_d(m)$ equals then number of data, N (Oldenburg and Li, 2005).

4.2 Forward and inverse modeling codes used

4.2.1 1D TEM and MT inversion code - TEMTD

The program TEMTD performs 1D inversion for TEM and MT data for a horizontally layered earth, both individually for each sounding method and joint inversion of both sounding methods. The program gives the option of using voltage or apparent resistivities for the TEM data and apparent resistivity and/or phase for the MT data. At the start of the inversion a starting model has to be supplied, which can be halfspace or a user specified model. A built in help in the program, prompted by the -h flag, list all the options that can be used in the program. Additionally

Árnason (2006) gives further explanation to the performance of the program, file formats and explains the use of options for the inversion.

For forward modeling of MT data, the recursion relationship in Equation 2.37 is used to calculate impedance for the layered model for a natural source EM waves. The impedance responses can be further calculated to apparent resistivity and phase with Equations 2.48 and 2.49, respectively. Forward modeling TEM data, Equation 2.85 can be used to calculate voltage responses in the receiver loop that may be presented as late time apparent resistivity with Equation 2.86. The source loop is assumed to be a square, formed out of multiple dipole segments, with the receiver located at the center. The current wave form in the source loop, is a half-duty bipolar semi-square wave, with exponential turn-on and linear current turn-off.

For the inverse modeling, a Levenberg-Marquardt non-linear least square inversion is used as described in Árnason (1989). The objective function as in Equation 4.3 becomes

$$\Phi_{1D}(m) = ||W_d(F(m) - d_{meas})||^2 + \alpha \frac{dm}{dz} + \beta \frac{d^2m}{dz^2} + \gamma \frac{dD}{dz} + \delta \frac{d^2D}{dz^2} \quad (4.4)$$

where W_d a diagonal matrix containing the ratio of the standard deviations for the measured data, $F(m)$ is the forward model operator applied to model and D is the layer depths. The parameters α , β , γ and δ are the relative importance of each of the damping parameters. The inversion searches for conductivities of the layers as well as finding the optimal thickness of each layer.

The program can also perform Occam inversion, for the minimum structure (Constable et al., 1987). The objective function in the Occam inversion becomes

$$\Phi_{Occ}(m) = \left\| \frac{dm}{dz} \right\|^2 + \mu^{-1} [(||W_d(F(m) - d_{meas})||^2 - X_*^2)] \quad (4.5)$$

where the X_* is the desired level of data misfit and μ is the Lagrange multiplier. A solution at the $k^{th} + 1$ iteration for m is

$$m_{k+1}(\mu) = \left(\mu (\mathbf{D}^T \mathbf{D} + \mathbf{J}_k^T \mathbf{W}_d^T \mathbf{W}_d \mathbf{J}_k)^{-1} \mathbf{D}^T \mathbf{D} + \mathbf{J}_k^T \mathbf{W}_d^T \mathbf{W}_d \right) \hat{\mathbf{d}} \quad (4.6)$$

where D is the divergence operator, $J_k = \nabla \cdot_m F(m_k)$ is the Jacobian matrix, T notes a matrix transpose and $\hat{\mathbf{d}}$ is data vector as used in Constable et al. (1987),

defined as

$$\hat{\mathbf{d}} = ||W_d(F(m_k) + \mathbf{J}_k m_{k+1} - \mathbf{J}_k m_k - d_{meas})||^2 - X_*^2 \quad (4.7)$$

When the k^{th} iteration has been completed, a model m_{k+1} is obtained by Equation 4.6. The value of μ is selected by minimizing the $\Phi_{Occ}(m)$ for m_{k+1} such that $\phi_d \cong X_*^2$.

4.2.2 3D TEM forward code - H3DTD

For 3D forward modeling for the TEM method, the program H3DTD is used developed at University of British Columbia under the MITEM (Multi-source Inversion of Time Domain Electromagnetic data) consortium (H3DTD manual, 2010). H3DTD is a software package for solving Maxwell's Equations in the time domain for multiple sources. The sources can be grounded dipoles or loop currents anywhere within the model with a user-defined transmitter waveform without any restrictions on the length or shape. The responses can be any of \mathbf{E} , \mathbf{H} , or $\frac{d\mathbf{B}}{dt}$, calculated in the "on-time" or "off-time" of the current waveform for anywhere within the model.

For the solution of the 3D TEM forward problem for multiple sources, Maxwell's Equations 2.1 are written as

$$\nabla \times \mathbf{E}^i + \mu \frac{\partial \mathbf{H}^i}{\partial t} = 0 \quad (4.8a)$$

$$\nabla \times \mathbf{H}^i - \sigma(r)\mathbf{E}^i - \epsilon \frac{\partial \mathbf{E}^i}{\partial t} = \mathbf{s}_r^i(t) \quad (4.8b)$$

for $i = 1, \dots, N$ where N is the number of transmitter sources, \mathbf{E}^i and \mathbf{H}^i are the electric and magnetic fields from the source \mathbf{s}_r^i , μ is the magnetic permeability, ϵ is the dielectric permittivity and $\sigma(r)$ is the location dependent conductivity.

For the system of Equations 4.8, the time derivative is approximated with a backward Euler discretization in time over a time step $\delta t = t^{j+1} - t^j$. In the time step, the

system becomes

$$\nabla \times \mathbf{E}^{j+1} + \mu \frac{\mathbf{H}^{j+1} - \mathbf{H}^j}{\delta t} = 0 \quad (4.9a)$$

$$\nabla \times \mathbf{H}^{j+1} - \sigma(r)\mathbf{E}^{j+1} - \epsilon \frac{\mathbf{E}^{j+1} - \mathbf{E}^j}{\delta t} = \mathbf{s}^{r_j} \quad (4.9b)$$

and by eliminating the electrical field \mathbf{E}^{j+1} and using that $\nabla \cdot \mu \mathbf{H} = 0$ yields

$$\begin{aligned} \nabla \times (\sigma + \delta t^{-1}\epsilon)^{-1} \nabla \times \mathbf{H}^{j+1} - \mu \nabla \mu^{-2} (\sigma + \delta t^{-1}\epsilon)^{-1} \nabla \cdot (\mu \mathbf{H}^{j+1}) \\ + \frac{\mu}{\delta t} \mathbf{H}^{j+1} = \mathbf{rhs}^{j+1} \end{aligned} \quad (4.10)$$

where \mathbf{rhs} is the right hand side, containing the information about the sources and the previous time step. Equation 4.10 is solved by discretizing the conductivities on to a rectangular grid where the conductivity is constant for each cell. The differential operators in Equation 4.10 are discretized with finite volume methods such that

$$\begin{aligned} A(\sigma, \delta t) \mathbf{H}^{j+1} &= (CRC - \tilde{\mu} G \tilde{\mu}^{-2} R D + M) \mathbf{H}^{j+1} \\ &= (K(\sigma, \delta t) + M) \mathbf{H}^{j+1} = \mathbf{rhs} \end{aligned} \quad (4.11)$$

where $R = (\sigma + \delta t^{-1})$, $M = \frac{\mu}{\delta t}$ and $\tilde{\mu}$ is the distribution of magnetic permeability. C, G and D represent discretization of the curl, gradient and divergence matrix operators, respectively (Haber et al., 2000a). The $A(\sigma, \delta t)$ matrix is singular, positive definite and for identical time steps (δt), only the right hand side changes in Equation 4.11. The A matrix can be decomposed as

$$A(\sigma, \delta t) = LL^T \quad (4.12)$$

The factorization is done with Multi-frontal Massively Parallel Solver (MUMPS) (Amestoy et al., 2006) and is computationally heavy, but once it is completed it can be used to solve the system in Equation 4.11 for multiple right hand sides very quickly. When calculating the TEM response for multiple transmitters this technique can be superior to iterative techniques of solving the system (Oldenburg et al., 2008).

4.2.3 3D MT forward code - MT3Dfwd

For 3D forward modelling for the MT method, the program MT3Dfwd is used. MT3Dfwd was developed at the University of British Columbia under the IMAGE (Inversion and Modelling of Applied Geophysical Electromagnetic data) consortium (MT3Dinv manual, 2010). MT3fwd is a modified version of the finite-volume, staggered-grid algorithm presented for a controlled source case in Haber et al. (2000a). A theoretical background of the forward problem is given in Farquharson et al. (2003, 2002) and practical description is given in MT3Dinv manual (2010).

For the solution of the 3D MT forward problem, introducing a decomposition of the electrical field as $\mathbf{E} = \mathbf{A} + \nabla\phi$ into Equation 2.21 yields

$$\nabla^2 \mathbf{A} + i\omega\mu_0\sigma(\mathbf{A} + \nabla\phi) = 0 \quad (4.13)$$

where \mathbf{A} is a vector field and ϕ is scalar field. As well, the electric and magnetic fields are separated into primary and secondary fields as

$$\mathbf{E} = \mathbf{E}_s + \mathbf{E}_p \quad (4.14a)$$

$$\mathbf{H} = \mathbf{H}_s + \mathbf{H}_p \quad (4.14b)$$

The primary fields, \mathbf{E}_p and \mathbf{H}_p , exist in a background conductivity model with conductivity of σ_b and inhomogeneous boundary conditions are imposed that satisfy Maxwell's Equations. The secondary fields, \mathbf{E}_s and \mathbf{H}_s exist due to a difference between the actual conductivity σ and background conductivity, σ_b . Similarly, the vector and scalar potentials in Equation 4.13 can be split into primary and secondary parts.

$$\mathbf{A} = \mathbf{A}_s + \mathbf{A}_p \quad (4.15a)$$

$$\phi = \phi_s + \phi_p \quad (4.15b)$$

Introducing the decomposition in Equations 4.15a and 4.15b into Equation 4.13 yields

$$\begin{aligned}
 & \nabla^2(\mathbf{A}_p + \mathbf{A}_s) + i\omega\mu_0\sigma(\mathbf{A}_p + \mathbf{A}_s + \nabla\phi_p + \nabla\phi_s) = 0 \\
 \Rightarrow & \nabla^2\mathbf{A}_s + i\omega\mu_0\sigma(\mathbf{A}_s + \nabla\phi_s) = -\nabla^2\mathbf{A}_p - i\omega\mu_0\sigma(\mathbf{A}_p + \nabla\phi_p) \\
 \Rightarrow & \nabla^2\mathbf{A}_s + i\omega\mu_0\sigma(\mathbf{A}_s + \nabla\phi_s) = -i\omega\mu_0\Delta\sigma\mathbf{E}_p
 \end{aligned} \tag{4.16}$$

where $\Delta\sigma = \sigma - \sigma_b$ is the conductivity difference and the solution of the background model, $\nabla^2\mathbf{A}_p = -i\omega\mu_0\sigma_b(\mathbf{A}_p + \nabla\phi_p)$, is used. Introducing Equations 4.15a into Equation 2.16 yields

$$\nabla \cdot (\sigma \mathbf{A}_s) + \nabla \cdot (\sigma \nabla \phi_s) = -\nabla \cdot \Delta(\sigma \mathbf{E}_p) \tag{4.17}$$

Equations 4.16 and 4.17 are the simultaneous equations that are solved during the MT forward modeling. The model is discretized on a rectangular grid where the conductivity is constant for each cell, the scalar potential (ϕ) is calculated at the cell centers and the vector potential (\mathbf{A}) is calculated at the centers of the cell faces. A system of equations for all the cells in the domain is obtained by using a finite volume technique for Equations 4.16 and 4.17 (Haber et al., 2000a), yielding a matrix system

$$\begin{bmatrix} L + i\omega\mu_0 S & i\omega\mu_0 SG \\ DS & DSG \end{bmatrix} \begin{bmatrix} A_s \\ \phi_s \end{bmatrix} = \begin{bmatrix} -i\omega\mu_0 \Delta S E_p \\ -D \Delta S E_p \end{bmatrix} \tag{4.18}$$

Here L, G and D represent discretization of the Laplacian, gradient and divergence matrix operators, respectively (Haber et al., 2000a). S is the averaged cell conductivities and $\Delta S = S - S_p$ is the difference between averages of the actual model and the background. The matrix Equation in 4.18 are solved using stabilized bi-conjugate gradient algorithm.

The final step of the forward modeling is to calculate the electric and magnetic fields for two different source field polarizations, x- and y-direction magnetic source fields. With superscripts 1 and 2 represent the x and y directed source fields then the impedance tensor is calculated as a function of position and frequency by solving

$$\begin{bmatrix} E_x^1(\omega) & E_x^2(\omega) \\ E_y^1(\omega) & E_y^2(\omega) \end{bmatrix} = \begin{bmatrix} Z_{xx}(\omega, r) & Z_{xy}(\omega, r) \\ Z_{yx}(\omega, r) & Z_{yy}(\omega, r) \end{bmatrix} \begin{bmatrix} H_x^1(\omega) & H_x^2(\omega) \\ H_y^1(\omega) & H_y^2(\omega) \end{bmatrix} \tag{4.19}$$

The data can be selected to be impedances or be presented as apparent resistivities and phases calculated for direction $i, j = x, y$ as

$$\rho_{ij}^{app} = \frac{1}{\omega\mu_0}|Z_{ij}|^2 \quad and \quad \phi_{ij}^{app} = \arctan\left(\frac{\Im(Z_{ij})}{\Re(Z_{ij})}\right)$$

4.2.4 MT 3D inversion code - MT3Dinv

The inversion algorithm in MT3Dinv minimizes the combination in Equation 4.3, that contains the data misfit functional 4.1 and the model objective functional 4.2. The minimization problem is solved using an iterative Gauss-Newton procedure, that is based on a linearized approximation of the relations of the model parameters and measured data. The procedure is based on algorithms used for the controlled source problem (Haber et al., 2000b).

The model objective functional used in MT3Dinv is a combination of smallness and smoothness constraints as

$$\begin{aligned} ||\mathbf{W}_m(\mathbf{m} - \mathbf{m}_{ref})||^2 &= \alpha_s ||\mathbf{W}_s(\mathbf{m} - \mathbf{m}_{ref})||^2 \\ + \alpha_x ||\mathbf{W}_x(\mathbf{m} - \mathbf{m}_{ref})||^2 &+ \alpha_y ||\mathbf{W}_y(\mathbf{m} - \mathbf{m}_{ref})||^2 + \alpha_z ||\mathbf{W}_z(\mathbf{m} - \mathbf{m}_{ref})||^2 \end{aligned} \quad (4.20)$$

where the \mathbf{W}_s is the smallness weight matrix and \mathbf{W}_x , \mathbf{W}_y and \mathbf{W}_z are first order finite-difference weighting matrices in the x-, y- and z-directions in the model, respectively. The α constants control the importance of each of the terms and the model vector contains the logarithms of the cell conductivities. The objective function that is minimized in the inversion is

$$\Phi(\mathbf{m}) = ||\mathbf{W}_d(\mathbf{d}_{meas} - \mathbf{d}_{pred})||^2 + \beta ||\mathbf{W}_m(\mathbf{m} - \mathbf{m}_{ref})||^2 \quad (4.21)$$

where \mathbf{d}_{meas} is the vector of the measured data, \mathbf{d}_{pred} is the vector of the predicted data calculated by solving Equation 4.18, β is the trade-off parameter and $||\cdot||$ is the l_2 -norm. At the $(n+1)^{th}$ iteration step of the minimization of the $\Phi(\mathbf{m})$, the Gauss-Newton method requires the solution of

$$(\mathbf{J}^T \mathbf{W}_d^T \mathbf{W}_d \mathbf{J} + \beta \mathbf{W}_m^T \mathbf{W}_m) \delta \mathbf{m} = -\mathbf{J}^T \mathbf{W}_d^T \mathbf{W}_d (\mathbf{d}_{meas} - \mathbf{d}_{pred}^n) - \beta \mathbf{W}_m^T \mathbf{W}_m (\mathbf{m}_n - \mathbf{m}_{ref}) \quad (4.22)$$

where \mathbf{m}_n is the model vector for the n^{th} iteration, and \mathbf{J} is the Jacobian matrix of sensitivities. $\delta \mathbf{m}$ is the model perturbation, once found is used to update \mathbf{m} .

Equation 4.22 is solved with a inexact preconditioned conjugate gradient algorithm, using a LU decomposition of $(\mathbf{W}^T \mathbf{W} + 0.1 \mathbf{I})$ as a preconditioner. By solving the problem with the procedure described above, requires only the operations of $\mathbf{W}^T \mathbf{W}$, \mathbf{J} and \mathbf{J}^T on to a vector, done with sparse matrix-vector operations (Farquharson et al., 2002).

5 Geothermal exploration with Electromagnetic methods

The exploration of geothermal energy poses a challenge. Geothermal systems are open, with multiple processes continually evolving the system. Within a geothermal environment, multiple processes and rock properties over a great range of depths and distances define the system. Convection of water and conduction of heat from the hot rocks to the water are important elements which allow for the utilization of the resource. Target zones in geothermal systems where fluids can be extracted for electricity production span depths of 1000-3500 m, have temperatures in the range of $250 - 350^{\circ}\text{C}$, and permeability is sufficient to allow for enough fluids to be extracted. Gaining information about the geothermal system over as large an area as possible in a wide depth range is beneficial for defining and managing the geothermal resource.

5.1 Resistivity structure of geothermal systems

Geothermal systems, can be thought of as localized zones close to the surface of the Earth containing abundant heat in the ground and sufficient network of pores and fractures for fluids to flow in, such that the heat may be transferred by convection to the surface. Geothermal systems are frequently associated with plate tectonic boundaries, where heat originates from igneous or volcanic events and fracturing occurs due to the movement of the plates. When fluids are present within the warm and fractured zone, a geothermal system is developed.

The resistivity structure of high temperature geothermal systems has been reported to have similar characteristics (e.g Arnason et al., 2000; Ussher et al., 2000). Typically, there is low resistivity cap at the outer limits of the geothermal system with more resistive core towards the center of the system. This character is found both in fresh water and saline geothermal systems but the overall resistivity is lower in saline systems. The resistivity of water-saturated rocks is related to many attributes or parameters such as porosity, temperature, conductivity of the rock matrix, thermal alteration and salinity of the saturation fluids. These parameters play a complex

role in the bulk resistivity of the rock that is not fully understood. A formula that could explain and connect all the different processes that affect the bulk resistivity is bound to have many free parameters which are hard to factor individually in a sufficient manner.

A correlation between the resistivity structure and the hydrothermal alteration of the rocks in geothermal systems is discussed in Arnason et al. (2000) and Flóvenz et al. (2005). The boundary of the low resistivity coat and the higher resistivity core has been found to correlate with the change from smectite to chlorite dominated alterations. This alteration change is known to occur at a temperature of approximately 230°C .

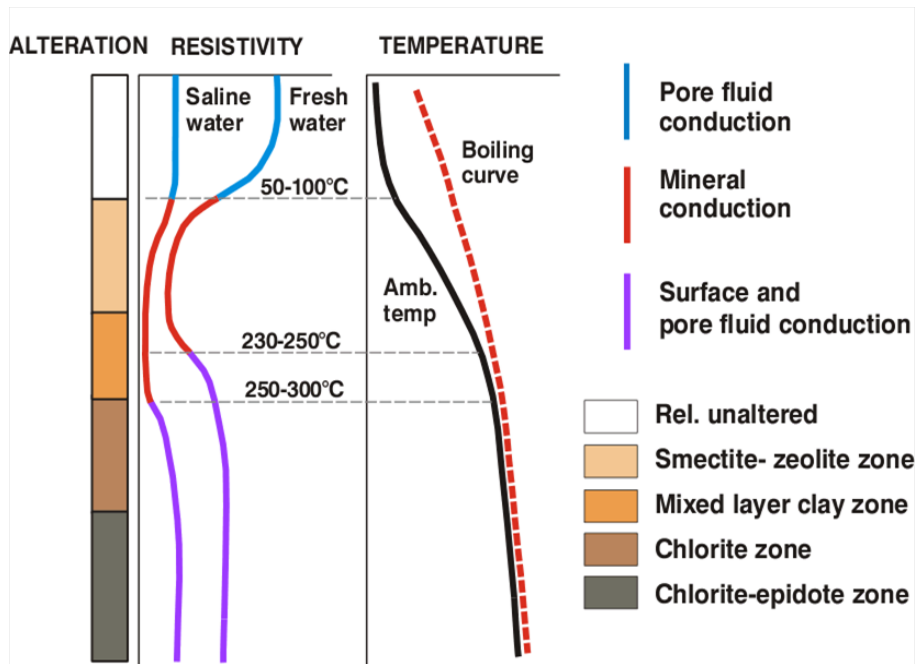


Figure 5.1: Figure of general resistivity structure and alteration of basaltic crust in Iceland. (From Flóvenz et al. (2005))

Figure 5.1 shows the general correlation alteration, resistivity and temperature for basaltic crust in Iceland. The relationship presented is both based on laboratory data covered in Flóvenz et al. (2005) and experience in Iceland and elsewhere (Arnason et al., 2000). For temperatures lower than $50 - 100^{\circ}\text{C}$ the resistivity is high in mainly unaltered rocks. In this alteration zone the conduction of current in the rocks is in the pore fluid. The salinity of the fluids determines the overall range of the resistivity, where more salinity leads to lower overall resistivity. When the temperature ranges from $100 - 230^{\circ}\text{C}$, smectite-zeolite alterations become dominant, the resistivity decreases and the conduction is mostly in the minerals of the pore walls. As the temperature increases further and ranges from $230 - 250^{\circ}\text{C}$ in fresh water systems and $250 - 300^{\circ}\text{C}$ in saline systems, the zeolites disappear and

smectite is gradually being replaced by chlorite in the mixed layer clay zone. When this happens, the resistivity increases due to decreased cation exchange capacity of the clay minerals. Above 300°C , resistivity slowly increases as the temperature increases.

Caution must be taken when interpreting temperature from resistivity data through the hydrothermal alteration as discussed above. The alteration may be fossil in the system. This means that the zone of alteration changing from zeolites-smectite to chlorite (where the top of the resistive core of the system is located) can only be interpreted to have been exposed to temperatures of $230 - 250^{\circ}\text{C}$ at some time during the thermal history of the geothermal system. Without supplementary data, exact thermal state of the geothermal system cannot be determined.

5.2 Application of EM methods

The exploration target in resistivity is the change in the resistivity associated with the change in alteration and conduction processes, as described above. Hersir and Björnsson (1991) gives an overview of basic theory and application of geophysical methods for geothermal exploration, among them the MT and TEM methods. Wright et al. (1985) discuss similarly state-of-the-art geophysical methods and methodologies in the year 1985, some of their drawbacks, and give a list of publications where the methods have been used in geothermal exploration. Pellerin et al. (1996) focus on theoretical and numerical evaluation of EM methods for geothermal exploration, without practical considerations such as cost and noise in data. The conclusions of Pellerin et al. (1996) indicate that methods that use both electrical and magnetic field measurements, such as MT, are superior to methods that only rely on magnetic field measurements. A combination of methods is suggested, such as using methods that economically provide information about the shallow resistivity structure in combination with deep sounding method. This provides the resistivity structure of great range of the geothermal system. Multidimensional interpretations is strongly recommended.

The use of TEM and/or MT soundings is widely reported for geothermal exploration, for example in Iceland (Árnason et al., 2010; Hersir et al., 2010; Rosenkjær and Karlsdóttir, 2008; Karlsdóttir et al., 2008) and worldwide (Cumming and Mackie, 2010; Raharjo et al., 2010; Manzella et al., 2010; Newman et al., 2008; Uchida, 2005). These references are a small fraction of the literature that deals with resistivity measurements in geothermal exploration, but provide a similar story of methodology and recovered models. The environments of the geothermal systems are complex, where most of them are situated in active volcanic and/or tectonic zones. The use of a combination of MT and TEM soundings to delineate resistivity structures has become

a standard practice. The joint application of the TEM and MT methods overcomes shortcomings of the individual sounding methods and allows for interpretation from near surface to depths of tens of km.

The inversion of the TEM and MT data is an important step in the interpretation of the measured data. 1D inversion of TEM or MT soundings separately and joint inversion of TEM and MT has traditionally been used in geothermal exploration due to the simplicity and accessibility of the computation. A common way to present MT data in 1D is to use one of the rotationally invariant combinations of the impedance tensor, as in equations 2.59, 2.60 and 2.61 in section 2.2.5. Stacking the resulting layer models into a cross-sections, iso-depth maps or 3D models by using mathematical interpolation, can provide a fairly accurate resistivity model. As long as the limitations of the 1D inversions are kept in mind (such as carefully interpreting models below the low resistivity coat, near boundaries of conductors or zones of low data coverage), the 1D MT inversion can support the quality assurance and interpretation process (Cumming and Mackie, 2010). 2D inversion of MT data allows for incorporation of multidimensionality in the inversion without requiring a full 3D inversion. Assumptions about the orientation of the electrical strike are needed. The MT soundings have to be oriented along and across the electrical strike direction such that equation 2.51 approximately holds. In many cases this can be a time consuming and demanding task for a data set collected in geothermal exploration. Even though 3D inversion is usually more appropriate, 2D inversion has advantages of less computational requirements allowing for better resolution and better testing of the results. Development of faster 3D inversion codes and with better computers, 3D inversion is becoming more feasible as a routine procedure in geothermal exploration. The nature of geothermal areas is commonly highly 3D, so the use of 3D inversion is most suitable. The 3D inversion is limited by the time an inversion takes to complete, which is dependent on the size of the problem, the number of frequencies and the discretization of the model.

The ability of MT soundings to measure at depths extending from the near surface to great depths gives the method an advantage over most other EM methods in geothermal exploration. It easily detects the low resistivity coat in geothermal systems but it can also provide valuable information on the resistivity structure at greater depths, which could associated with heat sources and deep hot spots. The collection of MT data is logistically simple compared to controlled source methods, that allows for fast and relatively inexpensive field campaigns. Interpretation can be done in 1D, 2D or full 3D providing valuable information about the geothermal system (Árnason et al., 2010; Cumming and Mackie, 2010).

5.3 Instruments and field setup

MT method

Instruments needed for a MT sounding are a data logger, 2 pairs of electric dipoles and 3 magnetic sensors. The data logger controls the acquisition process, amplifies and filters the data and converts to digital format for storage. Commonly the data logger has 5 channels, 2 for the orthogonal horizontal electrical fields (E_x, E_y) and 3 for the orthogonal horizontal and vertical magnetic fields (H_x, H_y, H_z).

A electrical field is measured as $E_i = U/D_i$ where U is the voltage and D_i is the distance between a pair of electrodes in the direction of $i = x, y$. The dipole distance is commonly in the range of 50 to 100 m. The use of non-polarisable electrodes is preferred. These consist of a plastic pot with a porous bottom filled with a metal in contact with a solution of a metallic salt of the same kind. A common metal combination is to use lead (Pb) and a solution of lead-chloride ($PbCl_2$) in the electrodes. The magnetic fields are measured with a magnetic field sensor oriented in the x, y, z directions. For the frequency range of $1000 - 0.001 Hz$, induction coil sensors are used.

When setting up a MT sounding in the field, a spirit level and a compass are used to align all the measurement axes such that the x, y directions are horizontal and orthogonal to each other and the z is vertical. Conventional alignment is x positive to magnetic North, y positive to the magnetic East and z positive vertical down. It is important to properly keep a field journal, where the exact orientation of the field setup, length of the dipoles and other valuable information is recorded.

The MT data collected in the field, needs to be processed. The raw time series of the electric and magnetic fields have to be converted from the time domain to the frequency domain and further processed as described in Section 2.2.7.

TEM method

Instruments needed for a TEM sounding are a current transmitter, wire for the transmitter loop, generator, receiver and coil. Conventional setup of TEM soundings in geothermal exploration uses a 300 by 300 m transmitter loop where a current of the order of 15A is used to generate the time varying signal. The transmitter and the receiver need to be synchronized in time, in order for the times of the measurements to be aligned with the turn off in the current.

When setting up a TEM sounding in the field, the transmitter loop is laid out in a shape as close to a square of 300 m sides. For a central-loop measurement the receiver is located in the center of the transmitter loop. Data is collected repeatedly to ensure data quality and for statistical analysis of the measurements.

6 Synthetic geothermal model

In the following chapter, the inversion of data from a synthetic geothermal system is discussed. Two different surface resistivities are considered, a homogeneous and Gaussian distributed resistivity. The design of the model, the generation of the synthetic data and noise assignment are covered first. Followed by results of the joint 1D inversion of TEM and MT data and 3D inversion of data, where a correction of static shift has both been and not been applied prior to the inversion. Lastly, a discussion of the results is given.

6.1 Model design

In order to get a better comparison of different interpretation methods used in geothermal exploration, a synthetic resistivity model of a geothermal system was designed. As discussed in Section 5.1 the typical resistivity structure of geothermal systems are described as a low resistivity coat underlain by a resistive core. The synthetic model used in this project is designed as an anomaly in a layered resistivity structure, where regional thickness and resistivity of the layers is shown in Table 6.1.

Table 6.1: The elevation to the top, bottom and the resistivity for the layers used in the design of synthetic geothermal system.

	Top [m]	Bottom [m]	Resistivity [Ω m]
Layer1	200	-290	500
Layer2	-290	-1100	10
Layer3	-1100	-3500	50
Layer4	-3500	-7600	5
Layer5	-7600	-110000	50

The layers described in Table 6.1 are similar to a layered initial model used in Árnason et al. (2010). Layer 1 is the unaltered surface rocks, commonly resistive

6 Synthetic geothermal model

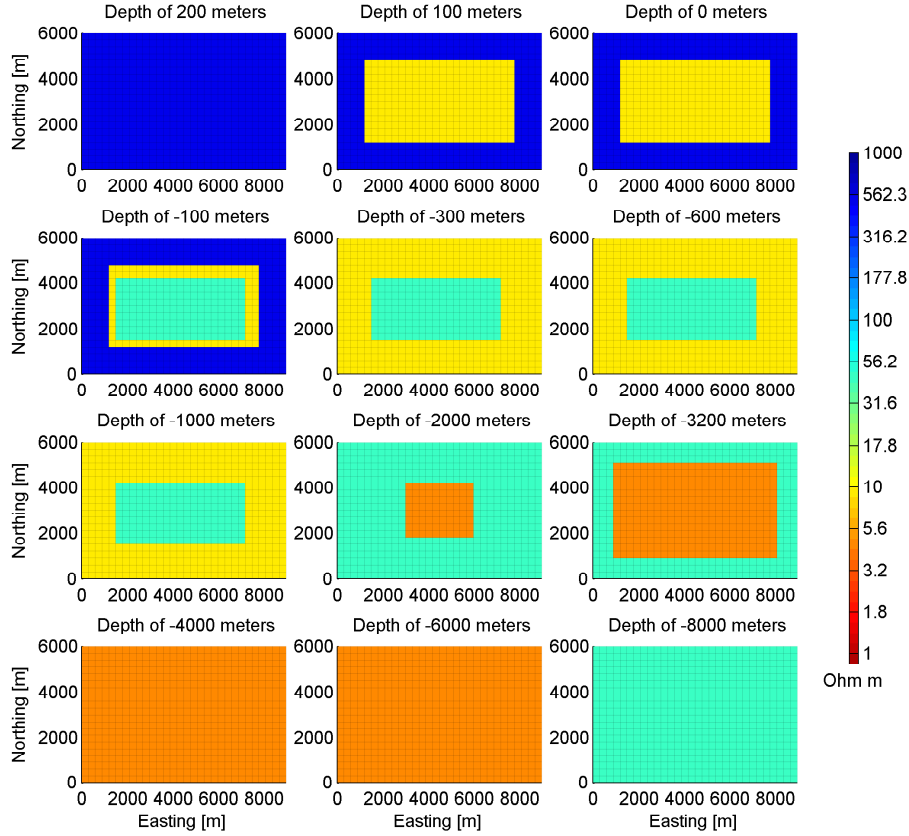


Figure 6.1: Iso-elevation maps of the synthetic geothermal model, used for forward calculation of synthetic TEM and MT data. The low resistivity coat from the 2nd layer extends from 1200-7800 m W-E and 1200-4800 m S-N. The resistive core from the 3rd layer extends from 1500 m-7200 m in W-E and 1500-4200 m S-N. The deep low resistivity layer dome extends from 3000-6000 m in W-E and 1800-4200 m S-N in the upper part and from 900-8100 m in W-E and 900-5100 m S-N in the lower part.

lavas with or without top soil; layer 2 is the conductive smectite-zeolite zone; layer 3 is the resistive chlorite-epidote zone; layer 4 is the deep low resistivity layer; and layer 5 is the bottom halfspace.

An area of interest has dimensions of 9000 by 6000 by 10000 m in Easting, Northing and Depth, respectively and has a flat surface of elevation of 200 m. A geothermal system is manifested as an upward trend of the 2nd and 3rd layers into the top layer, where the trends are blocks from the respective layers. The deep low resistivity layer has a block shaped upward dome underneath the geothermal system, signifying a heat source for the geothermal system. The horizontal and vertical extent of the model can be seen in Figure 6.1 and Figure 6.2, respectively.

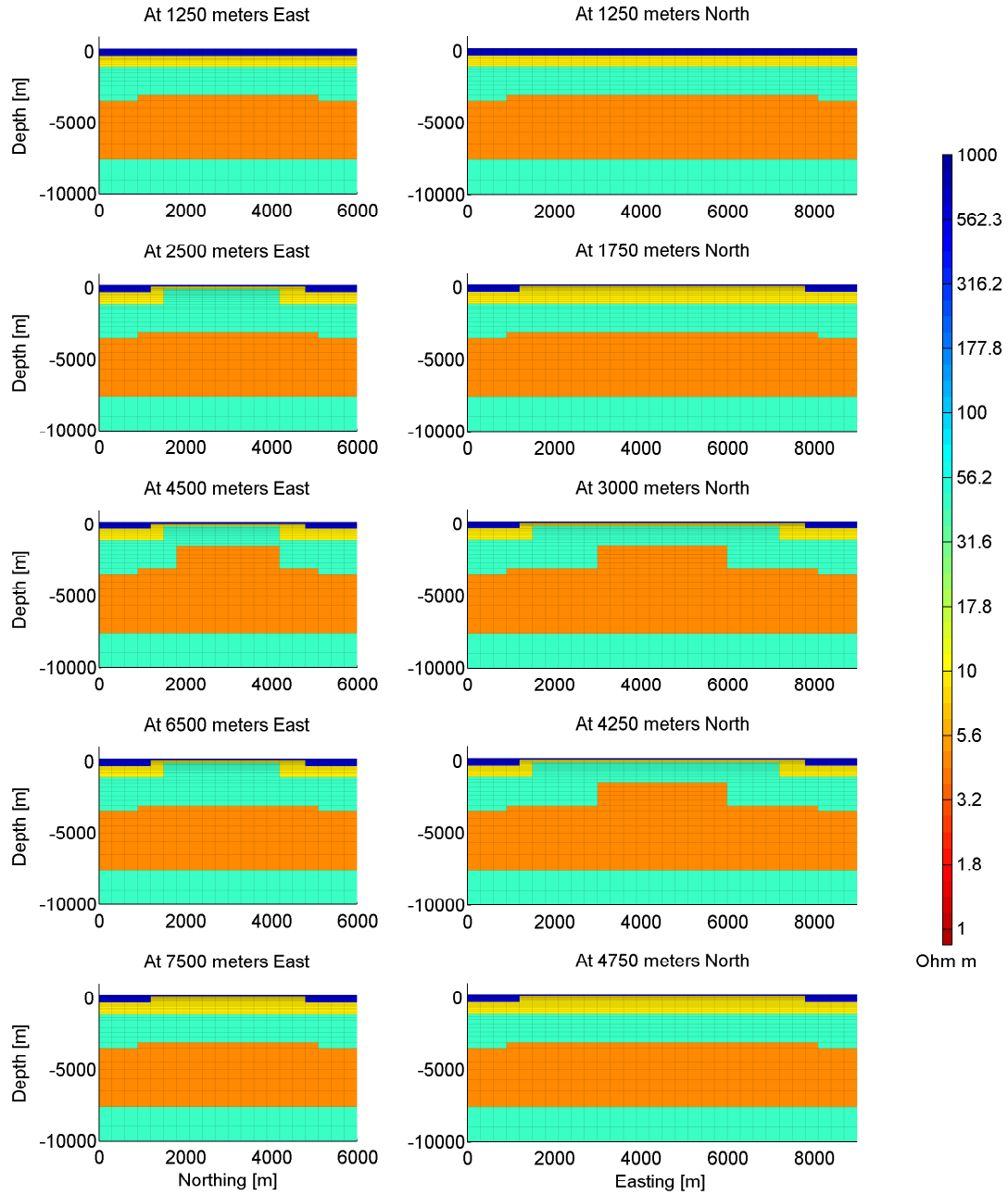


Figure 6.2: Cross sections of the synthetic geothermal model, used for forward calculation of synthetic TEM and MT data. The low resistivity coat reaches elevation of 100 m, the resistive core reaches elevation of -100 m and the upper and lower section of the deep low resistivity layer reach -1500 m and -3100 m, respectively.

Two variations of the model discussed above are used in this project. Sasaki and Meju (2006) discusses two geological processes that alter the overburden, affecting the surface resistivity structures. The processes discussed in Sasaki and Meju (2006) are categorized into (1) residual and unconformity deposits formed in situ by processes such as weathering, karstification and hydrothermal alteration, and (2) transported overburden such as granular deposits laid down by wind, water and volcanic eruptions. Both of these overburdens can be randomly distributed or cover extensive areas. Sasaki and Meju (2006) design and use models (1) small uniformly sized blocks of random resistivity and (2) an elongated body of homogeneous resistivity, different from that of the surroundings.

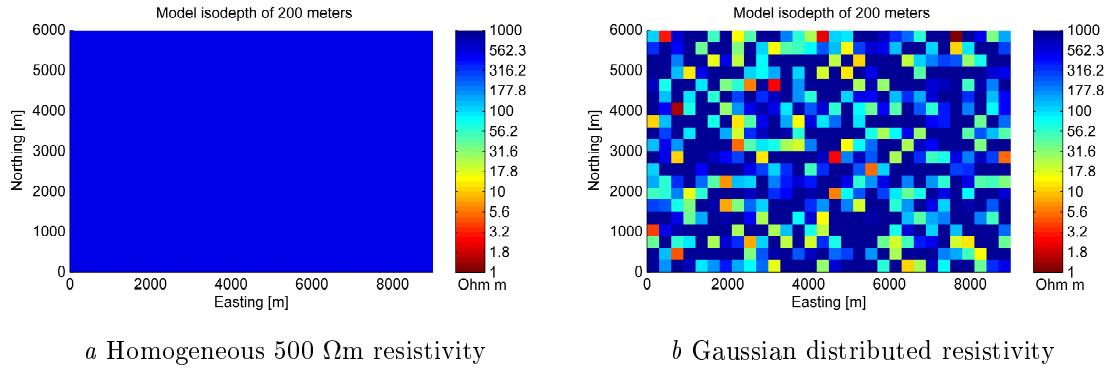


Figure 6.3: Surface resistivity of the 2 synthetic geothermal models used for calculation of the synthetic data. The model in Figure a) has homogeneous surface resistivity of 500 Ω m and the model in Figure b) has Gaussian distributed surface resistivity with a mean of 500 Ω m and standard deviation 1 on the log scale.

As discussed in Chapter 5, geothermal systems are commonly in volcanically and tectonically active areas. The overburden is often complex, constructed from volcanic erupted materials that are partly covered with soil or have been altered. Topography is as well considerable around geothermal areas, where the central volcano rises above other features. In order to introduce static shift inducing surface, a randomly varying resistivity is imposed in the surface, as in Figure 6.3b. For comparison, a model with homogeneous surface resistivity, (see Figure 6.3a), is also used.

6.2 Work procedure

To compare the effects of static shift in 3D inversions for a synthetic geothermal systems discussed in Section 6.1, the same workflow is used for both the models. The workflow includes the discretization of the geothermal systems, forward calculation of TEM and MT synthetic data, assigning noise and errors and doing 1D and 3D

inversions. Each of these steps will be discussed in the sections below.

6.2.1 Domain discretization

In order to forward model data for the synthetic geothermal area discussed above, the resistivity structure has to be discretized into mesh of cell elements. The size of the elements affects the accuracy of the solution, where small cells are more accurate but increased number of cells slows down the calculations. The penetration of the EM waves into the domain needs to be considered and boundary conditions need to be met.

Mackie (2002) discusses issues arising when discretizing domains for modeling of MT data and proposes rules of thumb in designing mesh that optimize the trade-off between accuracy and practicality of the mesh. Mackie (2002) proposes the vertical discretization as

- Thickness of surface layer to $\frac{1}{10}$ of the skin depth for the highest frequency and the least resistive cell.
- Increase the thickness of layers by a factor of 1.2 to 1.5 until the thickness is more than $\frac{1}{3}$ of the skin depth of lowest frequency and an average value of resistivity.

Horizontal discretization is further proposed as

- Within the zone of interest the column width should be of few hundred meters, but not greater, so there is roughly one sounding per column.
- Uniform spacing should be used in the zone of interest.
- Column widths can increase by a factor of 1.2 to 1.5 away from the zone of interest until the width of column is similar to the thickness of the deepest layer. Ideally the the model should be twice as thick as deep.

These guidelines were used when designing meshes used for forward calculation of TEM and MT data and for inversion of the MT data. As discussed above, the area of interest has a surface area of 54 km² and the outer edges of the geothermal systems covers approximately 23.7 km², or just over half of the area of interest. All the meshes used discretize roughly the same total volume of 163 by 163 by 163 km³. The volume includes padding cells in all directions and the air above the surface.

For the forward calculations of the TEM, cell widths of 150 by 150 m were used in the area of interest and cell thickness at the surface of 20 m. In total the mesh has

6 Synthetic geothermal model

90 by 70 by 73 cells in Easting, Northing and vertical direction where 19 top layers are the air. The mesh has a total of 459,900 cells. 15 padding cells were used on each horizontal side, expanding by a factor 1.3 to 22600 m. Within the Earth, the vertical thickness of the layers increases by a factor of 1.3 but close to the surface thickness of some adjoint layers are constant to increase resolution of the model in the near surface.

For the forward calculations of the MT, cell width in the area of interest was 300 by 300m. The same vertical thicknesses as for the TEM mesh were used. In total the mesh has 56 by 46 by 73 in Easting, Northing and vertical directions, total of 188,048 cells. On each vertical side of the area of interest 13 padding cells expending by a factor of 1.3 to 22600 m.

6.2.2 Forward modeling and error assignment

Synthetic MT data was forward modeled with MT3Dfwd, discussed in Section 4.2.3. Data was calculated for 23 frequencies in Hz

100.00	63.10	39.81	25.12	15.85
10.00	6.310	3.981	2.512	1.585
1.000	0.631	0.3981	0.2512	0.1585
0.100	0.0631	0.03981	0.02512	0.01585
0.0100	0.00631	0.003981		

A Gaussian random noise with a standard deviation of 5% of the data value and a noise floor of 10% of the mean value of each of the frequencies is added to the data. The error assigned is 10% of the data value with a floor that is 10% of the mean value of all values for each frequency.

Synthetic TEM data was forward modeled with H3DTD, discussed in Section 4.2.2. The source signal has a time-wave form assumed to be a step-off function at time 0 and data was calculated at following 20 time gates in s

8.913e-4	1.079e-3	1.323e-3	1.629e-3	2.016e-3
2.516e-3	3.154e-3	3.966e-3	5.004e-3	6.323e-3
8.004e-3	1.015e-2	1.288e-2	1.637e-2	2.082e-2
2.649e-2	3.374e-2	4.298e-2	5.476e-2	6.979e-2

The errors were assigned as a percentage of the value and a floor. The floor set as $1e-13$, the percentage for the first 15 time gates was 3% and for the last 5 as 5% of the data value.

TEM and MT data were calculated at same locations, covering most of the area of interest with equally spaced soundings with 600 m interval. Figure 6.4 shows the locations of the TEM and MT soundings relative to the outer bounds and the outer edge of geothermally altered layers.

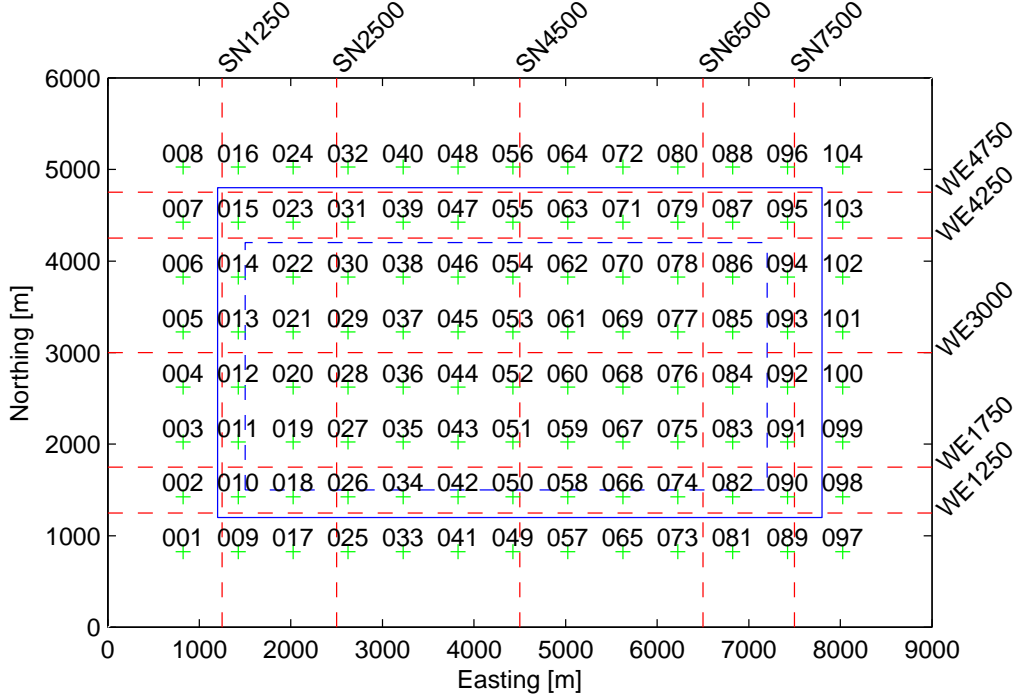


Figure 6.4: The location and names of TEM and MT soundings in the area of interest. The blue plus signs are the locations of the soundings, the numbers above are their names, blue line is the outer edge of the low resistivity coat, the dashed blue line is the outer edge of the resistive core and the red dashed lines are the placement of cross sections.

6.2.3 1D inversion

1D inversion was done with TEMTD, discussed in 4.2.1, using Occam inversion. TEM data is inverted for the measurement coil voltage and the MT data inverted for the apparent resistivity and phase. Inversions for the determinant, xy and yx elements of the MT tensor are carried out. The model has 29 layers that logarithmically increase in thickness down to 40 km depth, but a halfspace is set below that depth. A model from a 1D inversion of only the MT data was used as a starting model for the joint 1D inversions. The inversion stops if the data misfit can not be lowered, normally reaching root-mean-square data misfit around or below 1.

In order to estimate the static shift multipliers for the impedance tensor, a joint

inversion of the TEM and both the xy and yx MT impedance elements was done. The shift multiplier as estimated from the separate 1D inversion is then used to correct the impedance tensor as discussed in Section 3.3. As well, a joint inversion of TEM and the determinant of the MT impedance tensor, from Equation 2.61, was done. This practice is commonly reported as the common method when modeling MT data in 1D (e.g. Árnason et al., 2010; Cumming and Mackie, 2010; Eysteinsson et al., 2010).

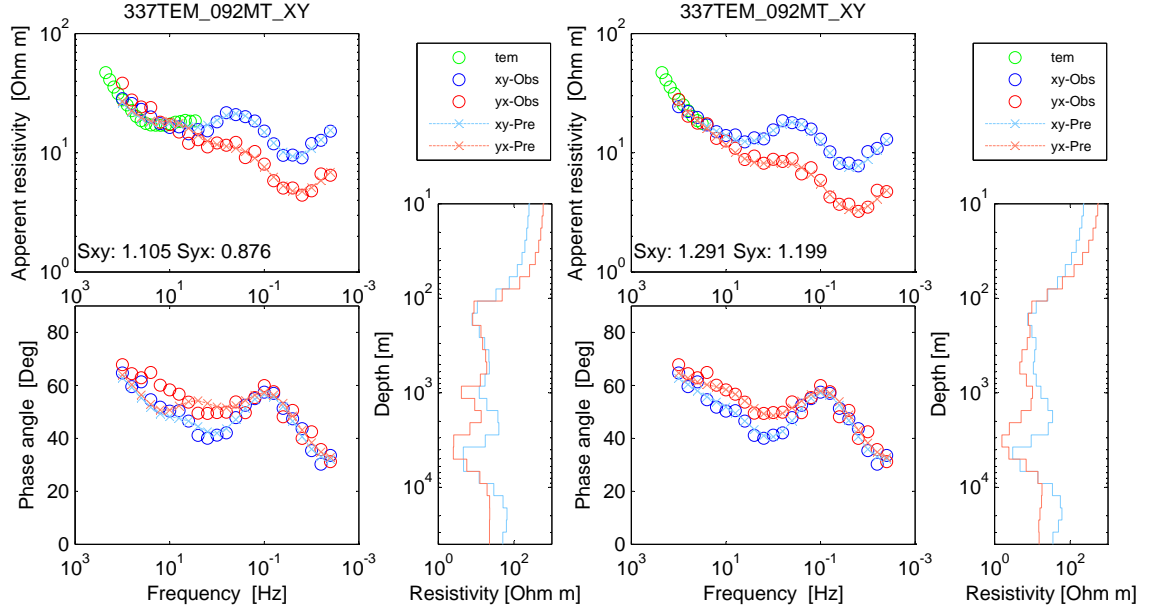


Figure 6.5: Results for joint 1D inversion of TEM and MT data for sounding 92, at the Eastern edge of the synthetic geothermal system. Apparent resistivity and phase are shown, where the green circles are the observed TEM data, blue and red circles are the observed xy and yx MT data, respectively, and the light blue and red lines and crosses are the predicted xy and yx MT data, respectively. The predicted 1D models are shown as well, with the same color coding as the predicted data. The left figure shows results where all the TEM data points are included and the right figure shows results where the last 10 data points are excluded. The fit between the TEM and MT data is better in the figure to the right, producing a better 1D models .

All the time gates of the TEM and all frequencies of the MT data are used for joint 1D inversions. However, during the joint 1D inversions the assumption that the TEM and MT soundings are sensitive to the same resistivity structure does not hold everywhere. For soundings over the vertical low resistivity coat, the match between the TEM and MT soundings is poor. The late timegates of the TEM soundings on the edge are sensitive to the 3D structure that the MT soundings are not as sensitive to. In order to get better fit of the TEM and MT data and produce

a more reasonable 1D model, the last 10 TEM data points for these measurements were excluded. Figure 6.5 shows an example of a joint 1D inversion for sounding 92, where the last 10 TEM data points have been excluded in the results shown to the right. Sounding 92 is located at the center of the Eastern edge of the geothermal system, see Figure 6.4.

The resulting models from the joint 1D inversion of the TEM and MT data are interpolated on to a 3D mesh. The area of interest has 18 by 12 cells in Easting and Northing, of cell widths of 500 by 500 m. Each side of the area of interest has 12 padding cells, that expand by a factor of 1.3 to 22600 m. The smallest thickness used was 25 m and 71 cells were used in the vertical direction, allowing for better resolution in the near surface. This adds to a total number of cells of 107,352. The resistivity of each cell in the 1D models was assigned the x, y, z, coordinate where the x and y are the Easting and Northing location of the sounding and z is the elevation of the cell center from sea level. The resistivity values of all the 1D cells were then interpolated to the centers of the cells in the 3D mesh. Forward calculations are done for the model, allowing the xy and yx modes from the 3D model constructed from the 1D inversion results to be compared to the observed xy and yx data modes.

6.2.4 3D inversion

3D inversion is done with MT3Dinv, discussed in 4.2.4. The inversion is done for the real and imaginary parts of the off diagonal elements of the impedance tensor. The initial and background models were all set as a halfspace, estimated to be the best fitting halfspace of 22 Ωm , where the halfspace value is found such that it minimizes the data misfit. During the inversion, bounds of the conductivity allowed are set in the range of 0.5 and 1000 Ωm . The relative importance of the smallness and smoothness terms of the regularization term are set as $2.5 \cdot 10^{-8}$ and 1. The algorithm determines the cooling scheme of the β trade-off parameter and updates the reference model as the resulting model from the previous β iteration. A chifactor of 0.45 is used to scale the target misfit.

Combinations of 16 frequencies are used, same as used in Árnason et al. (2010). They cover 3.5 decades of frequency

10.00	3.981	2.512	1.585
1.000	0.631	0.3981	0.2512
0.1585	0.100	0.0631	0.03981
0.02512	0.01585	0.0100	0.003981

These frequencies have a wide range of depth sensitivity and estimated skindepths, using Equation 2.46, for a 22 Ωm halfspace ranges from 750 m to 37500 m, which

covers well the expected structure depths. The mesh used for the 3D inversion of the MT data, has cell widths of 500 by 500 m in the area of interest. The horizontal extent of the mesh has 42 by 36 cells, with 12 padding cells on each side expanding to 22600 m by a factor of 1.3 for each padding cell. Vertical discretization with smallest thickness of 50 m and 48 cells, adding to total number of cells of 72,576. Given the range of skindepths, the design of the mesh falls within the mesh design criteria discussed in Section 6.2.1. Since the objective is to compare inversion results for synthetic MT data without and with static shift correction for two synthetic geothermal models, the speed of the inversions is important. The effects of the discretization and the frequency selection are investigated in more detail in Section 6.4.

6.3 Results of inversion modeling

In the following sections, results of joint 1D TEM and MT inversions and 3D MT inversions for synthetic geothermal models are discussed. The x and y directions in the following discussion refer to North and East direction in the model, respectively. The results of a joint 1D inversion TEM and the determinant of the MT data, 3D inversion where no static shift correction is done and 3D inversion where a static shift correction as discussed in Section 3.3 is applied prior to the inversion. Results for both of the synthetic geothermal models described in Section 6.1 are discussed separately.

6.3.1 Model with homogeneous surface resistivity

The results for inversion of a synthetic geothermal model with homogeneous surface resistivity, as described in Section 6.1, are discussed in the following section. The joint 1D inversions were setup as described in Section 6.2.3. All of the inversions reached a desired level of data misfit and the TEM and MT data match up well, when timegates of the TEM data were excluded from the inversion for some of the soundings as discussed in Section 6.2.3. The 3D inversions was set up as described in Section 6.2.4, where in both inversions the target misfit was 2995. A total of 20 iterations were needed to reach the target misfit for the inversion of MT data without a static shift correction. A total of 19 iterations were needed to reach the target misfit for the inversion of MT data with static shift correction.

Predicted data for inversions

Visualization of MT data is commonly done as (1) soundings, where the data is plotted for all the frequencies for each sounding, (2) pseudo-sections, where the MT data is plotted as a section of MT sounding locations on the x-axis and frequency on the y-axis or (3) iso-frequency maps of the MT data of 1 frequency is plotted as a map for all the MT soundings locations. Examples of observed and predicted data for all of the inversions are shown as iso-frequency maps.

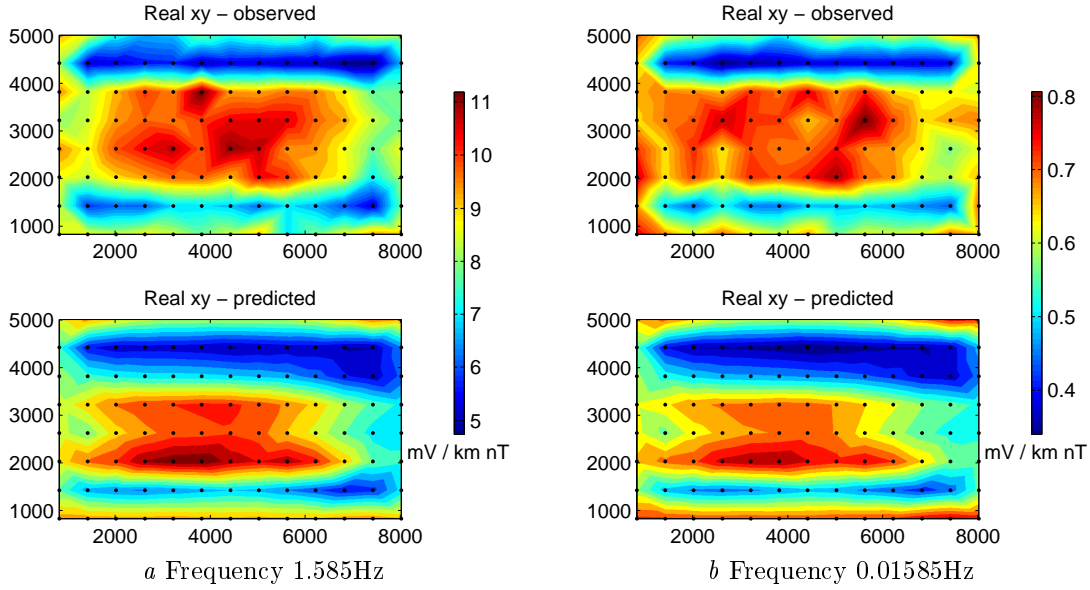


Figure 6.6: Real part of xy observed and predicted data at two frequencies, for the joint 1D inversion of the TEM and MT data. The predicted data is forward calculated from the 3D model interpolated from the resulting 1D models from joint inversions of the TEM and MT for a synthetic geothermal model with homogeneous surface resistivity. A resemblance can be seen between the observed and predicted data, but coincidence of boundaries is not good.

In Figure 6.6, two iso-frequency maps of the observed and predicted data are shown, where the predicted data is forward calculated from the 3D model interpolated from the resulting 1D models for a joint inversion of the TEM and MT data. For the higher frequency in Figure 6.6a, the predicted data resembles the observed data, but no details match. The low amplitude data anomaly, seen as the elongated West-East directed blue feature at approximate 4500m North, is present in both the observed and predicted data but the feature in the predicted data is larger and with a different shape. For the lower frequency, Figure 6.6b there is similar resemblance but edges and shapes do not match. Comparison of observed and predicted data of other elements and frequencies used in the inversion, have a similar general resemblance

with poor agreement of boundaries.

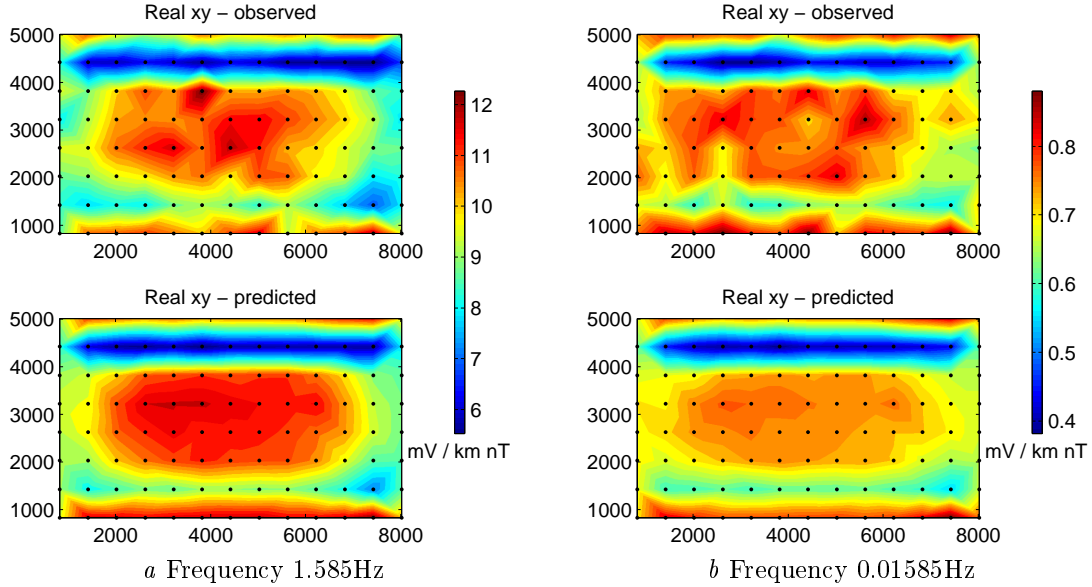


Figure 6.7: Real part of xy observed and predicted data of a 3D inversion model for a synthetic geothermal model with homogeneous surface resistivity, where no static shift correction has been applied to the data prior to the inversions. Coincidence of the observed and predicted data is good, where boundaries of features match well.

In Figure 6.7, two iso-frequency maps of observed and predicted data of 3D inversion of the MT data where no static shift correction was applied are shown. For the higher frequency in Figure 6.7a, the predicted data coincides well with observed data. Boundaries and size of the anomalies agree well, but the smaller scale features are not seen in the predicted data. This is seen in the high amplitude data anomaly in the center where boundaries coincide but the amplitude and finer details are not recovered in the predicted data. For the lower frequency in Figure 6.7b, the comparison of the predicted to the observed data, reveal similar match as in Figure 6.7a. Comparing predicted and observed data for other elements used in the inversion, reveals similar results.

In Figure 6.8, two iso-frequency maps of the observed and predicted data of 3D inversion of MT data where a static shift correction was applied are shown. As for the inversion of the data without static shift correction in Figure 6.7, the observed and predicted data agree well. For the higher frequency in Figure 6.8, the predicted and the observed data agree well. The boundaries and size of the anomalies coincide but as before the small scale features are not recovered well. For the lower frequency, the boundaries in the South-North direction are well defined but in the West-East direction the boundaries can not be seen. Similar results are seen when predicted

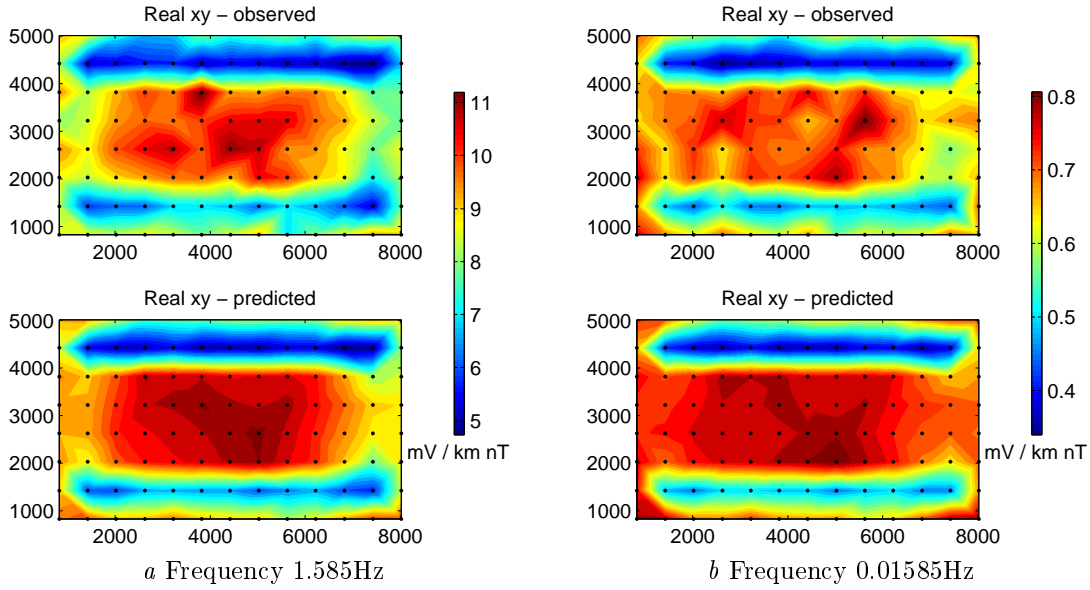


Figure 6.8: Real part of xy observed and predicted data of a 3D inversion model for a synthetic geothermal model with homogeneous surface resistivity, where a static shift correction has been applied to the data prior to the inversions. Coincidence of the observed and predicted data is good, where boundaries of structures match well.

and observed data for the other elements and frequencies are compared.

When the observed data without a static shift correction, Figure 6.7, and observed data with a static shift correction, Figure 6.8, are compared it can be seen that the low anomaly data features on the North and South edges are larger for the static shift corrected data. In both cases, the predicted data captures these differences.

Static shift estimation

Maps of the static shift multipliers can be seen in Figure 6.9. The multipliers are estimated from a joint 1D TEM and MT inversion for each of the xy and yx modes of the MT tensor. The largest shifts are seen on the edge of the geothermal system that is perpendicular to the direction of the electric field in the impedance tensor. For both of the components, moderate static shift is seen over the geothermal area. These estimates of the static shift are used for correction of the impedance tensor, as discussed in 3.3.

The static shift multipliers seen in Figure 6.9 are induced by the geothermal system

6 Synthetic geothermal model

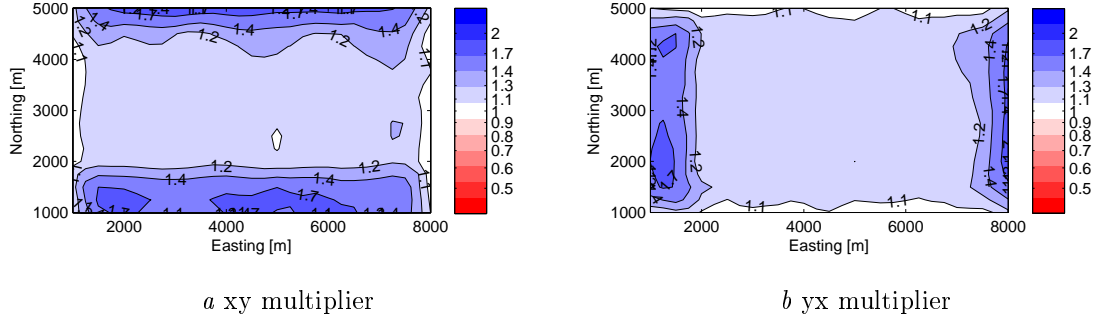


Figure 6.9: Maps of xy and yx static shift multipliers for synthetic geothermal system with homogeneous surface resistivity. The multipliers i are estimated from individual 1D joint inversion of TEM and MT data for the xy and yx modes, respectively. The multipliers are clear at the edges of the geothermal system, perpendicular to the electric field.

itself. Even though there are no inhomogeneities in the near surface, static shift is detectable.

Comparison of inversion results

Figures 6.10, 6.11 and 6.12 show synthetic geothermal model with homogeneous surface resistivity being compared to resulting inversion models.

Figure 6.10 shows iso-elevation maps at 200 m (the surface), -300 m and -3200 m. At the surface of the model, all the recovered models have a lower resistivity in the center of the area of interest surrounded by higher resistivity. In the models from the 3D inversions (rows c and d in Figure 6.10) the surrounding resistivity is of the order of 100 Ωm and has approximate resistivity at the center of 15 Ωm compared to 500 Ωm surface resistivity in the original model (row a in Figure 6.10). The 1D inversion model (row b in Figure 6.10) does better in recovering the surrounding resistivity of the original model (row a in Figure 6.10) but has a similar lower resistivity in the center. At -300m, the 1D model has a good recovery where a resistivity core of approximate 50 Ωm is seen in 10 Ωm layer. The 3D model with no static shift correction, does recover a resistive core surrounded by a low resistivity coat of 2 to 8 Ωm that is then surrounded by higher resistivity, where the layer of low resistivity is not recovered. The 3D model where a static shift correction has been applied, recovers better the resistive core embedded in a layer, but the layer is nonuniform with resistivity in the approximate range of 1 to 15 Ωm . At -3200 m, the 1D recovered model does not contain much indication of the doming of the deep low resistivity layer. Both the 3D models contain low resistivity structures that coincide with the doming of the deep low resistivity layer, but the shape or size are not

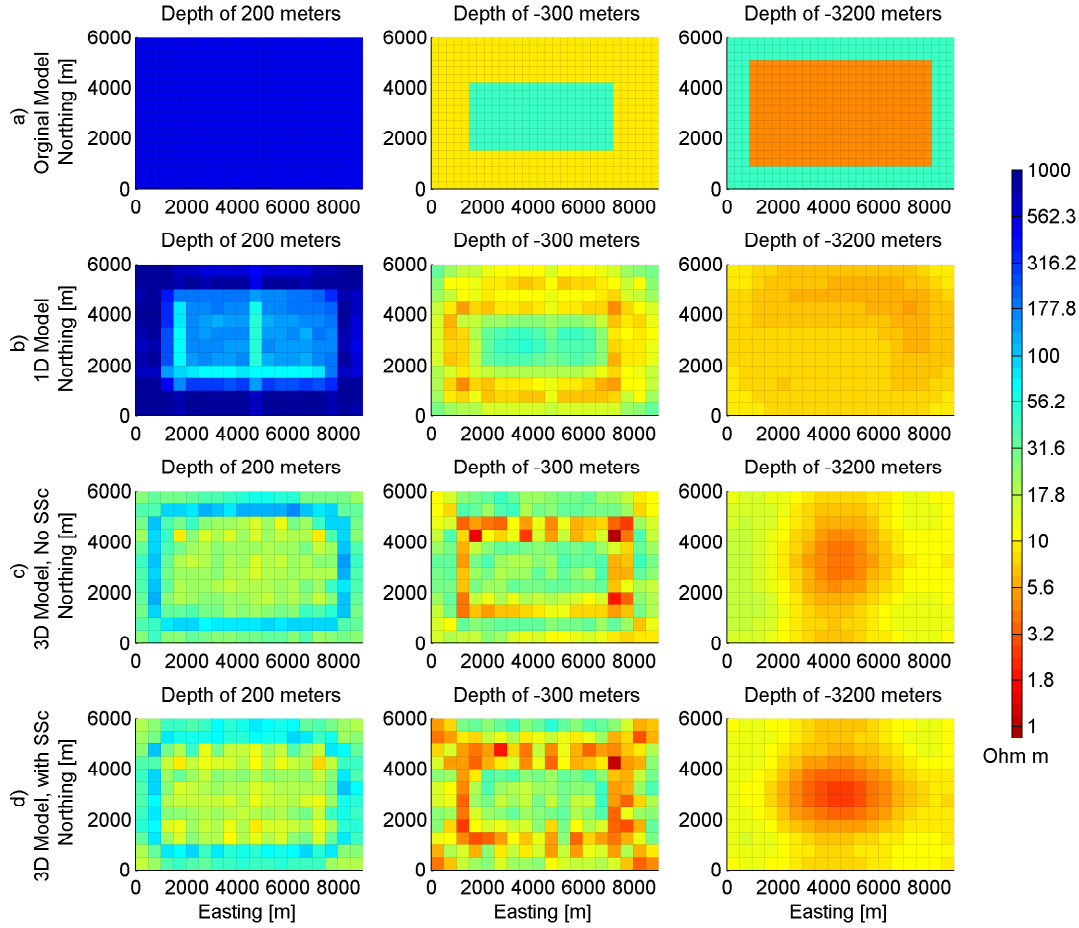


Figure 6.10: Iso-elevation maps comparing the synthetic geothermal system with homogeneous surface resistivity and the resulting inversion models. Row a) is the original model, row b) is the result from a joint 1D TEM/MT inversion, row c) is the result from 3D inversion of MT data without static shift correction and row d) is the result from a 3D inversion of MT data with static shift correction.

completely recovered.

Figures 6.11 and 6.12, show cross sections in the West-East and South-North directions, respectively. Comparing the recovered models with the original model in cross sections shows that the surface structures of the recovered models coincide reasonably with the surface structures of the original model. The thin 500 Ωm surface resistivity over the geothermal system is not fully recovered in any of the models, but the 1D comes closest to recovering the surface resistivity of the original model. However in the depth range of -1500 to -4000m, where the doming of the low resistivity layer occurs, the model from the joint 1D inversion does not recover any structure. Underneath the edges of the geothermal system, there are resistivity anomalies at depth of approximately -3500m but those anomalies are artifacts that

6 Synthetic geothermal model

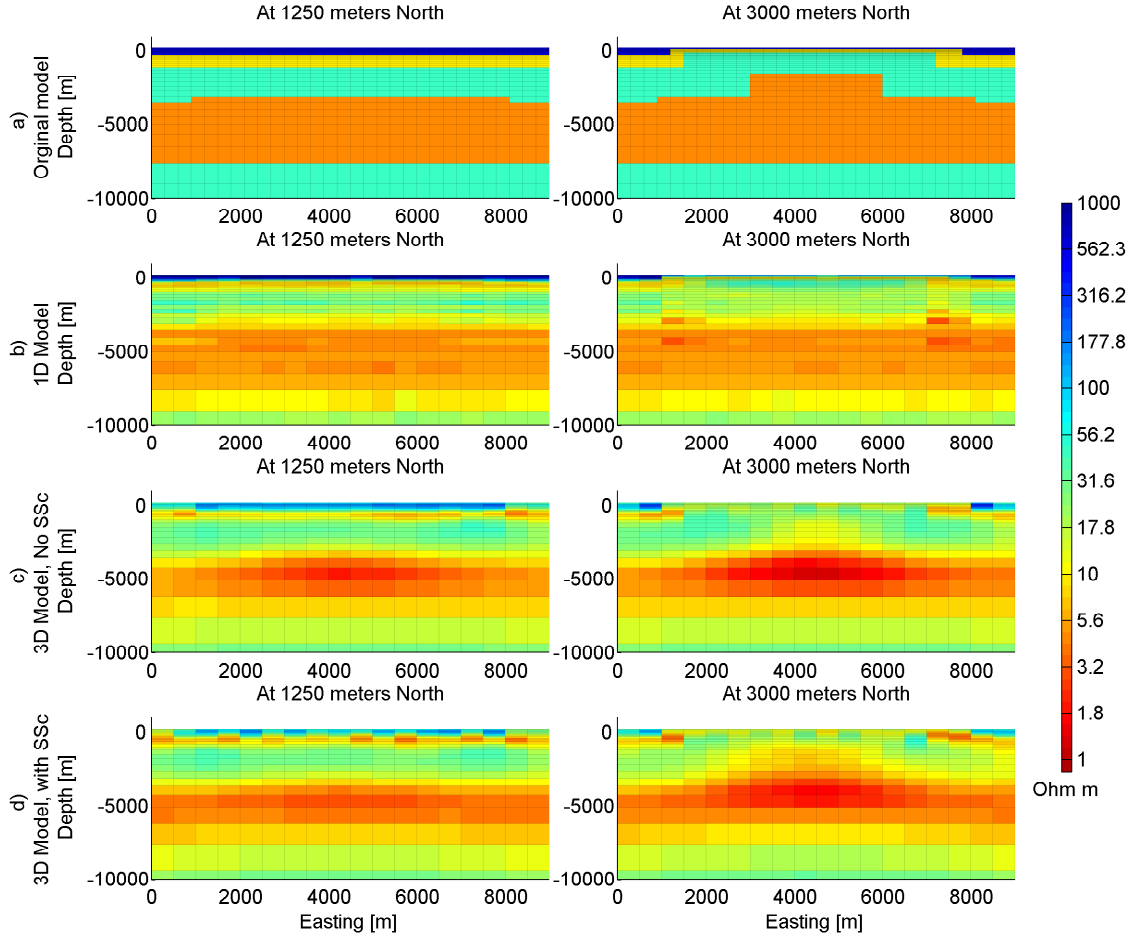


Figure 6.11: Cross sections in West-East direction comparing the synthetic geothermal system with homogeneous surface resistivity and the resulting inversion models. Row a) shows the original model, row b) shows the result from a joint 1D TEM/MT inversion, row c) shows the result from 3D inversion of MT data without static shift correction and row d) shows the result from a 3D inversion of MT data with static shift correction.

do not correspond to any structure in the original model. The 3D models do recover the doming, predicting the actual shape of structure fairly accurately but the resistivity values of the dome are 5 to 10 Ωm . The 3D inversions recover the thickness of the deep resistivity layer somewhat better compared to the joint 1D inversion, but the estimated resistivity values in the 3D models are in the range of 1.5 to 4 Ωm compared to resistivity of 5 Ωm in the original model and the 1D model.

Comparing the recovered models from 3D inversion of MT data without and with static shift correction, some differences at the edges of the geothermal system and of doming of the deep low resistivity layer are noticeable. The differences are not

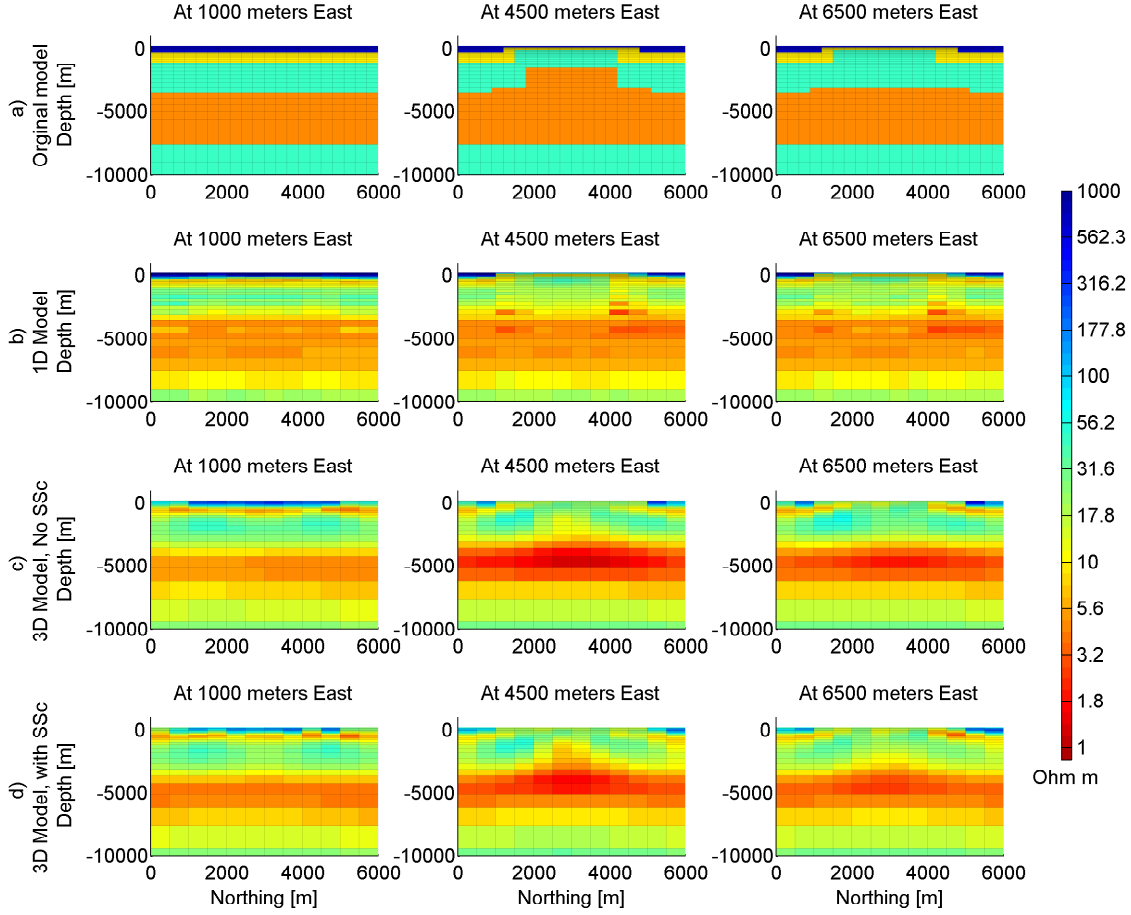


Figure 6.12: Cross sections in South-North direction comparing the synthetic geothermal system with homogeneous surface resistivity and the resulting inversion models. Row a) shows the original model, row b) shows the result from a joint 1D TEM/MT inversion, row c) shows the result from 3D inversion of MT data without static shift correction and row d) shows the result from a 3D inversion of MT data with static shift correction.

critical and all the general structures coincide in both the recovered models. The induced static shifts are due to the close proximity of the geothermal system to the surface and have a low amplitude. The differences in the recovered models can be explained by the static shift corrections, but it also needs to be kept in mind that the inversion is an under-determined problem, where multiple models can explain the same data.

6.3.2 Gaussian distributed surface resistivity

The results for inversion of a synthetic geothermal model with Gaussian distributed surface resistivity, as described in Section 6.1, are discussed in the following section. The joint 1D inversions were setup as described in Section 6.2.3. All the individual 1D inversions reached a desired level of data misfit where the TEM and MT data match smoothly. For some of the inversions, TEM timegates were excluded from the inversion, as discussed in Section 6.2.3. The 3D inversions was set up as described in Section 6.2.4. The target misfit was 2995 for both of the inversions. For both of the inversions a total of 20 iterations were needed to reach the target misfit.

Predicted data from inversions

The observed and predicted data from are visualized as iso-frequency maps below.

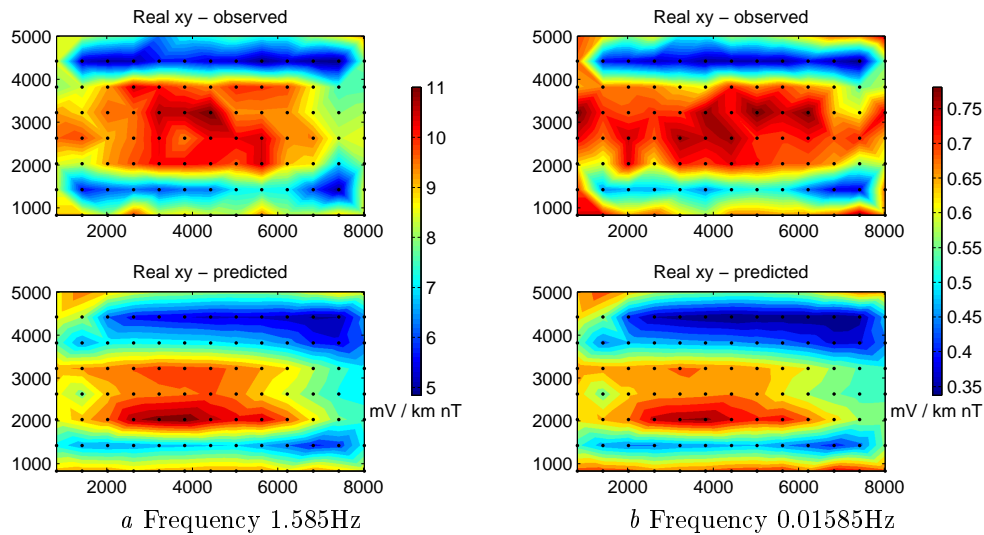


Figure 6.13: Real part of xy observed and predicted data at two frequencies, for joint 1D inversion the TEM and MT data. The observed data is the static shift corrected MT data and the predicted data is forward calculated data from the 3D model interpolated from the 1D models for a joint inversion TEM and MT for a synthetic geothermal model with Gaussian distributed surface resistivity. Some similarity can be seen between the observed and predicted data, but coincidence of boundaries and features is not good.

In Figure 6.13, two iso-frequency maps of the observed and predicted data. The predicted data, forward calculated from the 3D model constructed from 1D models from joint inversion of TEM and MT data. There is a good resemblance between

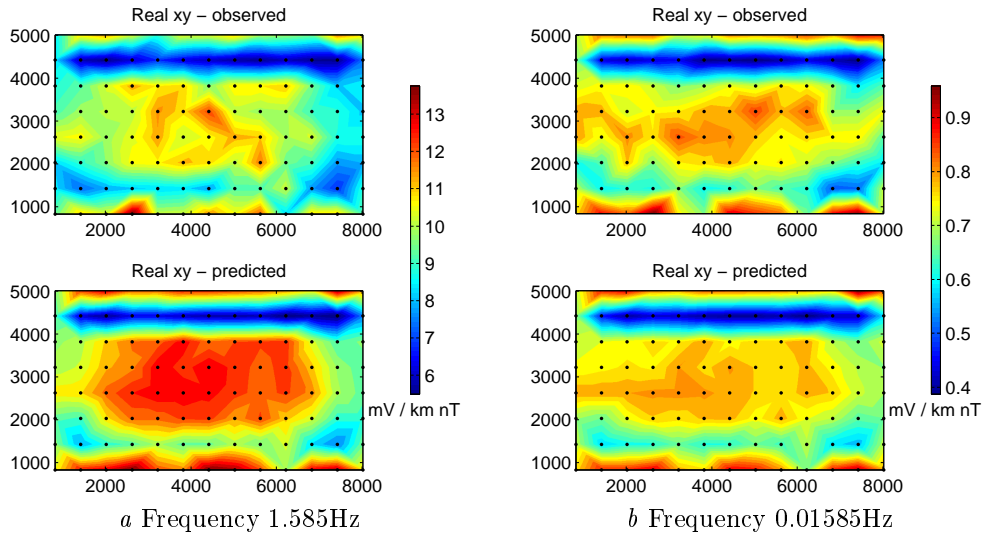


Figure 6.14: Real part of xy observed and predicted data of a 3D inversion model for a synthetic geothermal model with Gaussian distributed surface resistivity, where no static shift correction has been applied to the data prior to the inversions. The predicted data in a) overestimates the observed data but in b) the resemblance is better.

the predicted data in Figures 6.6 and 6.13 where the size and details of the predicted and observed data do not agree well.

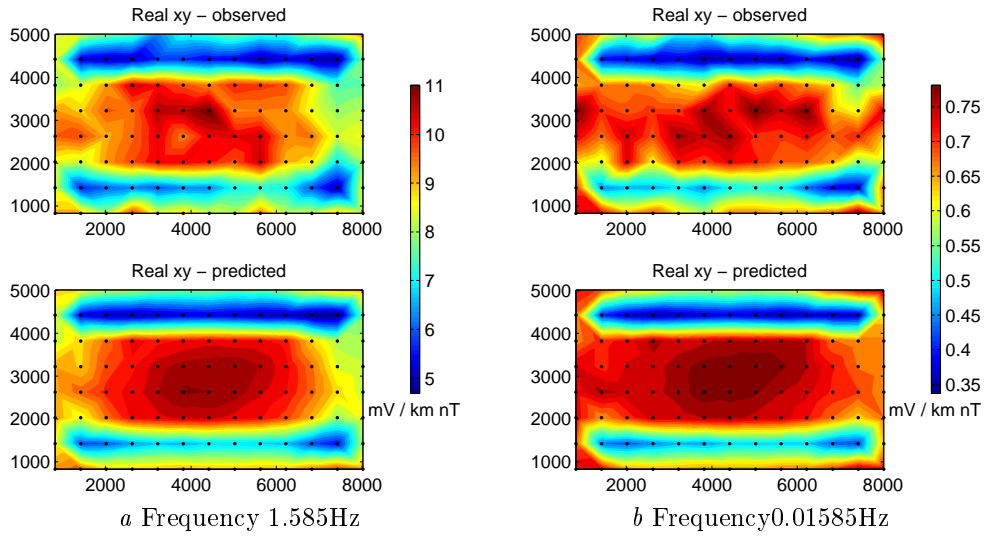


Figure 6.15: Real part of xy observed and predicted data of a 3D inversion model for a synthetic geothermal model with Gaussian distributed surface resistivity, where a static shift correction has been applied to the data prior to the inversions.

In Figure 6.14, two iso-frequency maps of the observed and predicted from 3D inversion of MT without static shift correction. The variance of the data is considerable greater in Figure 6.14 compared to Figure 6.7 and the predicted data has as well more variance, recovering the some of the effects of the static shift. However, Figure 6.15 shows two iso-frequency maps of the observed and predicted data with a static shift correction. When the observed data in Figure 6.15 is compared to Figure 6.7, the resemblance is clear. Since in both cases a static shift correction has been applied to the data, the effect of the static shift has been filtered out. There are still some minor differences in the data, that are due to the random noise assigned to each of the data. Therefore, it is not surprising that the predicted data in Figures 6.15 and 6.7 coincide well.

Static shift estimation

The static shift multipliers that are estimated from a joint 1D TEM and MT inversion for each of the xy and yx modes of the MT tensor, are shown in Figure 6.16. The appearance of the xy and yx static shift multipliers for an inhomogeneous surface resistivity, shown in Figure 6.16, is similar to the xy and yx static shift multipliers for a homogeneous surface resistivity in Figure 6.9. The clear difference are the irregularities seen in Figure 6.16, due to the inhomogeneous surface resistivity.

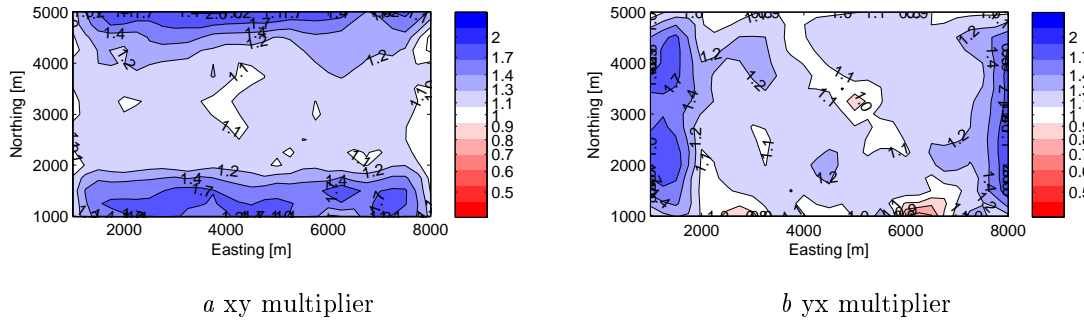


Figure 6.16: Maps of xy and yx static shift multipliers for synthetic geothermal system with Gaussian distributed surface resistivity. The static shift multipliers are estimated from individual 1D joint inversion of TEM and MT data for the xy and yx modes, respectively.

Comparison of inversion results

Figures 6.17, 6.18 and 6.19 shows a synthetic geothermal model with Gaussian distributed surface resistivity being compared to resulting inversion models.

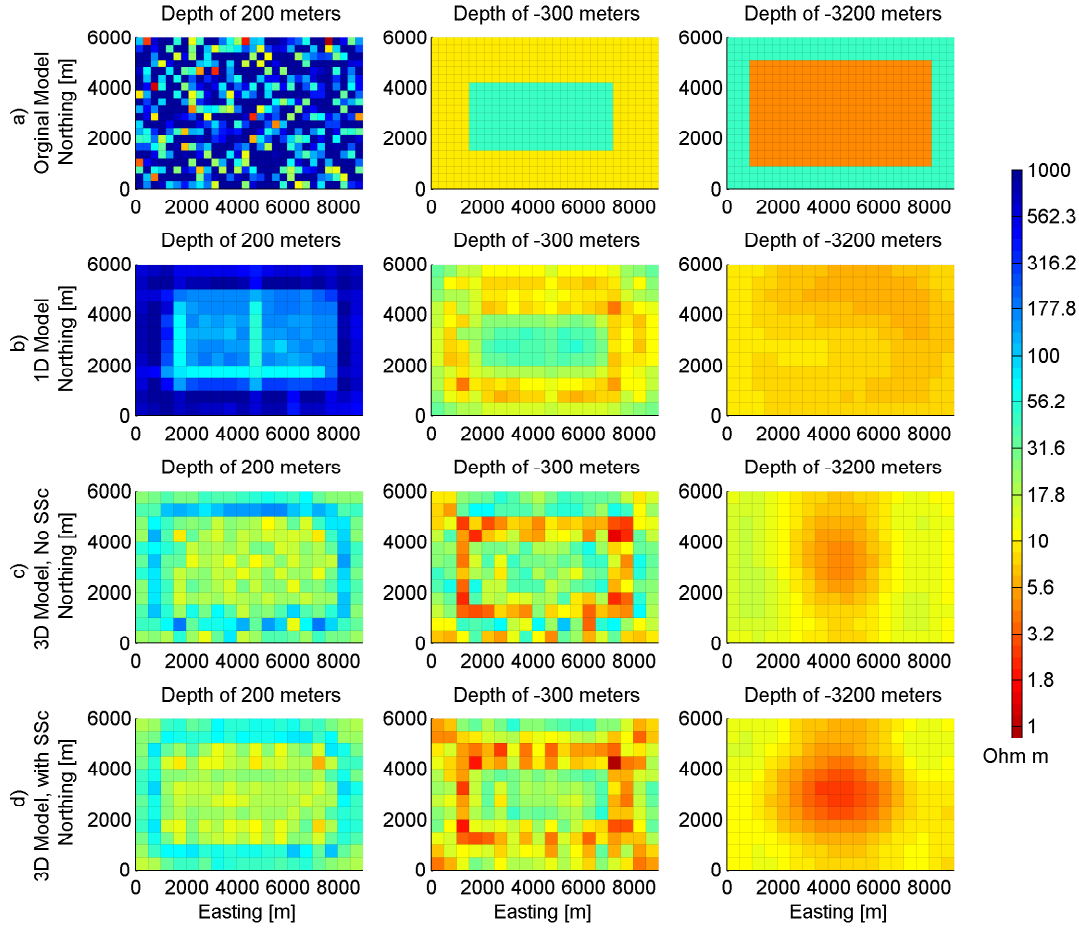


Figure 6.17: Iso-elevation maps comparing the synthetic geothermal system with Gaussian distributed surface resistivity and the resulting inversion models. Row a) is the original model, row b) is the result from a joint 1D TEM/MT inversion, row c) is the result from 3D inversion of MT data without static shift correction and row d) is the result from a 3D inversion of MT data with static shift correction.

Figure 6.17 shows iso-elevation maps at 200 m (the surface), -300 m and -3200 m. The surface of the original model is highly discontinuous and none of the inversions are able to recover this resistivity. All the recovered models have lower resistivity in the center of the area of interest surrounded by higher resistivity, similar to that as seen in Figure 6.10 for the model with homogeneous surface. The 1D inversion model (row b in Figure 6.17) is very similar to the recovered model discussed in Section 6.3.1, the shallow resistivity structures are recovered quite accurately but at depth it fails to recover the structure. The 3D inversion models (rows c and d in Figure 6.17) recover similar models as for the inversion of the geothermal model with homogeneous surface (in Figure 6.10). Close to the surface the recovery of the resistivity structures is reasonable with all major boundaries recovered but at depth the accuracy is better. A noticeable difference is seen in the 3D models of

6 Synthetic geothermal model

data without static shift correction (row c in Figures 6.10 and 6.17), where the 3D model for the inversion of data from the geothermal model with the inhomogeneous surface resistivity has more variations in the near surface. This is especially seen in the Southern part of the area of interest.

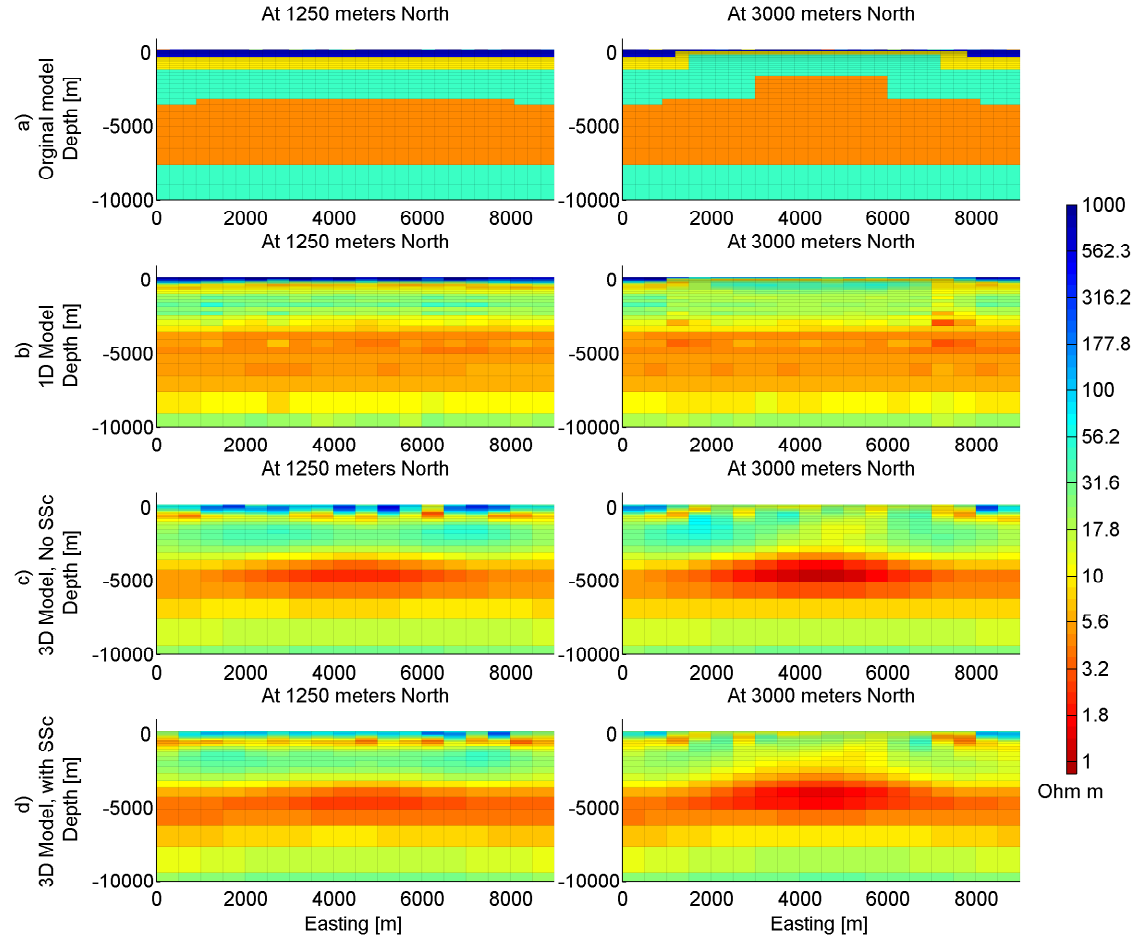


Figure 6.18: Cross sections comparing the synthetic geothermal system with Gaussian distributed surface resistivity and the resulting inversion models. Row a) is the original model, row b) is the result from a joint 1D TEM/MT inversion, row c) is the result from 3D inversion of MT data without static shift correction and row d) is the result from a 3D inversion of MT data with static shift correction.

Figures 6.18 and 6.19 show cross sections in the West-East and South-North directions, respectively. Comparing the recovered models with the original model in cross sections shows that the surface structures of the recovered models coincide reasonable with the surface structures of the original model. The thin inhomogeneous surface layer is not resolved nor is the 100m thick layer of 500 Ωm that the geothermal system is embedded in. In range of -1500 to -4000 m, the joint 1D inversion model does not see the doming of the deep low resistivity layer. Both of the 3D

models recover doming structures at depth, but the boundaries and edges vary.

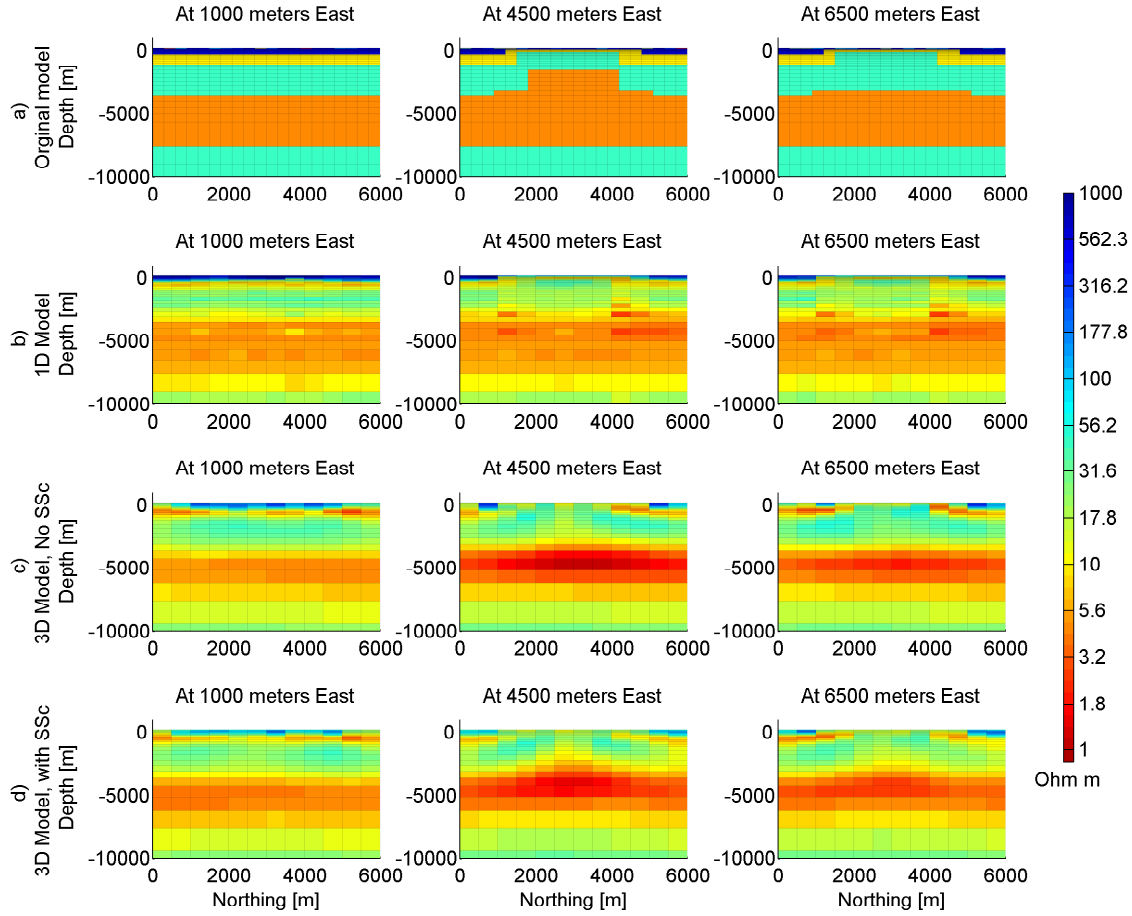


Figure 6.19: Cross sections comparing the synthetic geothermal system with Gaussian distributed surface resistivity and the resulting inversion models. Row a) is the original model, row b) is the result from a joint 1D TEM/MT inversion, row c) is the result from 3D inversion of MT data without static shift correction and row d) is the result from a 3D inversion of MT data with static shift correction.

It is expected that the inversion of the static shift corrected data will yield similar recoveries, since in both cases the observed data are consistent with one another. If the static shift correction is truly correct, only the random noise in the data would cause variations. The recovered models of 3D inversion of the static shift corrected data, agree well with each other. At -300 m, a similar irregular low resistivity layer surrounding a more resistive core is seen for both the models in the bottom rows of Figure 6.10 and 6.17. Similarly when the cross sections are compared, the row d) in Figures 6.11 to 6.18 and 6.12 to 6.19, shows that the doming of the deep low resistivity layer is recovered very similarly in both the models.

6.4 Investigation of the inversion

In this section the design of the mesh used for the inversion and the selection of frequency will be investigated further. For the inversions in Section 6.3, the mesh was designed such that the inversion runs relatively quickly but at the cost of the resolution in the mesh. The frequencies used give a good range of skindepths over the expected structures. To illustrate differences of inversion results using different meshes and/or frequencies, inversions for synthetic MT data from the geothermal system with homogeneous surface are compared and discussed.

6.4.1 Domain discretization

The discretization of the domain affects the results the inversion. Since the forward problem is solved during each iteration of an inversion, the total number of cells influences the speed of the inversion. The forward solution becomes more accurate when finer cells are used to discretize the domain, but the increased total number of cells in the system demands more time and computer resources to calculate the forward solution. Using finer mesh in the inversions increases the resolution of the mesh but the higher degree of freedom may cause different shape of structures.

Table 6.2: Relationship of mesh size and computation time. The smallest cell, total number of cells in the inversion and the computational time are listed for all the meshes used for the inversion of the models in Figure 6.20.

	Smallest cell [m*m*m]	Total nr of cells	Total nr iterations	Computation time [hh:mm:ss]
Inversion mesh	500*500*50	72576	20	9:12:42
Refined vertical	500*500*25	107352	18	13:53:44
Refined horizontal	300*300*50	114048	23	22:10:14
Forward mesh	300*300*20	188048	18	34:54:08

Figure 6.20 shows inversion models for MT data from the synthetic geothermal system with homogeneous surface resistivity where different meshes are used, see table 6.2. It is clear that the discretization influences the resulting inversion model. All the models recover similar layered resistivity structure and the structures recovered in the near surface agree fairly well. The doming of the deep low resistivity layer is recovered differently. The model shown in row b) is the results of the inversion where the mesh described in Section 6.2.1 was used. The doming is seen but is not well defined. When this model is compared to a model from inversion where a vertically refined mesh is used (row c), the doming of the deep low resistivity layer becomes

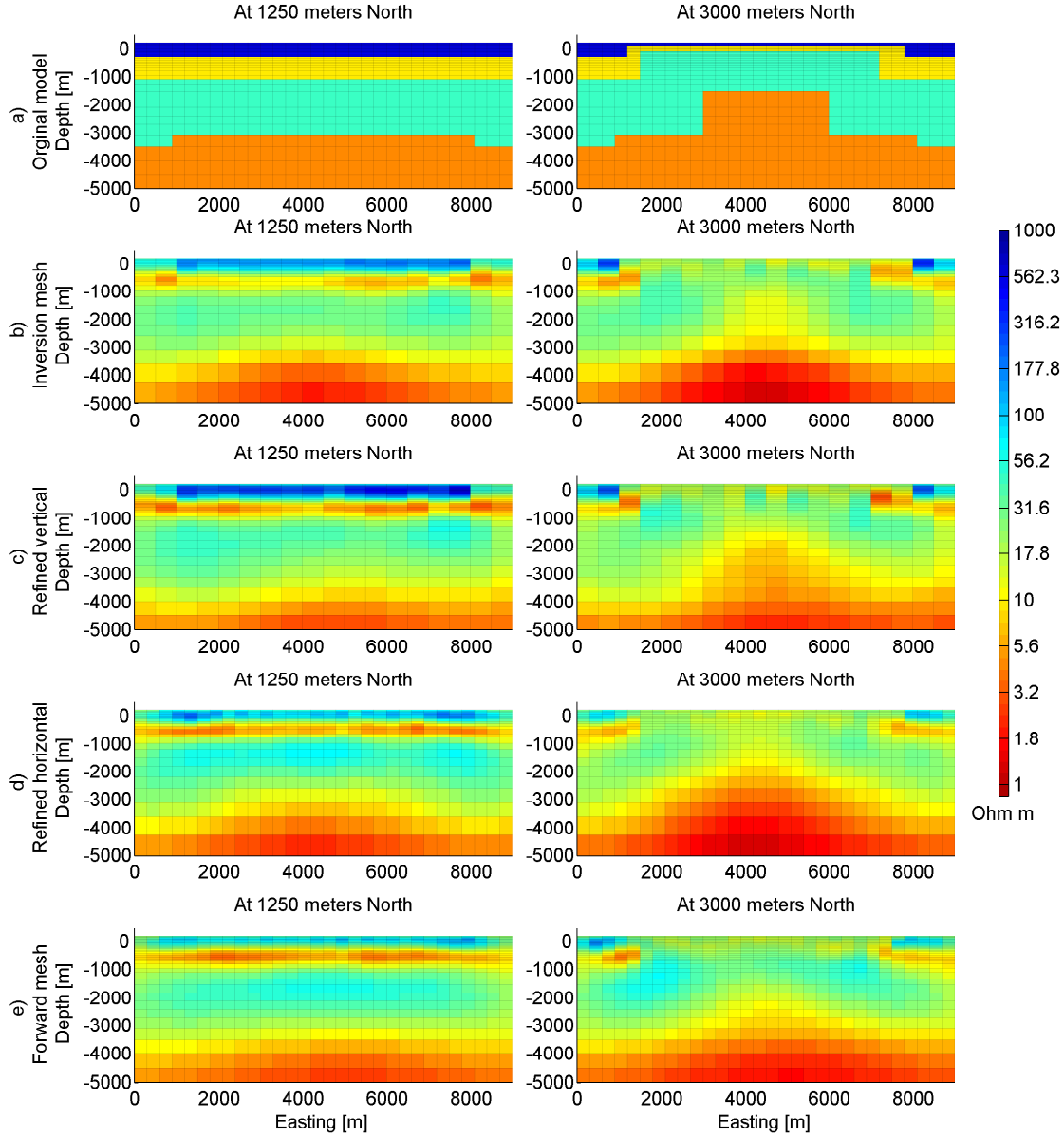


Figure 6.20: Cross sections comparing the synthetic geothermal system with homogeneous surface resistivity to 3D inversion of MT data without static shift correction, using different meshes. The model in row a) is the original model, b) is the inversion shown in Section 6.3.1, c) uses the fine mesh discussed in Section 6.2.1, d) uses mesh with horizontal cells of 300 by 300m in the area of interest but same vertical cell sizes as the inversion model and e) uses the mesh used for the forward calculations of the MT data.

clearer. Both the amplitude and the shape of the doming match the original model closer. In row d) a mesh that has the horizontal cells refined, such that the area of interest is discretized with 300 by 300 m cells, the doming smooths out to the sides and the estimated resistivity in the dome increases. In row e), the mesh in the one

used in the forward modeling of the MT data. The doming can be seen but does not reach as close to the surface as in other models in Figure 6.20.

The increased resolution comes with extra computational costs. All the inversions were run with the same computer configuration. The calculations were distributed onto 8 Intel®Xeon®X5660 CPU's with 2.80 GHz clock speed. Table 6.2 lists the smallest cell size, the total number of cells for the meshes used in the inversion for the models in Figure 6.20 and the time it took to achieve the target misfit. It is clear that with increased number of cells the time it takes to achieve the target misfit increases. The models in Figure 6.20 recover the same general structure validating the existence of the structure but the shape and boundaries of the structures vary.

6.4.2 Frequency selection

The frequencies in an inversion influence the depths of structures that can be recovered, where higher frequencies resolve shallower structures. The skindepth of EM waves (Equation 2.46), dictates the penetration of the waves into the earth. The skindepth depends on the frequency and resistivity of the earth that the wave is penetrating. The target depth and expected resistivity in the area need to be considered when selecting frequencies to use in an inversion. The frequency selection discussed in Section 6.2.4, has a large frequency range allowing recovery over a great depth range. The highest frequency selected was only 10 Hz and that limits the potential to recover variations in the near surface. The skindepths for all the frequencies used, for a 22 Ωm homogeneous resistivity (Table 6.3), reveal that the smallest skindepth is of the order of 750 m. Using this as an indicator of depth of investigation it can be seen the data resolution is not good close to the surface. In order to see the effects of different frequency selection, inversions of MT data for the synthetic geothermal system with the homogeneous surface resistivity were done for the frequencies in the first column of Table 6.3.

The new frequencies are 16 as before and cover almost 4 decades with 4 frequencies per decade. The frequencies range from 63.10 Hz to 0.01 Hz. These frequencies span approximate skindepths from 300 m to 23600 m, increasing the resolution in the near surface but covering the depth of the target structure well.

In Figure 6.21, two West-East directed cross sections of models from inversion of data with the new and the original frequency ranges are compared to the synthetic geothermal system with homogeneous surface resistivity. As expected the inversion using the higher frequencies resolves the surface structure considerable better. At 1250 m North, the 5 layered structure is recovered in both the inversion models but the layers close to the surface are recovered better with the higher frequencies. At the 3000 m North, the high frequency model resolves the near surface more clearly.

Table 6.3: Skin depth for the new and the original frequencies. Skin depths are calculated using Equation 2.46 for a 22 Ωm homogeneous resistivity.

New freq [Hz]	Skin depth [m]	Original freq [Hz]	Skin depth [m]
$6.310 \cdot 10^1$	297	$1.000 \cdot 10^1$	747
$3.981 \cdot 10^1$	374	$3.981 \cdot 10^0$	1183
$1.585 \cdot 10^1$	593	$2.512 \cdot 10^0$	1489
$1.000 \cdot 10^1$	747	$1.585 \cdot 10^0$	1875
$6.310 \cdot 10^0$	940	$1.000 \cdot 10^0$	2361
$3.981 \cdot 10^0$	1183	$6.310 \cdot 10^{-1}$	2972
$1.585 \cdot 10^0$	1875	$3.981 \cdot 10^{-1}$	3741
$1.000 \cdot 10^0$	2361	$2.512 \cdot 10^{-1}$	4710
$6.310 \cdot 10^{-1}$	2972	$1.585 \cdot 10^{-1}$	5929
$3.981 \cdot 10^{-1}$	3741	$1.000 \cdot 10^{-1}$	7465
$1.585 \cdot 10^{-1}$	5929	$6.310 \cdot 10^{-2}$	9398
$1.000 \cdot 10^{-1}$	7465	$3.981 \cdot 10^{-2}$	11831
$6.310 \cdot 10^{-2}$	9398	$2.512 \cdot 10^{-2}$	14894
$3.981 \cdot 10^{-2}$	11831	$1.585 \cdot 10^{-2}$	18751
$1.585 \cdot 10^{-2}$	18751	$1.000 \cdot 10^{-2}$	23606
$1.000 \cdot 10^{-2}$	23606	$3.981 \cdot 10^{-3}$	37414

A continuous low resistivity coat surrounds the resistivity core, where the vertical boundary between the low resistivity coat and resistive core matches well the the original model. A high resistivity artifact is seen in the resistive core in the high frequency model, that does not correspond to any structure in the original model. The constraints to the doming of the deep low resistivity layer are also noticeable in the high frequency model, where both the vertical and horizontal boundaries of the dome are better match to that of the original model.

The models in Figure 6.21, show that the selection of the frequencies used in the inversion is important for the depth resolution of the inversion. For the synthetic geothermal model used in this project, the higher frequencies do better in resolving the near surface structures. This shows that the selection of the frequencies need to be considered carefully in order to ensure that the full potential of the data and inversion is achieved.

The non-uniqueness of the inversion procedure, implies that different models can produce data that fit the observed data to the same level of errors. Doing multiple inversions where the setup is changed in each one, for example the mesh or the frequencies, will provide models that can be compared. Structures that can be seen in multiple inversions are validated but inconsistencies need to be considered

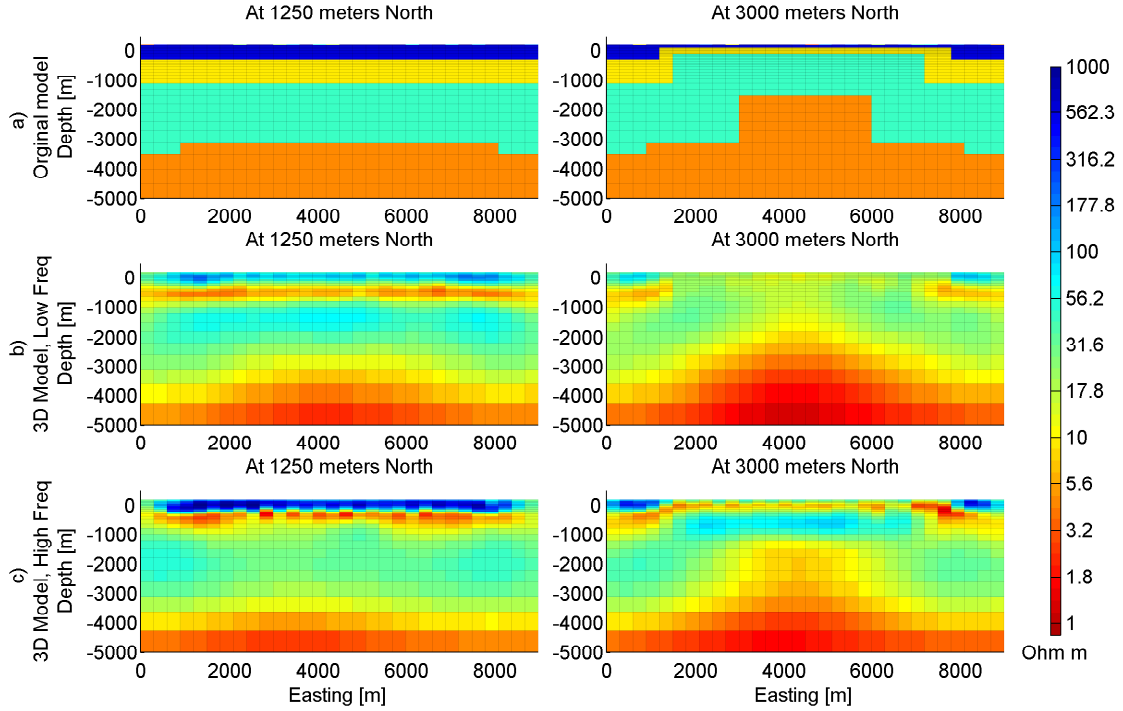


Figure 6.21: Cross sections comparing the synthetic geothermal system with homogeneous surface resistivity and the resulting inversion models using different frequencies of data. The inversions are done using the refined horizontal mesh discussed in Section 6.4.1. The original model is shown in row a), resulting model from an inversion using data in the original frequencies, discussed in Section 6.3.1, is shown in row b) and resulting model of new frequencies is shown in row c).

further. Rather than selecting one model to base all interpretation on, using a combination of multiple results will increase the confidence of the results and the final interpretation.

6.5 Discussion of inversion results

When the 3D models interpolated from joint 1D inversion of TEM and MT data, from the synthetic geothermal system with homogeneous surface resistivity (Section 6.3.1) and inhomogeneous surface resistivity (Section 6.3.2), are compared to the original models it is seen that the surface resistivity structure is recovered accurately. However, structures underneath the geothermal system are not resolved well. Since the static shift effects of the near surface inhomogeneities have been corrected during the inversion, we expect the recovered models to be similar.

The 3D inversions are over all better in recovering the resistivity structures at all depths. None of the resulting models from 3D inversions (in Section 6.3) resolve the surface resistivity in detail directly on top of the geothermal system. The thin horizontal layer of the low resistivity coat is not seen, it seems that the resistive core reaches the surface. The outer and inner vertical edges of the low resistivity coat are seen. In all the 3D models, non smoothness of adjoint cells in the near surface layers is clear but zones of similar resistivity can be seen and resolved. With increased depth, the 3D models have superior similarity with the original model. The doming of the deep low resistivity layer can be clearly resolved in all the models, though the exact extent of the doming is not recovered. The resistivity values are not directly compatible but the resistivity contrast is clearly seen. Sharp edges are not resolved, but that is to be expected since smoothness of the model is used in the regularization term of the object function.

Comparing the models from 3D inversions of MT data without and with static shift correction reveals over all similar models. Inversion of MT data without static shift correction recovers the general resistivity structure of the original models. The recovered models exceed expectations in recovering the original model. However, the inversion of MT data with static shift correction recovers the original model better, where the resistivity values and boundaries of structures are coincide more closely.

When performing a 3D inversion there are factors that affect the quality and resolution of the inversion, regardless whether static shift is present in the MT data or not. The refinement of the mesh increases the resolution of the recovered model but that is achieved with an increased computation time as illustrated in Table 6.2. All the recovered models in Figure 6.20 share the same general structures but details vary depending on the mesh, illustrating that verification of the inversion results is needed. Similarly, comparison of results from 3D inversions of MT data over different frequency ranges shows the importance of the frequencies selected for the inversion. By using the same number of frequencies but including higher frequencies improves the recovery of the near surface structures in the model, as well as enhancing the resolution of the boundaries of the doming of the deep low resistivity layer.

It is important to be critical of the inversion results and validate the model, especially when interpreting structures from the models. This may be done by comparing recovered models from multiple inversions where the data, mesh and/or other parameters of the inversion are changed. It is expected that results should differ but coinciding structures in the results gives assurance that the recoveries are accurate. Selecting the best model will always be subject to interpretation and needs to be considered on individual area basis.

7 Hengill geothermal area

In the following chapter, the inversions of EM data from the Hengill geothermal area are discussed as well as giving overview of the geology and previous work. The setup of the inversions are discussed, followed by results of the joint 1D inversion of TEM and MT data and two 3D inversion of the MT data, without and with static shift correction. Lastly, a discussion of the results and conclusion are given.

7.1 Overview of the Hengill geothermal area

The Hengill central volcano is located in Southwest Iceland, approximately 30 km East of Reykjavík. Hengill is in the Western Volcanic Zone and is cut by an active fissure swarm with a Southwest-Northeast direction. The geothermal field associated with Hengill is estimated to be approximately 110 km² in size and have the capacity of 690 MW_e for 50 years (Franzson et al., 2010). The Hengill geothermal area is often subdivided into 4 geothermal fields, Nesjavellir, Hellisheiði, Bitra and Hverahlíð, as seen in Figure 7.1.

The Hengill geothermal has installed power production of 330 MWe and 290 MW_{th} in the Nesjavellir and Hellisheiði fields (Franzson et al., 2010) and is currently the biggest geothermal power producing geothermal area in Iceland. During the exploration and development of the power plants, about 90 deep exploration, production and re-injection wells have been drilled into the systems at Nesjavellir and Hellisheiði. A few exploration wells have been drilled in Bitra and Hverahlíð, but no production wells have been drilled.

7.1.1 Geology

The Hengill central volcano complex is on junction of the Western Volcanic Zone (WVZ), Reykjanes Peninsula (RP) and the South Iceland Seismic Zone (SISZ) (Árnason et al., 2010). SISZ is the transform zone between the Reykjanes Peninsula oblique rift and the Eastern Volcanic Zone (EVZ) (Einarsson, 2008).

7 Hengill geothermal area

A major component of the volcanic system in the Hengill area is a 3-5 km wide and approximately 40 km long fissure swarm, seen as blue lines in Figure 7.1. The maximum volcanic activity is at the Hengill volcano, leading to accumulation of volcanic materials. The Hengill volcano is a tuya (table mountain), built up from hyaloclastite formations erupted during glacial periods (Franzson et al., 2005). Subaerial lavas erupted during interglacial periods have spread over the surrounding lowlands.

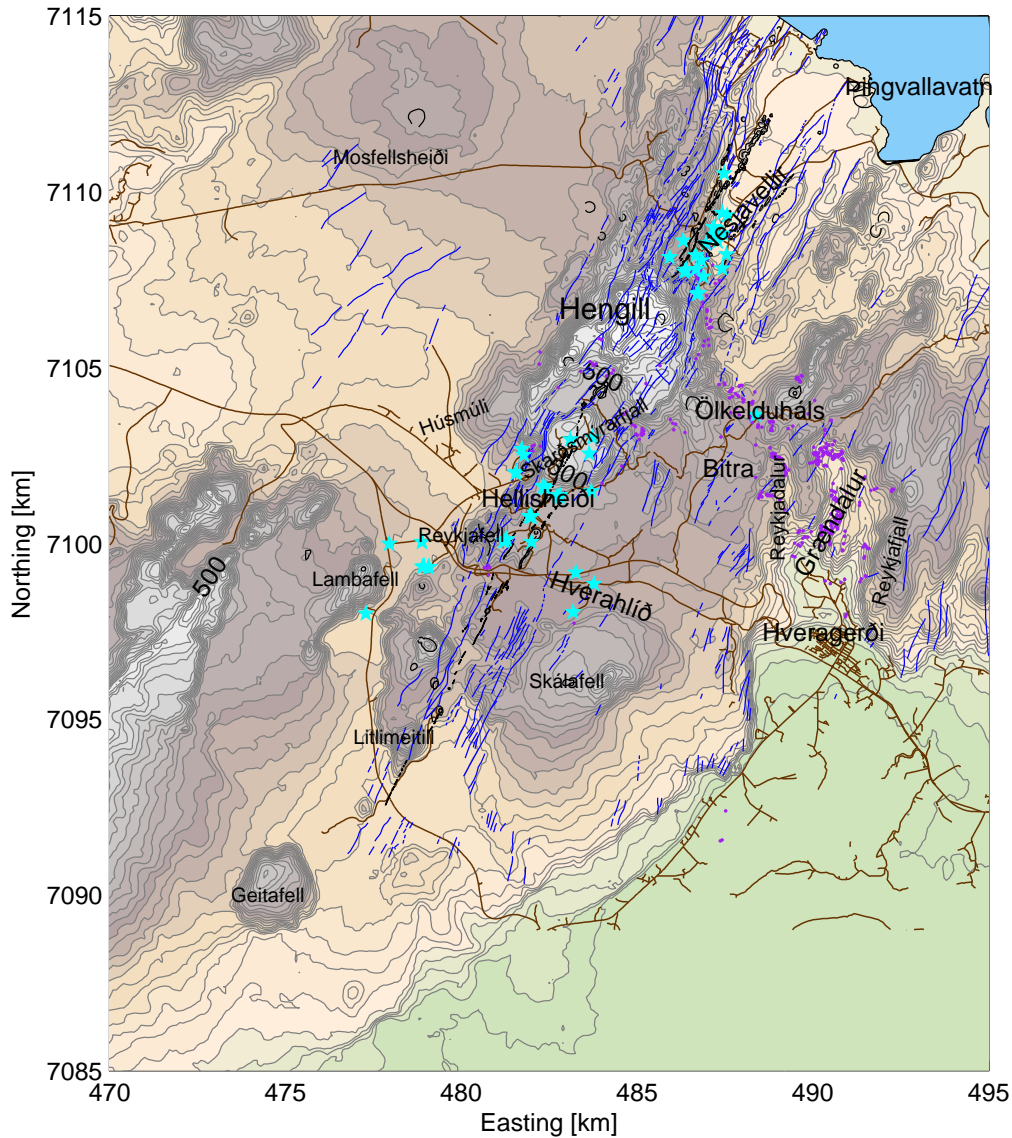


Figure 7.1: Topographic map of the Hengill area. Main roads are shown as brown lines, faults and fissures mapped on the surface as blue lines, volcanic craters and fissures as black lines, geothermal surface manifestations as purple dots and production boreholes as light blue stars.

Three lava eruptions have been recorded in the Hengill area since last glaciation, approximately 9, 5 and 2 thousand years ago (Franzson et al., 2010). The volcanic products in the Hengill volcano are mainly basaltic, but felsic and intermediate rocks are found in the Western part of the volcano. To the Southeast of Hengill are older volcanic complexes, i.e. Hrómundartindur that hosts the Bitra geothermal system and Grændalur just North of the town of Hveragerði (Figure 7.1). The majority of the seismic activity is found in the area near Hrómundartindur and Grændalur. In the years 1991-2001, over 90,000 earthquakes were recorded in the area. A majority of these earthquakes were related to inflation of the ground caused by a magmatic intrusion at 6-7 km depth beneath Hrómundartindur (Sigmundsson et al., 1997).

In the Hengill geothermal system, permeability is considered to be controlled by boundaries of intrusions and major faults. Basaltic dykes from fissure eruptions 5 and 2 thousand years ago, with a Southwest-Northeast strike direction, are of special interest (black lines in Figure 7.1). The dykes are expected to be the major flow channels of the geothermal fluids from the upflow zone in the central part of the Hengill volcano towards the South and North, feeding the Hellisheiði and Nesjavellir geothermal fields, respectively (Franzson et al., 2005).

Substantial surface hydrothermal alteration is found in the Hengill area, in particular at the Hengill volcano itself. Hydrothermal alteration shows coincidence with tectonic faults and fissures in the area, but is mainly due to past activity. Geothermal activity on the surface have been mapped in the area (purple dots in Figure 7.1). Most of the surface activity lies on a Northwest-Southeast line, from Nesjavellir in the North to Hveragerði in the Southeast.

7.1.2 Previous geophysical work

The Hengill geothermal area has been explored by various methods. Hersir et al. (1990a) give an overview and results of the exploration in the Hengill area. In their report the location and interpretation of DC-resistivity measurements, airborne magnetic measurements, gravity measurements, MT-soundings and passive seismic measurements are discussed and main results of each individual survey are given. The report also jointly interprets the results, providing a conceptual picture of the geothermal activity based on these surveys.

In the year 1984, exploration activity increased due to the development of the geothermal power plant in Nesjavellir, which started production in 1990. Central loop TEM surveys were tested in 1987 in the Hengill area and were found more effective than the DC-resistivity methods used previously, due to lower costs and simpler interpretation. An extensive network of 280 TEM soundings has been collected in the Hengill area, using 300 by 300 m transmitter loops with current in the

order of 20 A. Árnason and Magnússon (2001) inverted 186 TEM soundings with 1D inversion modeling providing maps and sections of the resistivity down to about 1000 m depth below the surface. A detailed analysis of earthquake epicenters during the period from 1990 to 2000 is also discussed by Árnason and Magnússon (2001). MT soundings were first carried out in the Hengill area in 1976 and 1982 (Hersir et al., 1990a,b). Since then 4 major MT sounding campaigns have been carried out in the Hengill area (Árnason et al., 2010). Locations of MT soundings were selected close to previously measured TEM soundings. As a part of the I-GET project, a joint 1D inversion of 148 TEM and MT soundings and a 3D inversion of 60 MT soundings in the Hengill area was done (Árnason et al., 2010).

7.2 Setup of inversions

7.2.1 TEM and MT data

The MT data used for this project are the same as in Árnason et al. (2010). After filtering out soundings of bad quality, some 136 MT soundings are used in this study. The data was collected with Phoenix MTU instruments with a remote reference station. During the data collection 5-component instruments, with 2 orthogonal electric dipoles and 3 magnetic sensors, and 2-component instruments, with only 2 orthogonal electric dipoles, were used. The survey was organized such that 2-component instruments were set up in close proximity of a 5-component instrument, and the measured magnetic fields are used for both stations. The instruments were moved daily, on average providing about 20 hrs of recordings at each location. The highest frequency recorded was 294 Hz and the lowest frequency usually in the range of 10^{-2} to 10^{-3} Hz. Locations of the MT soundings used in this study are shown in Figure 7.2.

The TEM data in Hengill has been collected since 1987. From the 280 TEM soundings done in the area, only TEM soundings in close proximity of the MT soundings are used in this study. The wave form used was exponential turn on and a linear turn off. Commonly, the data was collected for 2 different frequencies of the current signal, 25 and 2.5 Hz. This gives increased depth range for each sounding. The transient was collected at the center of the source loop at 20 time gates for each of the frequency that are equally spaced on log scale from 88.13 μ s to 68.78 ms after the current is turned off.

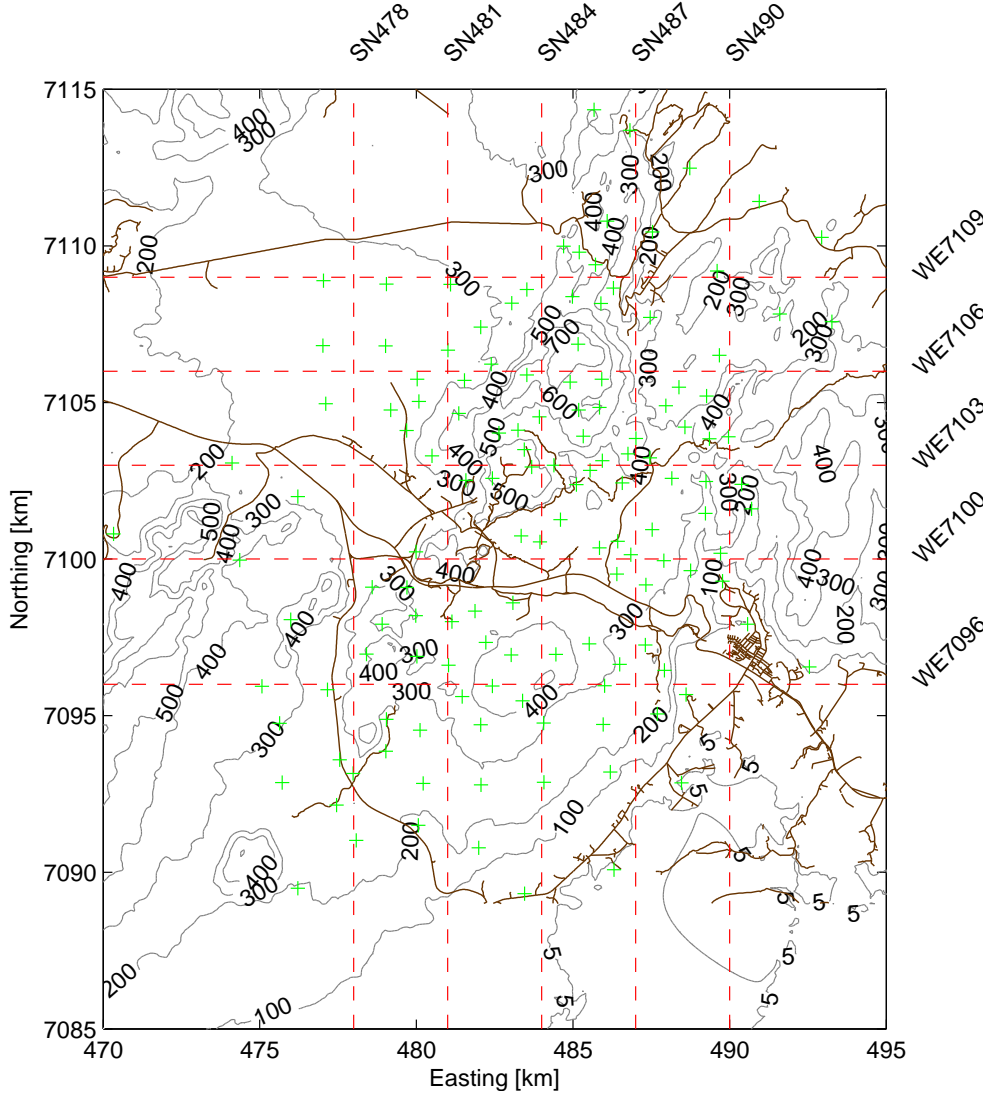


Figure 7.2: Contour map of Hengill area with contour lines at 100 m interval in light gray, roads are shown as brown lines, MT sounding locations are shown as green plus signs and SN and WE cross sections are shown as broken red lines.

7.2.2 Joint 1D inversion

1D inversion was done with TEMTD program, discussed in 4.2.1, using Occam inversion. The setup of the inversions was the same as discussed in Section 6.2.3, using 29 layers down to 40 km depth.

The joint 1D inversion of the TEM and the xy and yx elements of the MT impedance was done in order to estimate the static shift multipliers. In most cases the frequency range of 100 Hz to 0.001 Hz was used but in some cases additional frequencies were

excluded from the inversion due to data quality. When the agreement between the TEM and MT data was poor, either the last time gates of the TEM data or the highest frequencies of the MT data were excluded in order to improve the fit. The joint inversions of TEM and the determinant of the MT impedance tensor, had been previously done for the data and published in Árnason et al. (2010).

For comparison with 3D model results, the resulting models for joint 1D inversion of TEM and MT determinant are interpolated onto the mesh used for the 3D inversion. The resistivity of each cell in the 1D models is assigned the x, y, z, coordinate where the x and y are the Easting and Northing location of the sounding and z is the elevation of the cell center from sea level. To compare the data fit of the 3D model constructed from the 1D inversion results, the model is forward calculated so that the xy and yx modes for the 3D model can be compared to the observed xy and yx data modes.

7.2.3 3D inversion

3D inversion is done with MT3Dinv, discussed in 4.2.4. The inversion is done using the real and imaginary parts of the off diagonal elements of the impedance tensor. The initial and background models were all set as a halfspace of $17 \Omega\text{m}$, which is the halfspace resistivity that minimizes the overall data misfit. Bounds for the resistivity were set to be in the range of 0.5 and $2000 \Omega\text{m}$. The weight of the smallness was set to $2.5 \cdot 10^{-8}$ and the smoothness to 1. On new beta iteration, the reference model was updated with the resulting model from the previous beta iteration.

Before the inversion, the MT data were checked for quality and 12 MT soundings were excluded from the original data set and the inversion due to large errors and difficulties to invert in 1D. The standard deviations used for the inversion were 10% of the data value plus a floor that was 10% of the mean value of each frequency. The standard deviations include all sources of errors in the inversion and data.

The same 16 frequencies are used as in the inversion of synthetic data discussed in Section 6.3. They cover 3.5 decades of frequency

10.00	3.981	2.512	1.585
1.000	0.631	0.3981	0.2512
0.1585	0.100	0.0631	0.03981
0.02512	0.01585	0.0100	0.003981

Estimated skindepths, using Equation 2.46, for a $17 \Omega\text{m}$ halfspace over these frequencies range from 637 m to 31907 m, which covers well the expected target depths of interest.

For the 3D inversion of the MT data and model interpolation of 1D inversion models, a mesh was used that has 45 by 50 by 48 cells covering a total volume of 172 by 177 by 127 km in the Easting, Northing and vertical, respectively. The area of interest was selected to extend from 470 to 495 (UTM km) in the Easting and 7085 to 7115 (UTM km) in the Northing (Figure 7.1) and is covered by 1000 by 1000 m wide cells. Outside of the area of interest is padded by 10 cells that expand by a factor of 1.3 to 20000 m. The thinnest cells are 100 m thick and topography was modeled in the mesh. The total number of cells in the mesh is 108,000.

7.3 Inversion results

In the following sections, results of joint 1D TEM and MT inversions and 3D inversions for the Hengill geothermal area are shown. The results of individual models are discussed first followed by comparison of the results and discussion.

7.3.1 1D inversion models

Results of the joint 1D TEM and MT inversion for the apparent resistivity of the determinant of the impedance tensor are shown and discussed briefly below. The 1D inversions were performed as described in section 7.2.

Iso-elevation maps of the 3D model interpolated from joint TEM and MT 1D inversions are shown in Figure 7.3. At an elevation of 300 m above sea level, a clear low resistivity area can be seen at the Hengill volcano, surrounded by higher resistivity. As the elevation decreases the low resistivity area grows in size, and at sea level it extends to the whole Hengill volcano. The area around Hverahlíð, enclosed by loop of roads, is decreasing in resistivity. The resistivity under the Hengill volcano is starting to increase at -200 m and expands on a Northwest-Southeast axis with increased depth. At -1000 m, the resistive area has grown in size and covers the area from Hverahlíð in the South to Nesjavellir in the North. From -2000 to -6000 m, low resistivity below the Hengill may be seen. An average resistivity of 10 Ohm m covers most of the area at -10000 m.

Figure 7.4 shows South-North cross sections of the 3D model interpolated from joint 1D TEM and MT inversions (the locations of the cross sections are shown in Figure 7.2). A layered structure, similar to that of the layered background model used in chapter 6 is seen in cross section a). A clear exception is noticeable between 7095 and 7100 Northing, in range -4 to -6 km where there is a low resistivity body in the resistive layer. In cross sections b), c) and d) the low resistivity at and close to

7 Hengill geothermal area

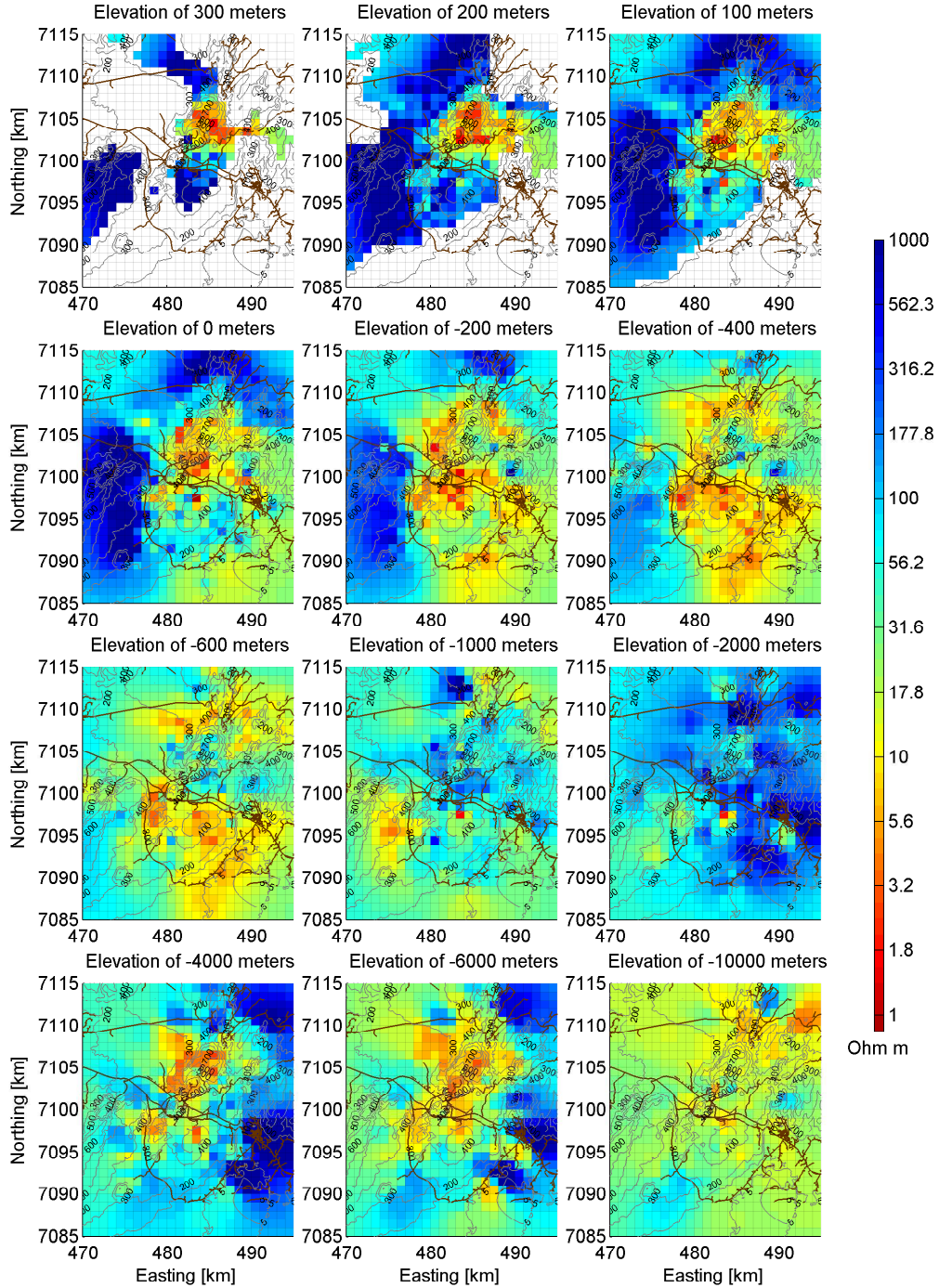


Figure 7.3: Iso-elevation maps for a 3D model of interpolated joint 1D TEM/MT inversion. Topography and roads in the area are plotted as well as light gray and brown lines, respectively. The increasing size of the low resistivity under the Hengill volcano is seen in the range from 300 to 1000 m with a resistive ridge developing in the same location at increased depth.

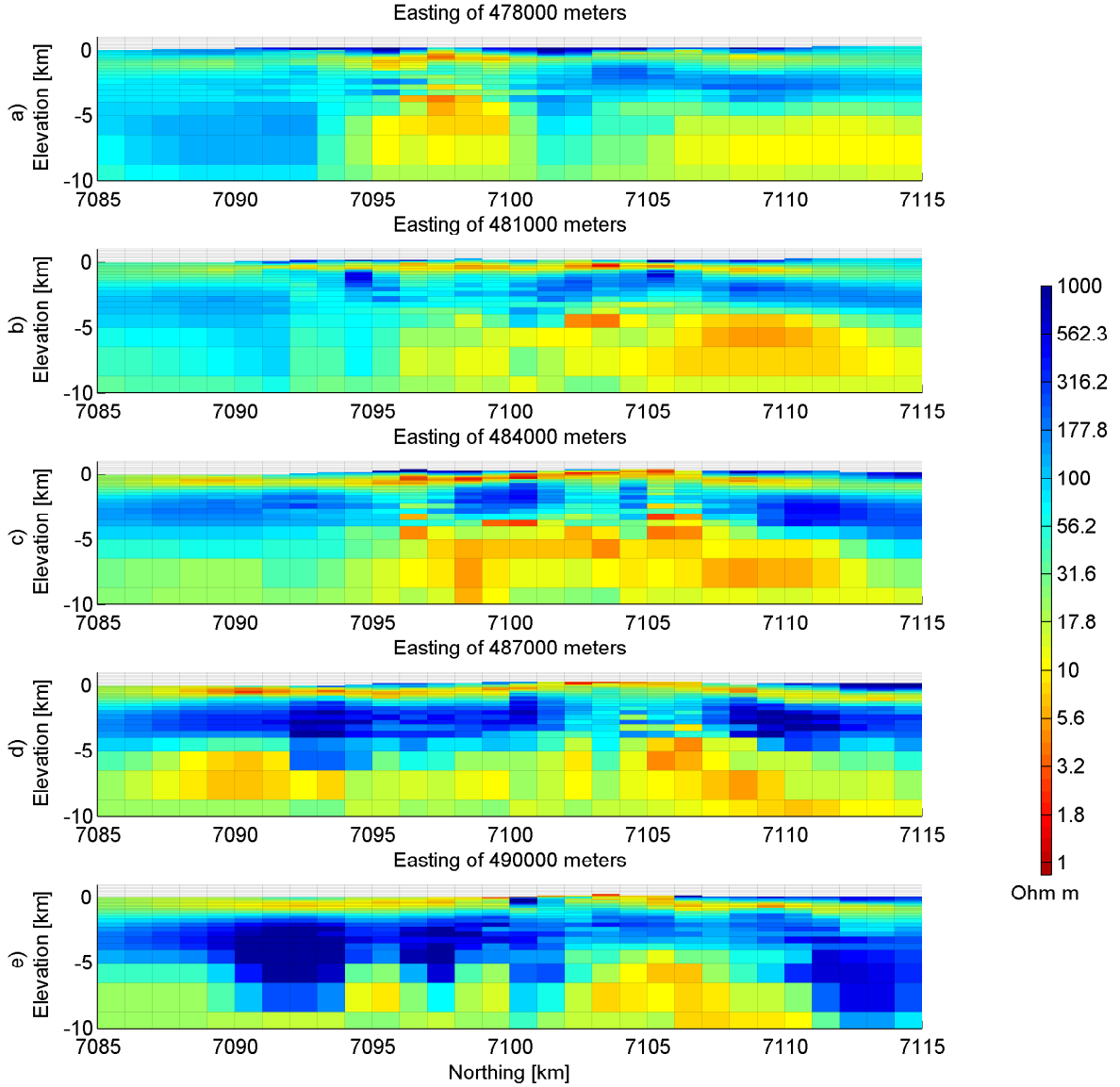


Figure 7.4: South-North cross sections of a 3D model of interpolated joint 1D TEM/MT inversion.

the surface, outlines the geothermal system. The deep low resistivity layer beneath most of the area, domes up to -3 km at approximately 7097 and 7106 Northing. The shape and the resistivity of the doming varies considerable, making it hard to define details of the doming. In cross section e) the deep low resistivity layer has mostly faded and a layer structure is observed.

West-East oriented cross sections of the 3D model interpolated from joint 1D TEM and MT inversions are illustrated in Figure 7.5 (location of the cross sections is shown in Figure 7.2). In cross section a), layers of high resistivity are at the surface,

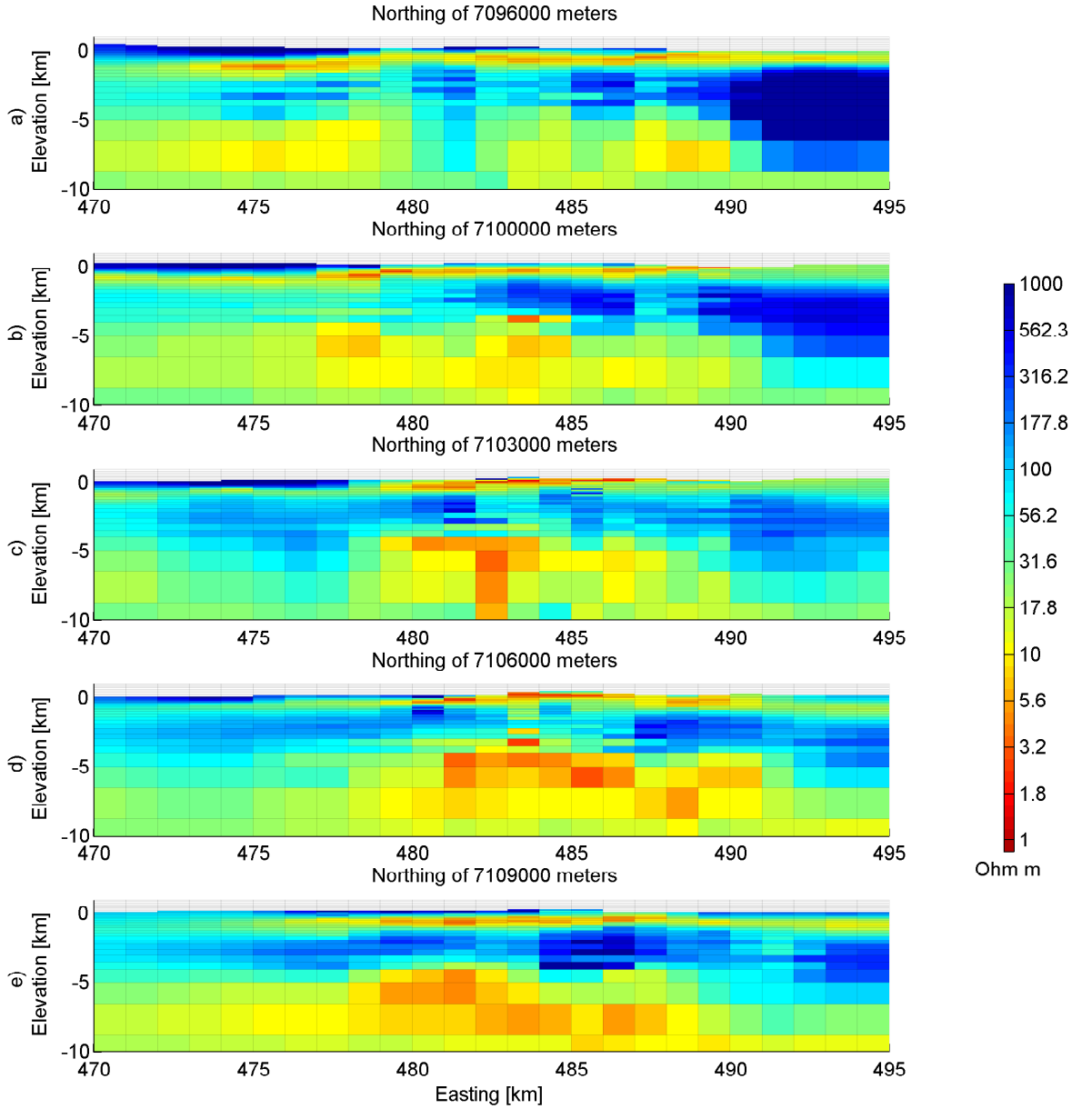


Figure 7.5: West-East cross sections of a 3D model of interpolated joint 1D TEM/MT inversion. The sections have layered structure but extension towards the surface around the Hengill volcano in section c).

low resistivity layer close the surface, resistive layer and then a lower resistivity close to the bottom of the section. In cross section b), the shallow low resistivity layer ascends towards the surface. In cross sections c) and d) the low resistivity reaches the surface around the Hengill volcano, at 484 Easting. The deep low resistivity domes upwards and in section d) reaches to -3 km. In section e), the shallow low resistivity has descended from the surface and the doming of the deep low resistivity

subsides to greater depths.

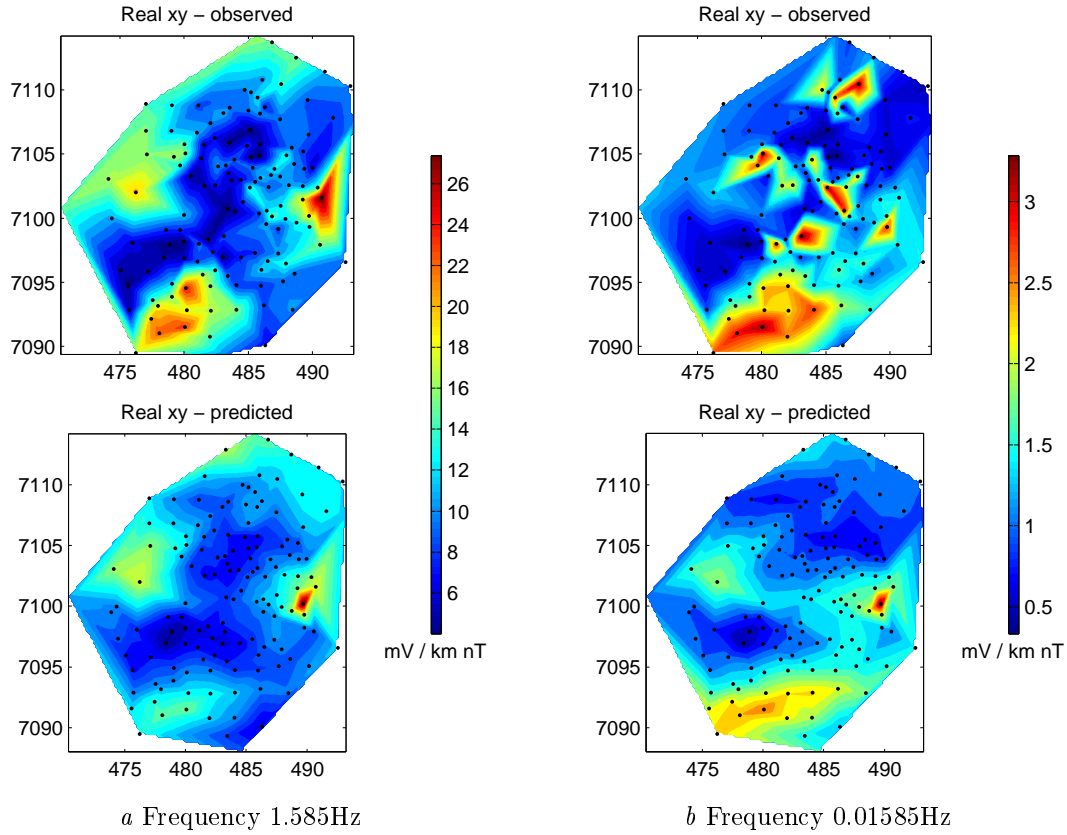


Figure 7.6: Real part of xy observed and predicted data at two frequencies, for the Hengill area. The observed data is the static shift corrected MT data and the predicted data is forward calculated data from the 3D model interpolated from the 1D models for a joint inversion TEM and MT from the Hengill area. As seen for the synthetic data (e.g. Figure 6.7), there is resemblance between the predicted and observed data but the details in shape and amplitude of data anomalies do not match well.

The real parts of xy impedance element for the observed and predicted data for the Hengill area are shown for two frequencies in Figure 7.6. The predicted data is forward calculated from the model shown in Figures 7.3, 7.4 and 7.5. For the high frequency in Figure 7.6a, the predicted data does not agree well with the observed data. There is general resemblance with the data, where similar features are present but the amplitude and boundaries do not coincide well. Similarly, for the lower frequency in Figure 7.6b, there is a general resemblance of the data but no details agree.

7.3.2 3D inversion models without static shift correction

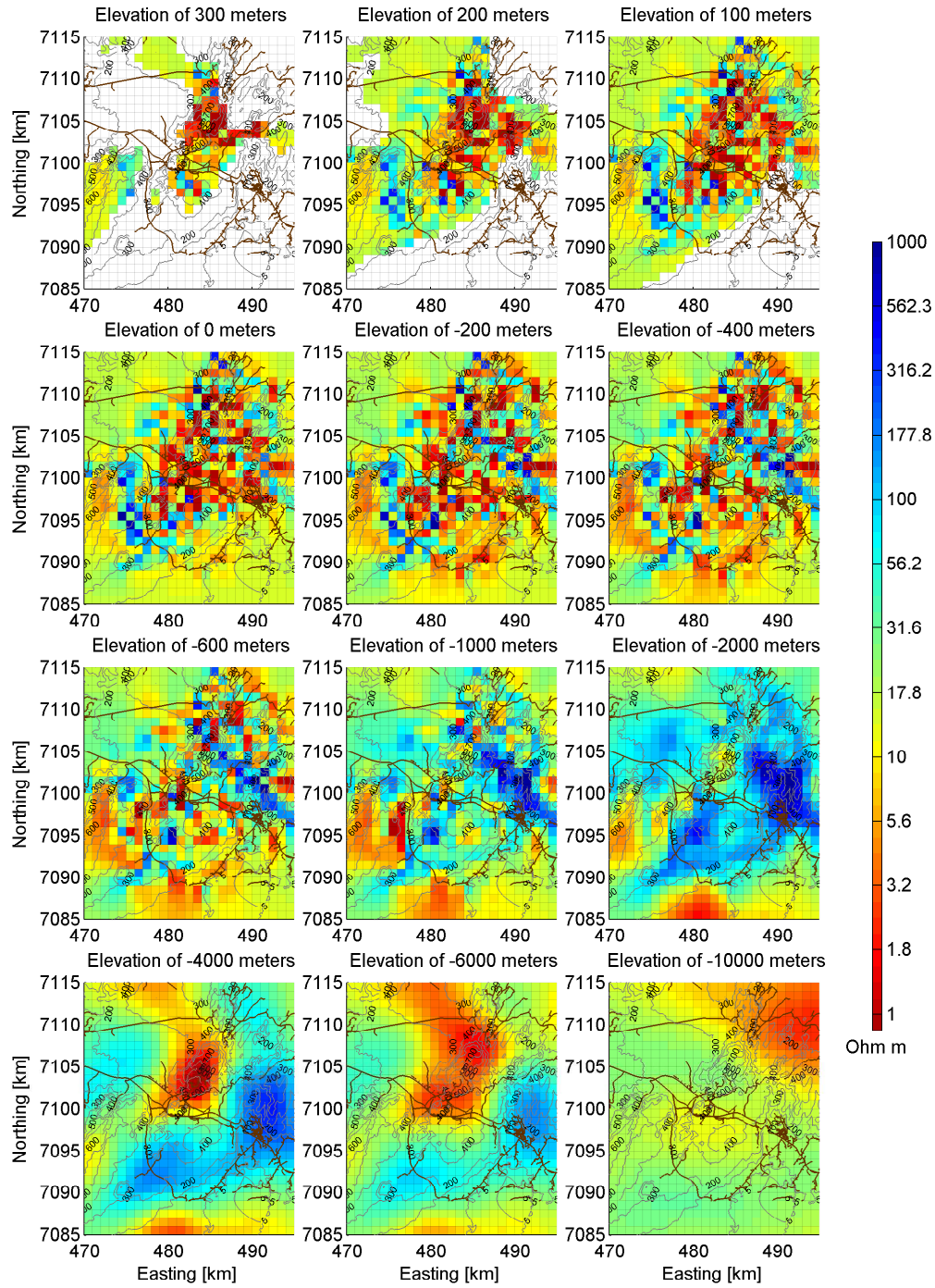


Figure 7.7: Iso-elevation maps of a model from a 3D inversion of MT data where static shift correction has not been applied prior to the inversion. Topography and roads in the area are plotted as well as light gray and brown lines, respectively.

The inversion was set up as described in section 7.2. The target misfit was $8.32 \cdot 10^3$

and the inversion reached a misfit of $2.83 \cdot 10^4$. A total of 20 iterations were done, for 4 beta trade-off values with the final beta as $4.44 \cdot 10^{-4}$. It took 44 hours and 21 min on 8 Intel®Xeon®CPU's E5410 with 2.33 GHz speed to complete the inversion.

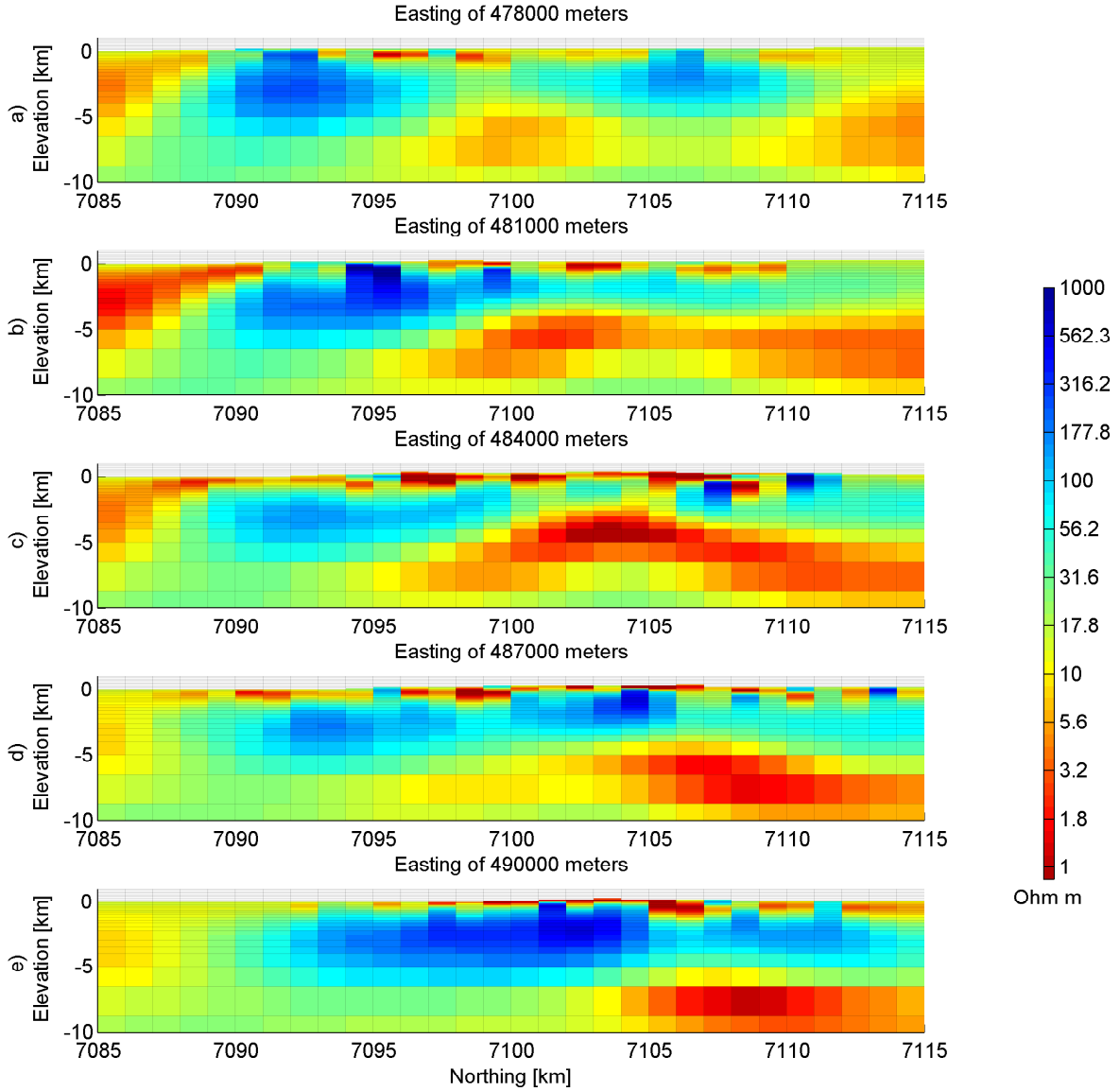


Figure 7.8: South-North cross sections of the model from the 3D inversions of MT data without static shift correction prior to the inversion.

The resulting model from a 3D inversion of MT data without static shift correction are shown as iso-elevation maps in Figure 7.7. At 300 m, low resistivity is seen at the Hengill volcano. There are clear variations of the resistivity in adjoint cells, but this is required in order for the inversion to be able to fit the data appropriately. At 200 m and 100 m the low resistivity area increases in size and at sea level it covers the area from the Hengill volcano in the North and to Hverahlíð in the South. There

7 Hengill geothermal area

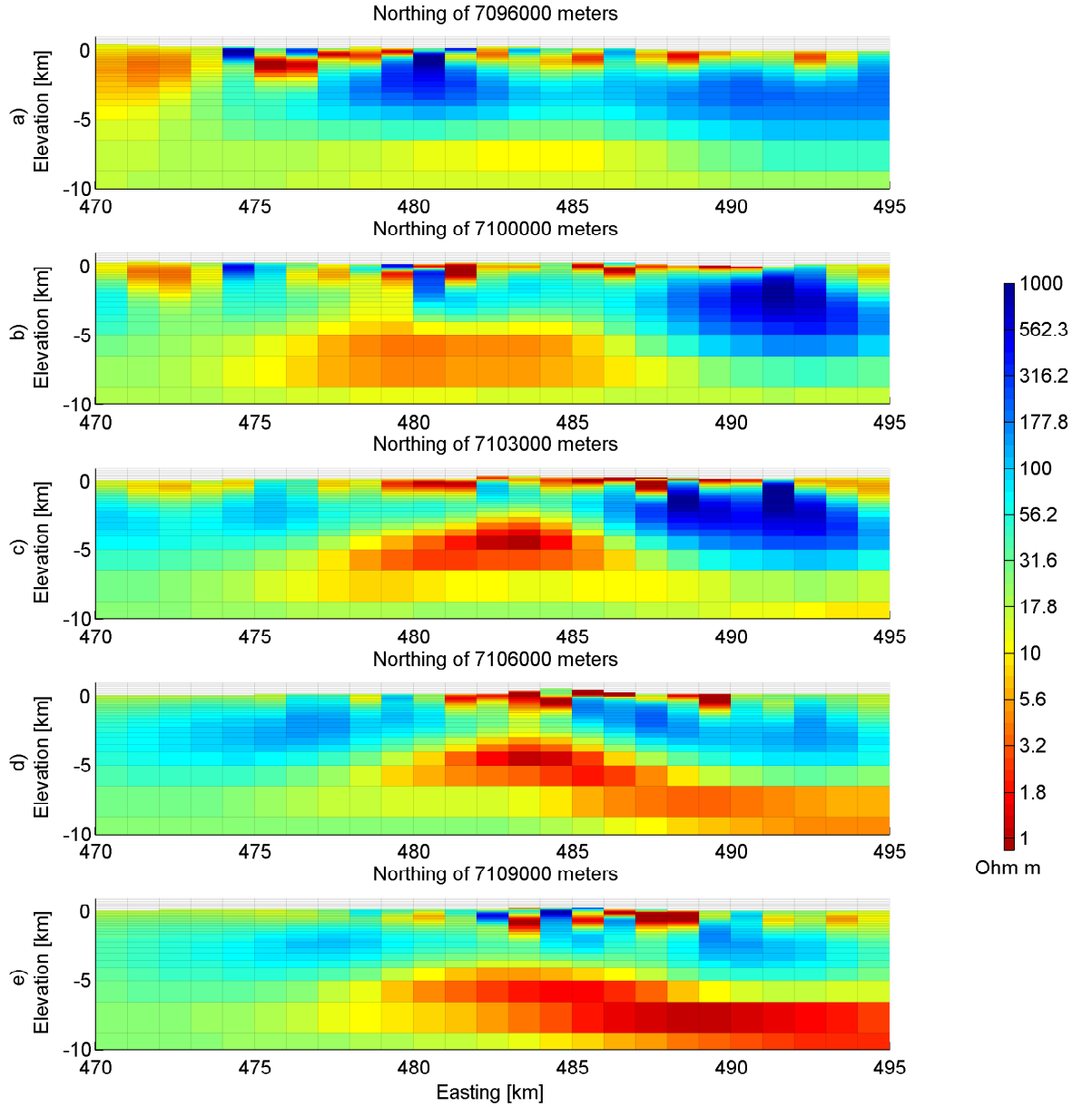


Figure 7.9: West-East cross sections of the model from the 3D inversions of MT data without static shift correction prior to the inversion.

is higher resistivity around the edges and a linear high resistivity ridge is noticeable, reaching from the Hengill volcano towards the Southeast. At -200 m and -400 m, the high resistivity ridge becomes more defined and the low resistivity dissipates. At -600 m and -1000 m, the high resistivity ridge and an area of higher resistivity South of Hverahlið are observed, that at -2000 m becomes connected. At -4000 m, there is a low resistivity doming beneath the Hengill volcano surrounded by higher resistivity and at -6000 m the doming has increased in size and the high resistivity dissipated. At -10000 m, the Northeast has lower resistivity while other areas have

moderate resistivity in the range of $20 \Omega\text{m}$.

South-North oriented cross sections for a model from a 3D inversion of MT data without static shift correction are shown in Figure 7.8 (location of the cross sections is shown in Figure 7.2). In cross section a), a resistivity in the order of $5 \Omega\text{m}$ can be seen at the surface in the central part of the section with higher resistivity bodies to the sides. A dome in the deep low resistivity layer is seen in the depth range of -5 to -9 km, centered at 7100 Northing. In section b), the deep low resistivity layer has extended to the North and risen to -4 km between 7100 and 7105 Northing. The amplitude of the surface low resistivity has decreased. In section c), the deep low resistivity dome has risen to -3 km underneath Hengill, at 7103 Northing. The surface low resistivity layer is thinnest at Hengill. In section d) and e), the low resistivity surface layer dissipates and the resistive layer becomes dominant. The doming of the deep low resistivity layer vanishes.

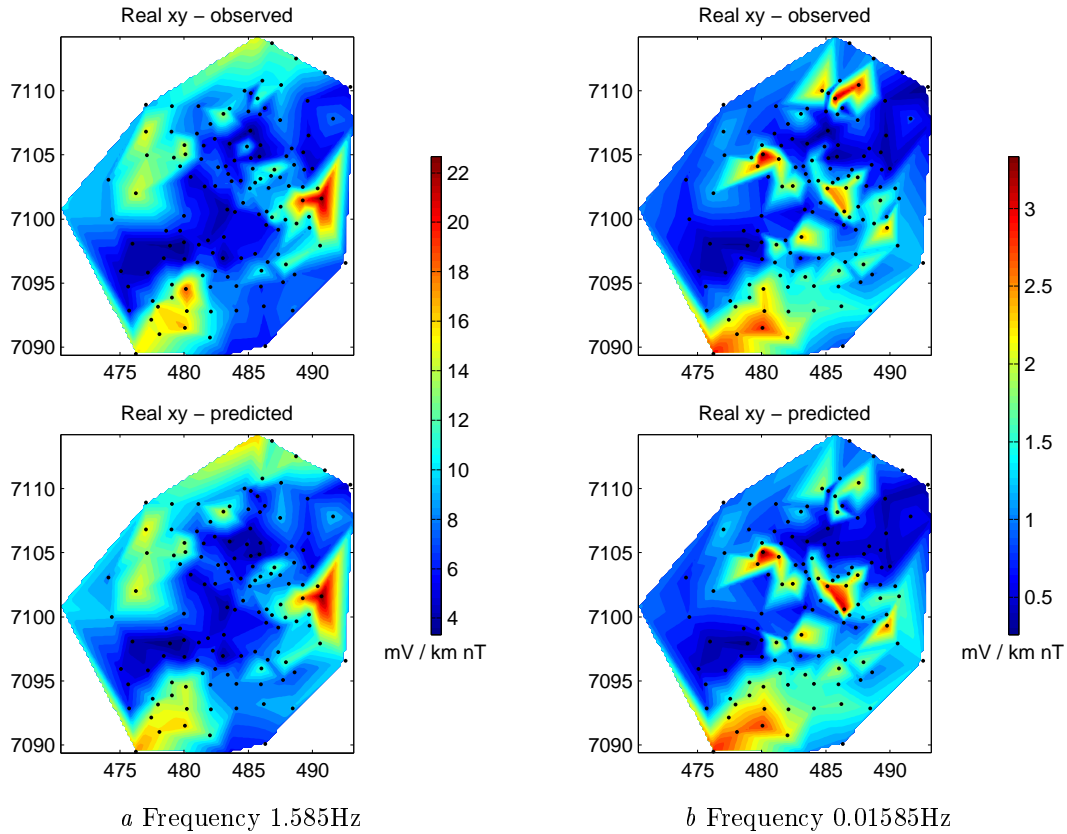


Figure 7.10: Real part of xy observed and predicted data of a 3D inversion for the Hengill area without static shift correction of the observed data prior to inversion. Comparison of the predicted and observed data reveals a close agreement, where boundaries and amplitude of anomalies are well defined.

Figure 7.9 shows West-East oriented cross sections for the model (location of the

cross sections is shown in Figure 7.2). In cross section a), close to the surface a high resistivity is followed by a low resistivity that are somewhat mixed. Below that is a thick layer of high resistivity in the range of -1.5 to -5 km that is followed by lower resistivity at the bottom. In section b), at the surface low resistivity has become dominant, the resistive mid layers are not as defined and a low resistivity body is seen at range of -5 to -9 km from 475 to 485 Easting. In sections c) and d), the doming of the deep low resistivity layer is noticeable, reaching depth of -3.5 km. Then in section e), the doming has dissipated but the low resistivity layer is pronounced at the bottom.

Iso-frequency maps of the observed and predicted data for the inversion are shown in Figure 7.10. For both the higher frequency (Figure 7.10a) and the lower frequency (Figure 7.10b), the agreement of the predicted and the observed data is good. All the general features and boundaries in the observed data are well matched in the predicted. The agreement of the predicted and observed data in Figure 7.10 is superior to that for the 3D model interpolated from 1D models (Figure 7.6).

7.3.3 3D inversion models with static shift correction

The static shift multipliers were estimated from a joint 1D TEM and MT inversion for each of the xy and yx modes of the MT tensor. These estimates of the static shift are used for correction of the impedance tensor, as discussed in Section 3.3. Maps of the static shift multipliers can be seen in Figure 6.9.

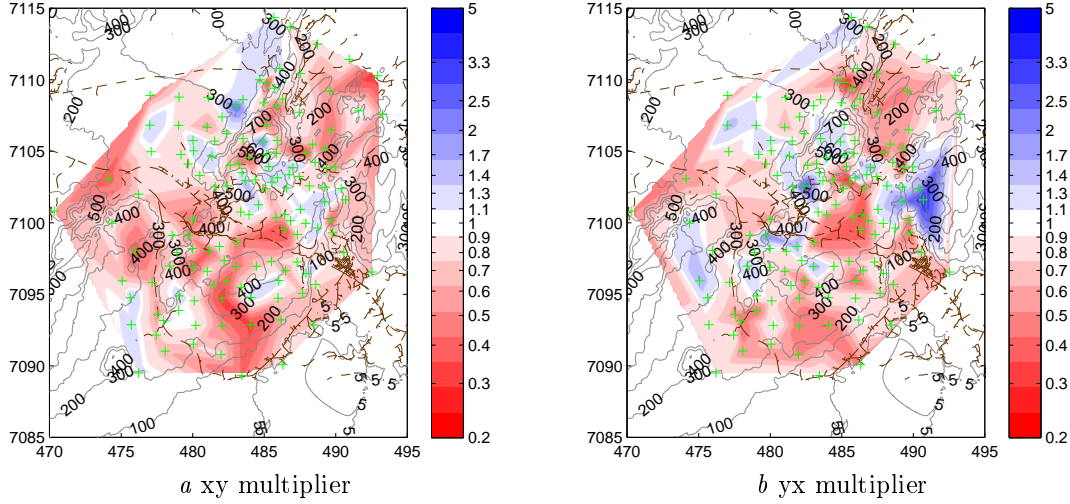


Figure 7.11: Maps of xy and yx static shift multipliers for Hengill geothermal system. The static shift multipliers are estimated from individual 1D joint inversion of TEM and MT data for the xy and yx modes. Topography and roads in the area are shown as light gray and brown lines, respectively.

The inversion was set up as described in section 7.2. The target misfit was $8.32 \cdot 10^3$ and the inversion reached a misfit of $1.27 \cdot 10^4$. A total of 20 iterations were done, for 4 beta trade-off values with the final beta as $2.60 \cdot 10^{-4}$. The inversion took 21 hours and 56 min on 8 Intel®Xeon®X5660 CPU's with 2.80 GHz speed each to complete the inversion which is half the time that was needed to complete the inversion for the MT data without static shift correction. The improvement in time, is due to different computers being used for the inversion. The final misfit of this inversion is considerable better as compared to the inversion for the MT data without static shift correction (Section 7.3.2).

The iso-elevation maps in Figures 7.12 and 7.7 are similar. In the resulting model from the 3D inversion of the MT data with static shift correction (Figure 7.12), the low resistivity at the near surface is smoother and more condensed. With depth, the low resistivity increases in size and in the center breaks up with higher resistivity structure that appears to have a strike direction to the Southwest-Northeast and Northwest-Southeast. At -200 m and -400 m, a high resistivity ridge starts to appear from the Hengill volcano to the Southeast. At -600 m and -1000 m, the

7 Hengill geothermal area

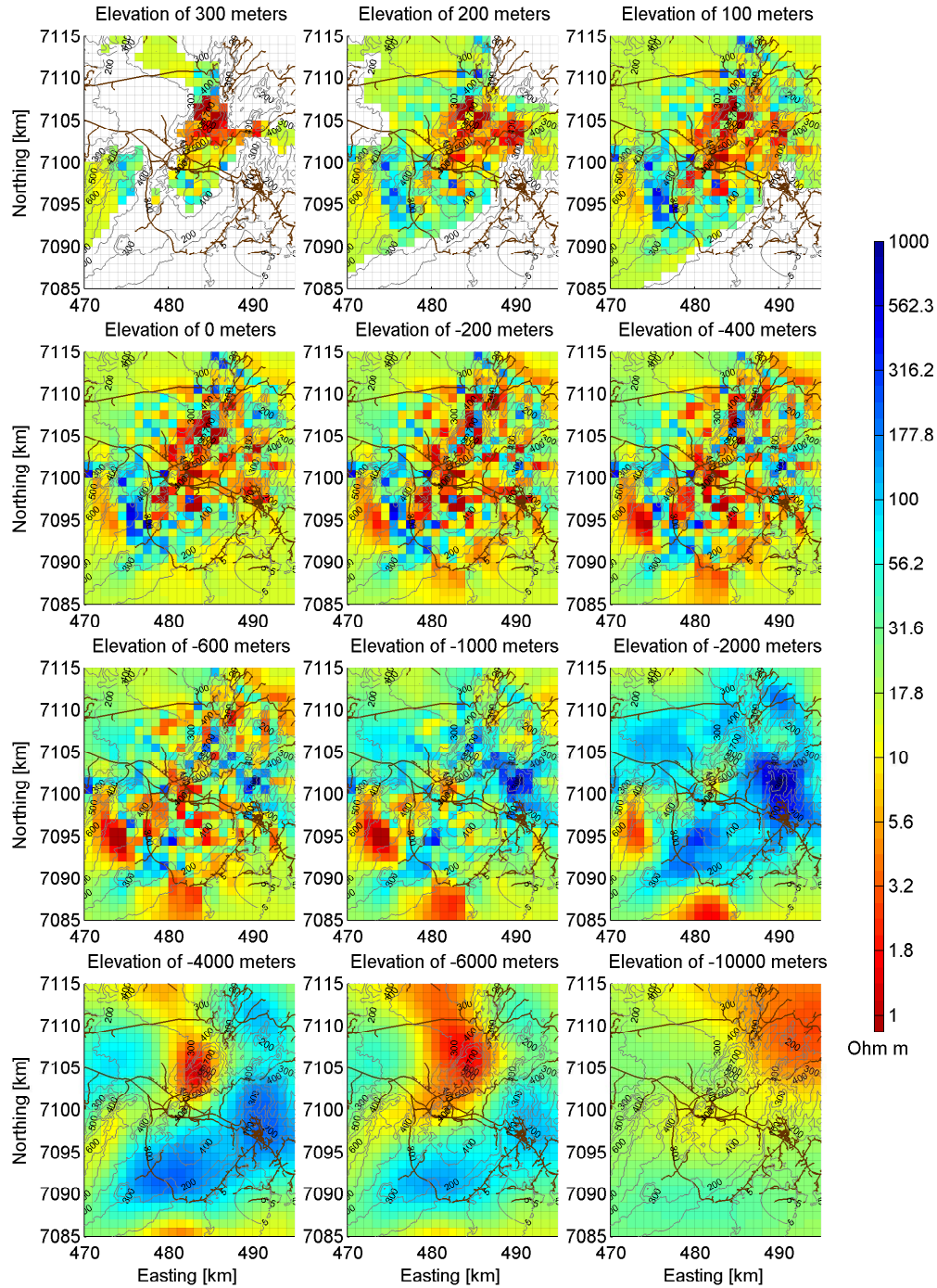


Figure 7.12: Iso-elevation maps of the model from the 3D inversion of the MT data with static shift correction prior to the inversion. Topography and roads in the area are shown as light gray and brown lines, respectively.

high resistivity ridge becomes more visible but does not become as striking as in the model from the MT data without static shift correction (Figure 7.7). High

resistivities in the ridge and on the edges connect at -2000 m forming a consistent high resistivity at this depth. At -4000 m and -6000 m, a doming beneath the Hengill volcano appears from the lower resistivity layer at -10000 m.

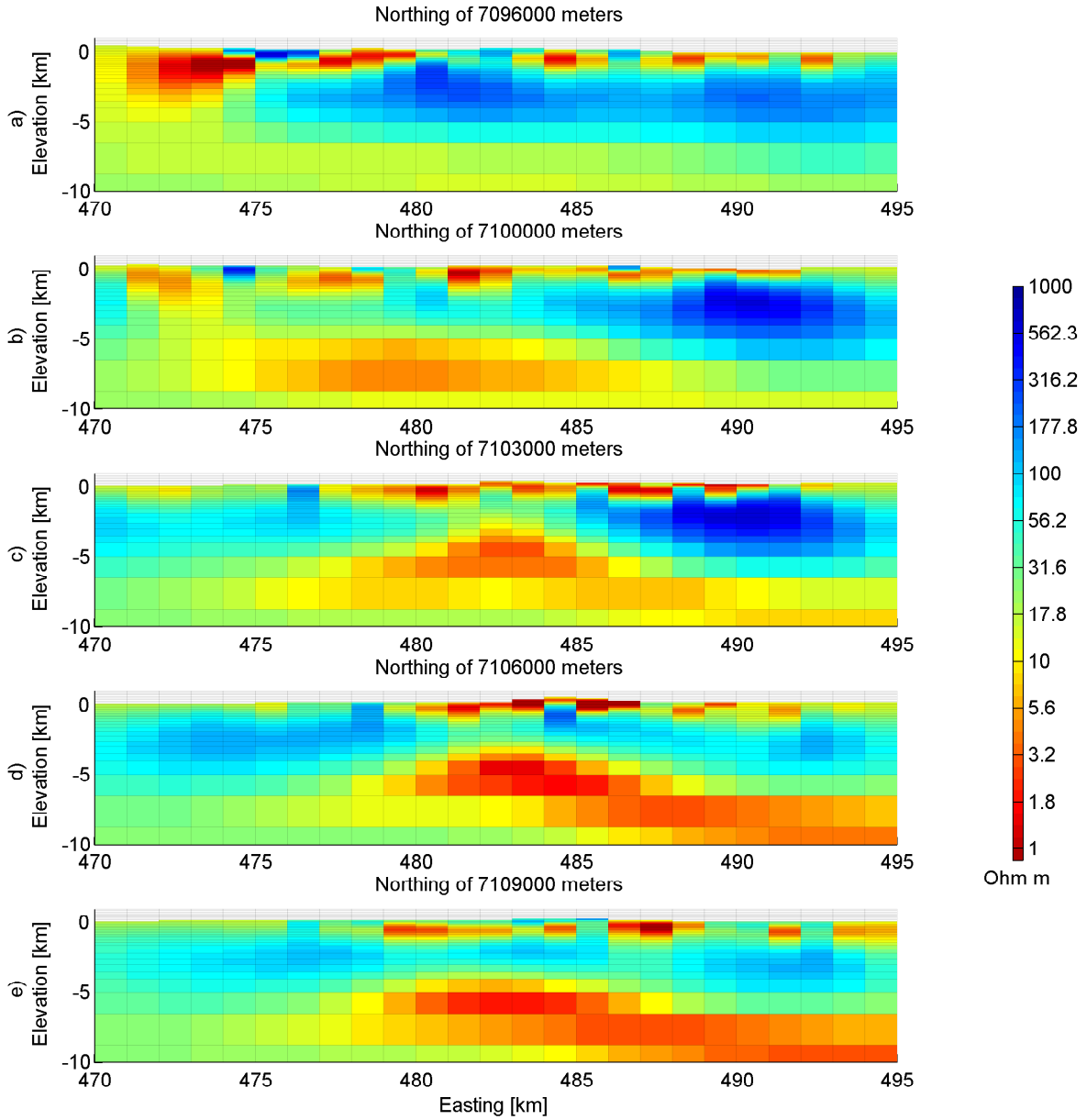


Figure 7.13: West-East cross sections of the model from the 3D inversions of the MT data with static shift correction prior to the inversion.

West-East oriented cross sections for a model from a 3D inversion are shown in Figure 7.13 (location of the cross sections in Figure 7.2). In section a), a layered resistivity structure can be seen, with higher resistivity at the surface followed by a low resistivity layer at depths shallower than -1 km. A resistive layer is seen at depths from -1 km to -5 km and followed by a low resistivity towards the bottom.

7 Hengill geothermal area

In section b), the resistive mid layer decreases in resistivity in Western side till 485 Easting and in the same area the deep low resistivity has become more noticeable. In section c), doming of the deep low resistivity reaches to -2 km and at the surface low resistivity is dominant. In sections d) and e), the dome of the deep low resistivity subsides and the surface resistivity increases. The resistive mid layer, becomes more continuous as well.

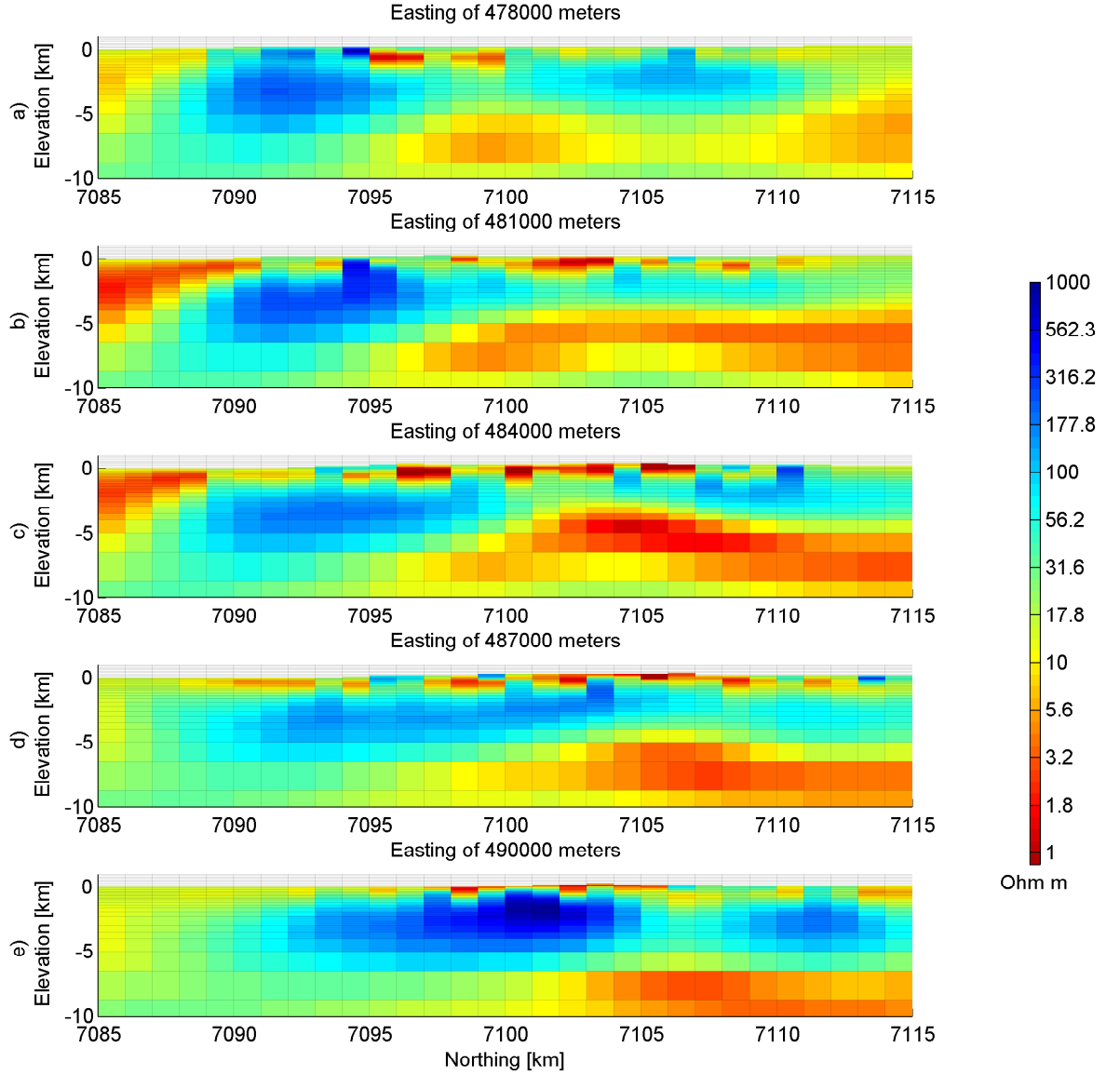


Figure 7.14: South-North cross sections of the model from the 3D inversions of the MT data with static shift correction prior to the inversion.

South-North oriented cross section for the model from the 3D inversion of the MT data with static shift correction are shown in Figure 7.14 (location of the cross sections in Figure 7.2). In section a), 2 resistive bodies centered at 7093 and 7107

Nothing are noticeable. A low resistivity layer is seen close to the surface between these bodies and the deep low resistivity has 2 closely connected bodies at depth of -7 km at 7100 Northing and at the Northern edge. In section b), the deep low resistivity layer is continuous, the Northern more resistive body has vanished and the surface has come less resistive. In section c), the surface resistivity is low and doming of the deep low resistivity layer reaches -4 km. In sections d) and e), the deep low resistivity subsides and a layered resistivity structure becomes clear.

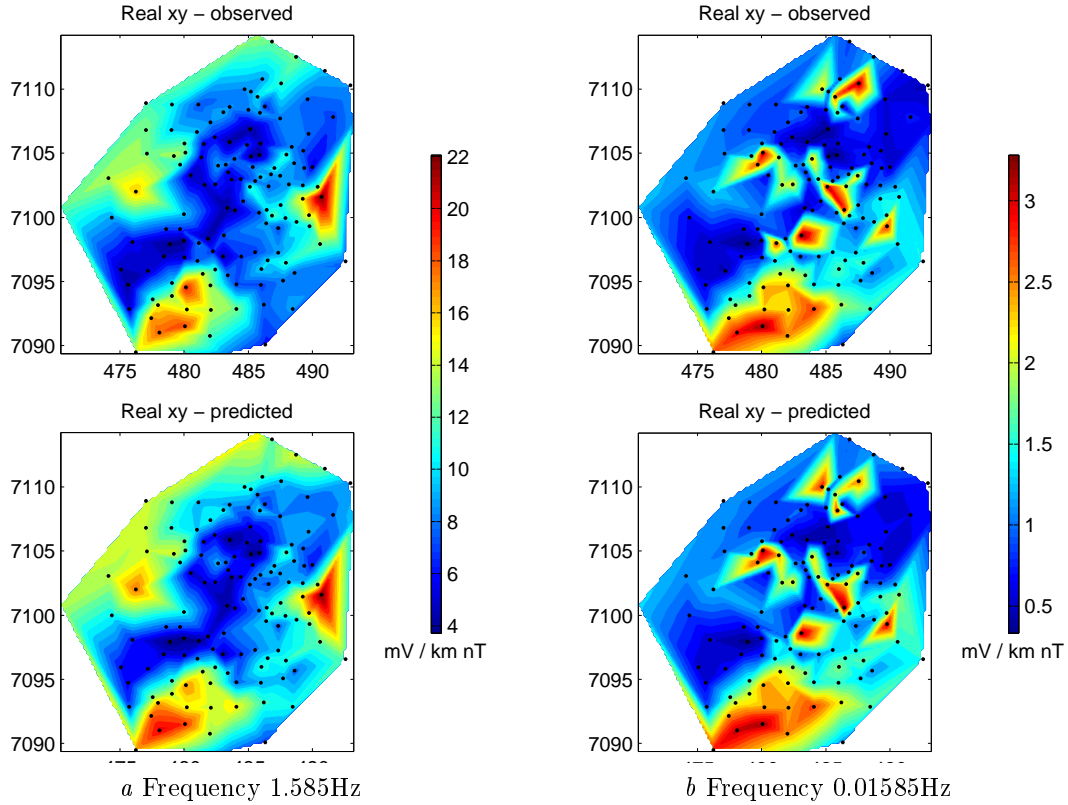


Figure 7.15: Real XY observed and predicted data of a 3D inversion for the Hengill area. Static shift correction has been applied prior to the inversion.

Figure 7.15 shows two iso-frequency maps of the observed and predicted data. For both the frequencies (Figures 7.15a and 7.10b), the predicted and the observed data agree well. Boundaries and features in the observed data are well matched in the predicted data. Other frequencies and components used in the inversion have similar fit, where the boundaries and amplitude of the anomalies agree.

7.4 Discussion of inversion results

In Figure 7.16 the observed and predicted data for sounding 0682721 is shown. The predicted data in Figure 7.16a) is calculated from the model discussed in Section 7.3.1. The fit at the higher frequencies is good, but as the observed data components split the predicted data can not follow the trend. The predicted data of both the 3D inversions without and with static shift correction fit the observed data accurately (Figures 7.16 b and c, respectively).

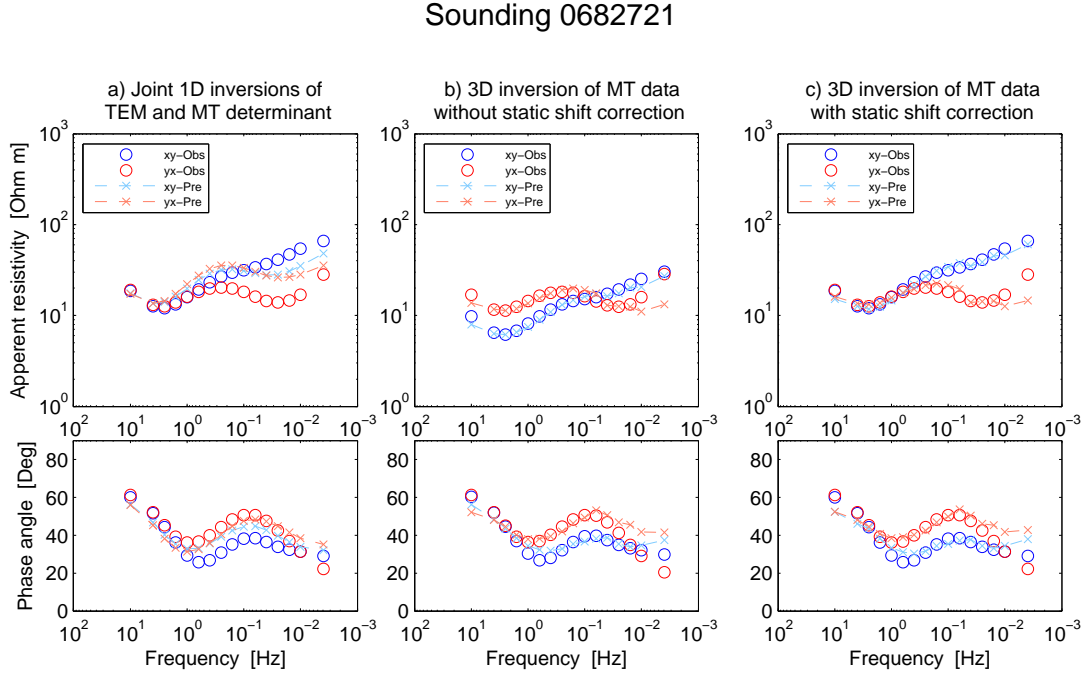


Figure 7.16: Comparison of observed and predicted data from inversion procedures, for sounding 0682721. The apparent resistivity and phase of the xy and yx components are shown. a) has the forward calculated from the 3D model interpolated from the joint 1D inversion of TEM and MT data, b) is the results of 3D inversion without static shift correction, and c) is the results of the 3D inversion with static shift correction.

In Figures 7.19, 7.17 and 7.18 the models from inversions discussed in Section 7.3 are compared. In all the figures row a) are the results from a joint 1D TEM/MT inversion, row b) are the results from 3D inversion of MT data without static shift correction and row c) are the results from 3D inversion of MT data with the static shift correction.

Cross sections West-East direction at 7103 Northing (UTM km) and South-North direction at 484 Easting (UTM km) are shown in Figures 7.17 and 7.18, respectively. The cross sections both dissect the Hengill but their location can be seen in Figure

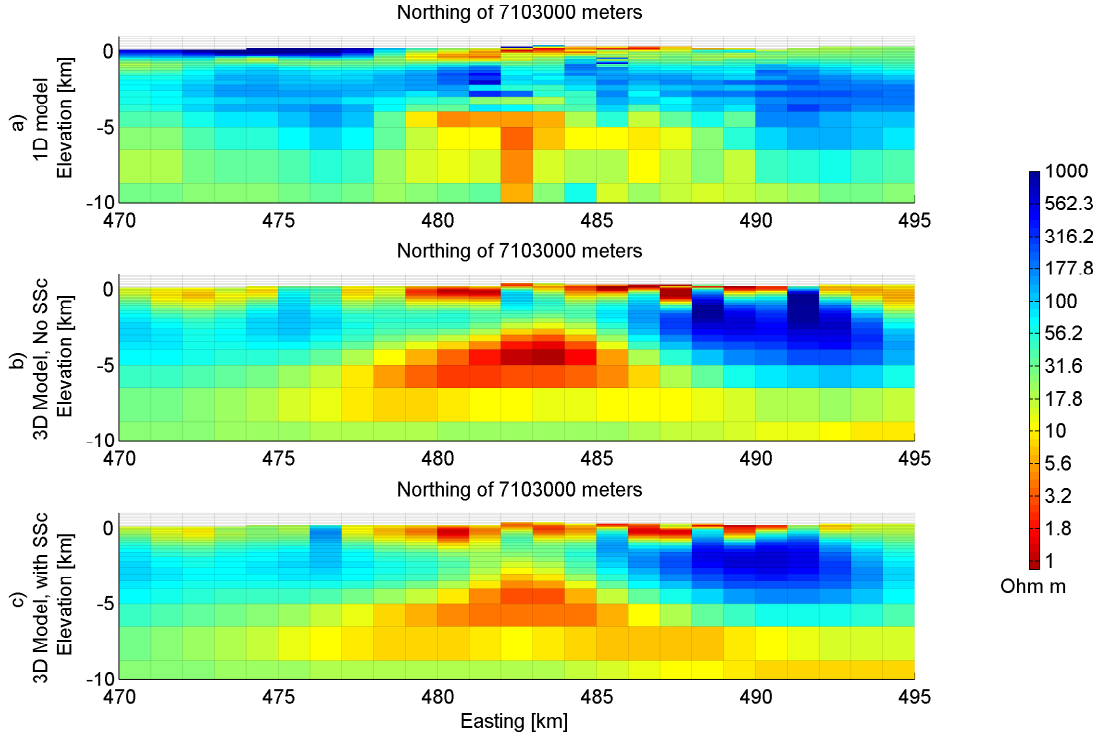


Figure 7.17: Cross section in West-East direction at 7103 Northing (km), comparing inversion models of the Hengill area. In row a) 3D model interpolated from joint 1D inversion of TEM and MT data; b) model from 3D inversion of MT data without static shift correction and c) model from 3D inversion of MT data with static shift correction.

7.2. Visual comparison of the cross sections in Figures 7.17 and 7.18 reveals general resemblance. The 3D models without and with static shift correction, sections b) and c), agree well. All edges of bodies and boundaries match well although minor differences in amplitude and shape can be seen. The 1D model has a similar resistivity distribution but the boundaries of the structures do not match with the 3D models. This is especially apparent for the deep low resistivity structure, but its location and shape does not agree with the results of the 3D inversions. The 1D inversion seems to be able to resolve the surface structure better than the 3D inversions. As seen in Chapter 6, excluding frequencies higher than 10 Hz in 3D inversion does not resolve the surface structure as well. The size of the Hengill area makes it difficult to design a mesh that accommodates the higher frequencies without increasing the total number of cells significantly.

The models are compared as iso-elevation maps at 200 m, -600 m and -4000 m in Figure 7.19. At 200 m, all the recovered models have a similar low resistivity underneath Hengill, where the size and shape of the 1D joint model and 3D model

7 Hengill geothermal area

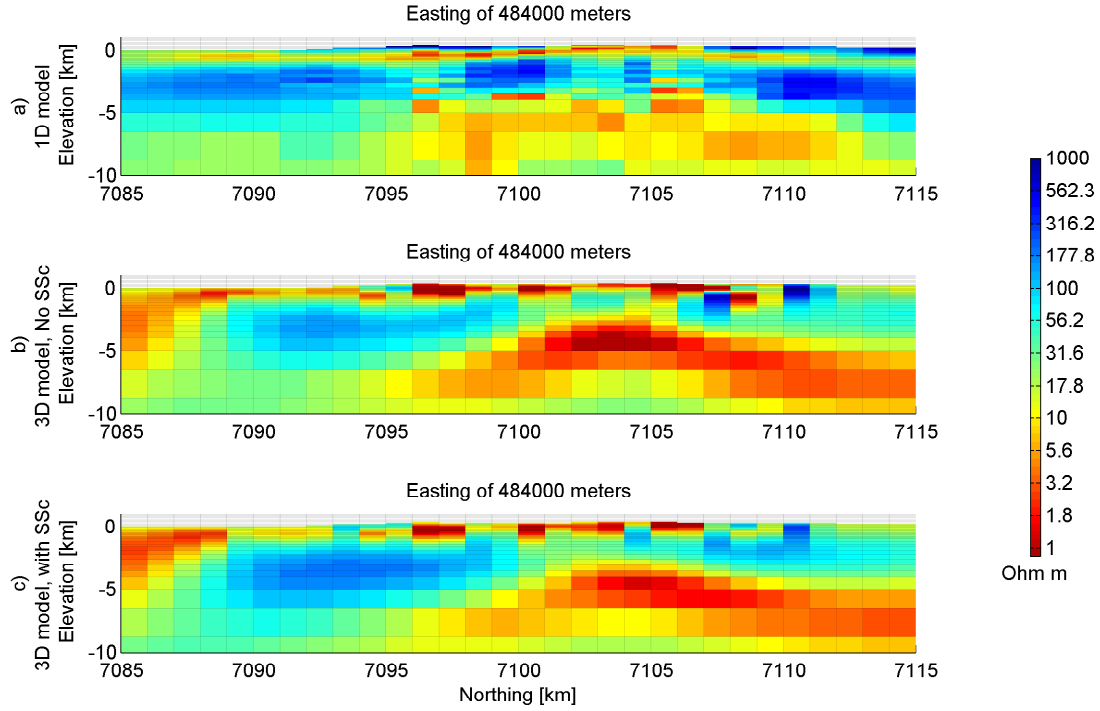


Figure 7.18: Cross section in South-North direction at 484 Easting (km), comparing the inversion models for the Hengill area. In row a) 3D model interpolated from joint 1D inversion of TEM and MT data; b) model from 3D inversion of MT data without static shift correction and c) model from 3D inversion of MT data with static shift correction.

with static shift correction is similar but 3D model without static shift correction the low resistivity covers a larger area. The surrounding resistivity in the 1D model is significantly higher, as compared to the 3D models. As seen in the inversion for the synthetic geothermal system, the range of frequencies used in the 3D inversion yield detailed resolution in the near surface. At -600 m, in the 1D model is a low resistivity coat encircling a resistivity of order of 40 Ωm . The 3D models show similar resistivity structure but both 3D model have a lot more variations in the resistivity coat. The high resistivity in the center is shaped more as a ridge in a Northwest-Southeast direction. At -4000 m, a low resistivity domes up beneath the Hengill volcano in all the models. The domes in the 3D models are better defined, with extension to the Southwest and Northwest from the Hengill volcano. The doming structure in the 1D model, has more variations and the boundaries and the shape are not as clear.

The comparison of the inversion results of EM data from the Hengill area reveals a similar resistivity structure in all cases. The low resistivity coat and resistive core,

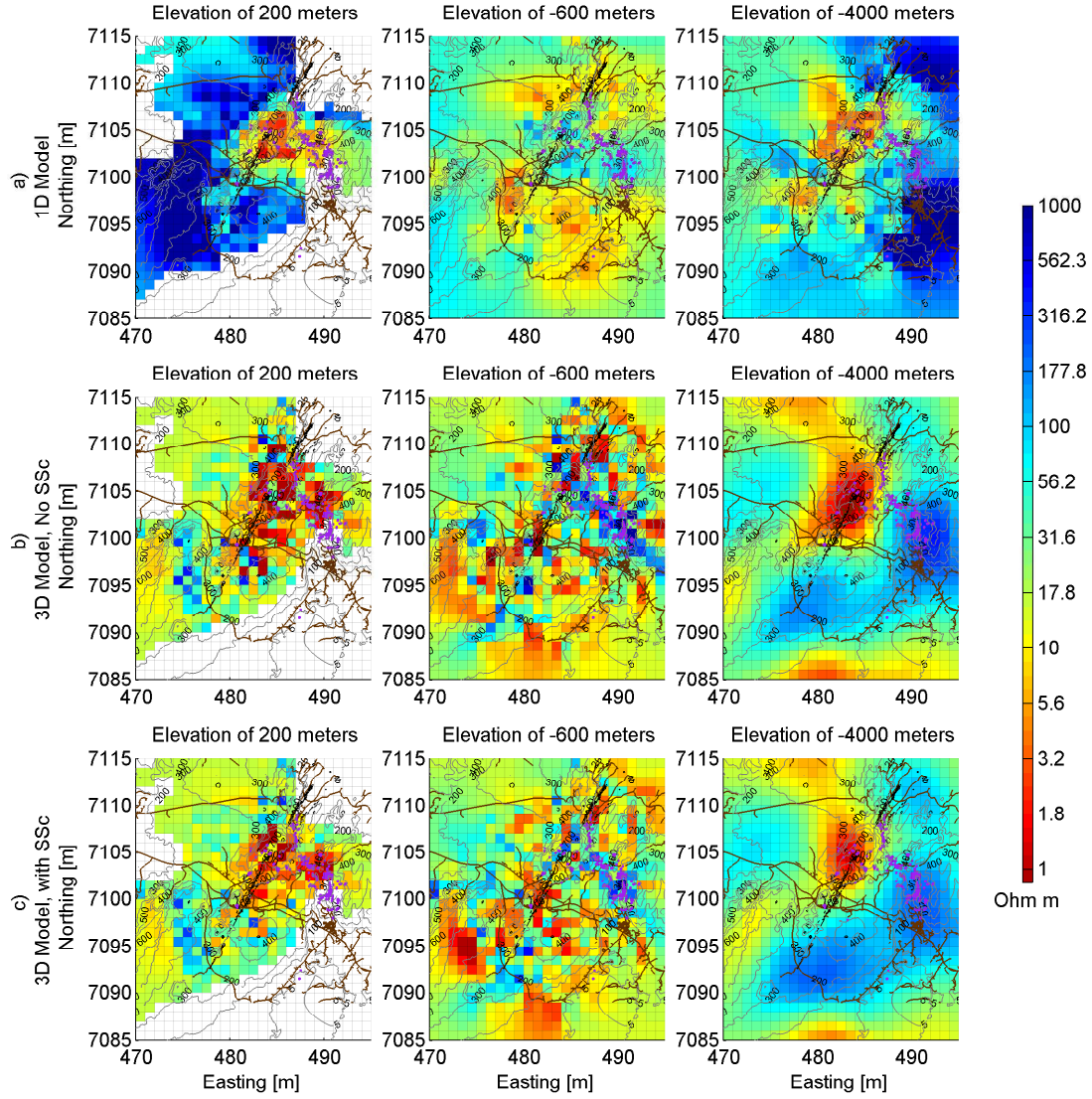


Figure 7.19: Iso-elevation maps comparing results of inversions of Hengill geothermal system. In row a) 3D model interpolated from joint 1D inversion of TEM and MT data; b) model from 3D inversion of MT data without static shift correction and c) model from 3D inversion of MT data with static shift correction. Topography is shown as light gray, main roads are shown as brown lines, volcanic craters and fissures as black lines and geothermal surface manifestations as purple dots.

as discussed in Chapter 5, are clearly seen in all the inversion results. The resolution of shallower structures is better in the model from the 1D inversions, but the 3D inversions are superior over all. The deep low resistivity layer is seen in the results from the joint 1D inversion but is better defined in both of the 3D inversion models. Similar to the inversion results of the synthetic data (Section 6.5), it is clear that the 3D inversion of MT data from the Hengill area is superior to the joint 1D inversion

in recovering resistivity structures at depth. The difference between the models from 3D inversion of the MT without and with static shift correction are not significant, where major features coincide in both models. The 3D inversion of the MT data with the static shift correction came closer to the target misfit.

In all the resulting models from the inversions of data from the Hengill area, have similar recovered resistivity structure. Low resistivity is seen the in surface at the Hengill volcano that reaches maximum size at -200 m. At that depth the low resistivity covers the area from Nesjavellir in the North, the Hengill volcano in the West, Hverahlíð in the South and Grænidalur in the East, surrounded by higher resistivity on all sides. At -200 to -400 m, a resistive ridge is seen from the Hengill volcano extending Southeast through Ölkelduháls and Grænidalur. The ridge is clearer in the model from the MT data without static shift correction (Figure 7.19). A deep low resistivity layer can be seen below most of the Hengill area. A doming is seen beneath the Hengill volcano, reaching to approximately -3000 m in all the models. The doming is smoother in the 3D models and defined as an isolated body. The surface alteration and fissures (purple dots and black lines in Figure 7.19) align with the resistivity structures. The near surface low resistivity (first column in Figure 7.19) has elongated axis Southwest-Northeast and Northwest-Southeast direction similar to the geological features. The resistive ridge at -600 m, aligns with the surface alterations areas.

The 3D inversions of the MT data from the Hengill geothermal area can be improved further. As the results from the inversion of the data from the synthetic geothermal area suggest that refining the mesh used for the inversion would likely increase resolution in the model. Adjusting the frequencies selection to include higher frequencies might allow the near surface to be resolved in more detail. In a large and complex area like the Hengill area this is a time consuming task and requires increased computations, going beyond the scope of this study. This is left as future work.

8 Conclusion

The goals of this study were to investigate the static shift problem that arises when using the MT method in geothermal exploration and compare different inversion methods. The theoretical basis of the TEM and MT methods is established first and followed by discussion of static shift problem. The computer algorithms used in the study are discussed as well as the resistivity structure of geothermal systems.

In the discussion of the static shift problem, the causes of the static shift are considered to be due to inhomogeneities and/or topography at the surface. Multiple methods to correct the static shift are discussed and using TEM soundings is confirmed to be most appropriate. TEM soundings are not affected by static shift and are widely used for static shift correction. Practical problems do come up, when the fit between TEM and MT soundings is not sufficient. In 1D inversions when static shift multipliers of each of the xy and yx components of the MT data are estimated, it often becomes necessary to exclude data from either TEM or MT data in order to improve the fit.

The results of the inversion of data from the synthetic geothermal system may be summarized as follows:

- 3D inversion of MT data is superior to joint 1D inversions of TEM and MT data. The 3D models interpolated from joint 1D inversions reproduce the original model close to the surface but at depth the 1D inversion fails to recover the resistivity structure. 3D inversions recover the surface fairly well, where boundaries between resistivity structures are seen but the recovered resistivity of the structures are different from the original model.
- Comparisons of 3D inversion of MT data without and with static shift correction do show good correlation. Applying the static shift correction prior to the inversion seems to recover models that agree better with the original model, especially when the static shift is considerable. Even without any resistivity variations in the surface there is a significant static shift induced by the low resistivity coat close to the surface.
- The design of the 3D mesh, how the data is selected and other settings of the inversion need to be considered carefully. Changing the mesh or frequen-

cies used in an inversion shows significant differences in the recovered models. Using smaller cells enhances the resolution but it increases the computation time. Changing the frequencies used for the inversion by including higher frequencies improves the recovery of resistivity structures close to the surface. Using higher frequencies often requires a finer mesh to comply with the smaller skindepths, leading to longer time needed for the inversion.

- Regardless of the setup of the inversion, all the major structures in the recovered models agree confirming their validity but interpreting detailed locations of boundaries has to be done with care. Optimizing between the accuracy and time constraints of the 3D inversion is an important task.

The results of the inversions of the TEM and MT data from the Hengill geothermal area show similar results as the inversion of the synthetic geothermal data. The models from the 3D inversion of MT data are superior to the model from the joint 1D inversions of TEM and MT data. The models from the 3D inversion of MT data without and with static shift correction recover similar structures with clear layering at the edges with defined resistivity structures around the Hengill volcano at all depths. The model interpolated from the 1D shows some resemblance to the 3D models but does not recover the resistivity structures at depth as well.

The main resistivity structures seen in all the resulting models from the Hengill area are:

Low resistivity is seen at the surface at the Hengill volcano, reaching maximum size at -200 m, covering the area from Nesjavellir in the North, the Hengill volcano in the West, Hverahlíð in the South and Grændalur in the East.

There is a high resistivity ridge from the Hengill volcano extending Southeast through Ölkelduháls and Grændalur getting closest to the surface at -200 to -400 m.

A deep low resistivity layer can be seen under most of the Hengill area. A dominant upward doming is seen beneath the Hengill volcano, reaching -3000 m.

The direction of structures in the model has a Southeast-Northwest and Northeast-Southwest, that aligns with geological features.

It is clear for both the synthetic geothermal area and the Hengill area, that 3D inversion of MT soundings in geothermal exploration have advantages over joint 1D inversion of TEM and MT soundings. The 3D inversions of the MT data from the synthetic geothermal area recovers the structures in the original model at all depths. It is clear that the setup of the inversion affects the results, therefore it is important to be critical of the results and confirm them. Running multiple inversions where

the setup is altered slightly and/or confirming the results with forward modeling should be a standard practice.

Bibliography

- Amestoy, P., Guermouche, A., L'Excellent, J., Pralet, S., 2006. Hybrid scheduling for the parallel solution of linear systems. *Parallel Computing* 32, 136–156.
- Árnason, K., 1989. Central Loop Transient Electromagnetic Soundings Over a Horizontally Layered Earth. OS-89032/JHD-06 Reykjavík, August 1989.
- Árnason, K., 2006. TEMTD - A programme for 1D inversion of central-loop TEM and MT data. short manual. Tech. rep., Iceland Geosurvey.
- Árnason, K., 2008. The Magneto-Telluric static shift problem. Tech. rep., Iceland Geosurvey, ÍSOR-08088.
- Árnason, K., Eysteinnsson, H., Hersir, G. P., 2010. Joint 1D inversion TEM and MT data and 3D inversion of MT data in the Hengill area, SW Iceland. *Geothermics* 39, 13–34.
- Arnason, K., Karlsdottir, R., Eysteinnsson, H., Flovenz, O. G., Gudlaugsson, S. T., 2000. The resistivity structure of high-temperature geothermal systems in Iceland. *Proceedings World Geothermal Congress 2000 Kyushu - Tohoku, Japan, May 28 - June 10, 2000*, 923–928.
- Árnason, K., Magnússon, I. T., 2001. Jarðhiti við Hengil og á Hellisheiði. Niðurstöður viðnámsmælinga. (Geothermal activity in Hengill and Hellisheiði. Results of resistivity surveys.) in Icelandic. Tech. rep., National Energy Authority, Geothermal division, OS-2001/091.
- Berdichevsky, M. N., Dmitriev, V. I., 2008. *Models and Methods of Magnetoellurics*. Springer-Verlag, Berlin, Germany.
- Cagniard, L., 1953. Basic theory of the magnetotelluric method of geophysical prospecting. *Geophysics* 18, 605–635.
- Constable, S. C., Parker, R. L., Constable, C. G., 1987. Occam's inversion: A practical algorithm for generating smooth models from electromagnetic sounding data. *Geophysics* 52, 289–300.
- Cumming, W., Mackie, R., 2010. Resistivity imaging of geothermal resources using 1D, 2D and 3D MT inversion and TDEM Static Shift Correction Illustrated by a

BIBLIOGRAPHY

- Glass Mountain Case History. In: Proceedings World Geothermal Congress 2010, Bali, Indonesia, 25-29 April 2010.
- deGroot Hedlin, C., 1991. Removal of static shift in two dimensions by regularized inversion. *Geophysics* 56, 2102–2106.
- Einarsson, P., 2008. Plate boundaries, rifts and transforms in Iceland. *Jökull* 58, 35–58.
- Eysteinnsson, H., Teklesenbet, A., Rosenkjær, G. K., Karlsdóttir, R., 2010. Resistivity Survey in the Alid Geothermal Area, Eritrea, a Joint Interpretation of TEM and MT data. In: Proceedings World Geothermal Congress 2010, Bali, Indonesia, 25-29 April 2010.
- Farquharson, C., Haber, E., Shekhtman, R., Oldenburg, D., 2003. Theoretical Background for the Magnetotelluric Inversion Program MT3Dinv. Tech. rep., University of British Columbia.
- Farquharson, C. G., Oldenburg, D. W., Haber, E., 2002. An algorithm for the three-dimensional inversion of magnetotelluric data. 72nd Ann. Internat. Mtg., Soc. Expl. Geophys., 649–652.
- Flóvenz, O., Spangenberg, E., Kulenkampff, J., Árnason, K., Karlsdóttir, R., Huenges, E., 2005. The role of electrical interface conduction in geothermal exploration. Proceedings World Geothermal Congress 2005 Antalya, Turkey, 24-29 April 2005, 1–9.
- Franzson, H., Gunnlaugsson, E., Árnason, K., Sæmundsson, K., Steingrímsson, B., Harðarson, B. S., 2010. The Hengill Geothermal System, Conceptual model and Thermal Evolution. In: Proceedings World Geothermal Congress 2010, Bali, Indonesia, 25-29 April 2010.
- Franzson, H., Kristjánsson, B. R., Gunnarsson, G., Björnsson, G., Hjartarson, A., Steingrímsson, B., Gunnlaugsson, E., Grímsson, G., 2005. The Hengill-Hellisheið i Geothermal Field. Development of a Conceptual Geothermal Model. Proceedings World Geothermal Congress 2005, Antalya, Turkey, 24-29 April 2005.
- Gamble, T. D., Goubau, W. M., , Clarke, J., 1979a. Error analysis for remote reference magnetotellurics. *Geophysics* 44, 959–968.
- Gamble, T. D., Goubau, W. M., Clarke, J., 1979b. Magnetotellurics with a remote magnetic reference. *Geophysics* 44, 53–68.
- Groom, R., Bailey, R., 1989. Decomposition of magnetotelluric impedance tensor in the presence of local three dimensional galvanic distortion. *Journal of Geophysical Research* 94, 1913–1925.

- H3DTD manual, 2010. H3DTD - MUMPS A Program Library for Forward Modelling of Multi-Transmitter, Time-Domain Electromagnetic Data over 3D structures. Version 1.6. Developed under the MITEM consortium Research Project. UBC-Geophysical Inversion Facility.
- Haber, E., Ascher, U. M., Aruliah, D. A., Oldenburg, D. W., 2000a. Fast simulation of 3D electromagnetic problems using potentials. *J. Comp. Phys.* 163, 150–171.
- Haber, E., Ascher, U. M., Oldenburg, D. W., 2000b. On optimization techniques for solving nonlinear inverse problems. *Inverse Problems* 16, 1263–1280.
- Hersir, G. P., Björnsson, A., 1991. Geophysical exploration for geothermal resources: Principles and application. Tech. rep., National Energy Authority, Geothermal Division.
- Hersir, G. P., Björnsson, G., Björnsson, A., 1990a. Eldstöð var og Jarðhiti á Hengilssvæði. Jarðeðlisfræðileg könnun. (Volcanism and geothermal activity in Hengill area. Geophysical exploration) in Icelandic. Tech. rep., National Energy Authority, Geothermal division, OS-90031/JHD-06.
- Hersir, G. P., Björnsson, G., Björnsson, A., Eysteinnsson, H., 1990b. Eldstöðvar og Jarðhiti á Hengilssvæði. Jarðeðlisfræðileg könnun-Viðnámsmæligögn. (Volcanism and geothermal activity in Hengill area. Geophysical exploration-resistivity data) in Icelandic. Tech. rep., National Energy Authority, Geothermal division, OS-90032/JHD-16B.
- Hersir, G. P., Vilhjálmsson, A. M., Rosenkjær, G. K., Eysteinnsson, H., Karlsdóttir, R., 2010. Jarðhitasvæðið í Krýsuvík: Viðnámsmælingar 2007 og 2008 (Krysuvik geothermal area: Resistivity surveys in 2007 and 2008) in Icelandic. Tech. rep., Iceland Geosurvey, ÍSOR-2010/025.
- Jiracek, G. R., 1990. Near-surface and topographic distortions in electromagnetic induction. *Surveys in Geophysics* 11, 163–203.
- Karlsdóttir, R., Vilhjálmsson, A. M., Eysteinnsson, H., 2008. Vonarskarð: TEM- og MT-mælingar 2007 (Vonarskarð:TEM- and MT- soundings 2007) in Icelandic. Tech. rep., Iceland Geosurvey.
- Ledo, J., Gabas, A., Marcuello, A., 2002. Static shift leveling using geomagnetic transfer functions. *Earth Planet Space* 54, 493–498.
- Mackie, R., 2002. Multi-dimensional Magnetotelluric Modeling and Inversion. Tech. rep., GSY-USA, Inc.
- Manzella, A., Ungarelli, C., Ruggieri, G., Giolito, C., Fiordelisi, A., 2010. Electrical resistivity at the Travale geothermal field (Italy). In: *Proceedings World Geothermal Congress 2010 Bali, Indonesia*, 25-29 April 2010.

BIBLIOGRAPHY

- Meju, M. A., 1996. Joint inversion of TEM and distorted MT soundings: Some effective considerations. *Geophysics* 61, 56–65.
- MT3Dinv manual, 2010. MT3Dinv - A Program Library for Inversion of Magnetotelluric Data over 3D Structures. Version 2010. Developed under the IMAGE consortium research project. UBC-Geophysical Inversion Facility.
- Nabighian, M. N., Macnae, J. C., 1991. Time-domain electromagnetic prospecting methods. Vol. 2. Soc. Expl. Geophysics.
- Newman, G. A., Hoversten, G. M., Wannamaker, P. E., Gasperikova, E., 2008. Three-dimensional Magnetotelluric Characterization of the Coso Geothermal Field. *Geothermics* 37, 369–399.
- Ogawa, Y., Uchida, T., 1996. A two-dimensional magnetotelluric inversion assuming gaussian static shift. *Geophys. J. Int.* 126, 69–76.
- Oldenburg, D., Haber, E., Shekhtman, R., 2008. Forward modelling and inversion of multi source TEM data. SEG Annual Meeting, Extended Abstracts, 559–556.
- Oldenburg, D. W., Li, Y., 2005. Near-surface geophysics, SEG investigations in geophysics. Vol. 13. Ch. Inversion for applied geophysics: a tutorial, pp. 89–150.
- Park, S., Livelybrooks, D. W., 1989. Quantitative interpretation of rotationally invariant parameters in magnetotellurics. *Geophysics* 54, 1483–1490.
- Pellerin, L., Johnston, J. M., Hohmann, G. W., 1996. A numerical evaluation of electromagnetic methods in geothermal exploration. *Geophysics* 61, 121–130.
- Raharjo, I. B., Maris, V., Wannamaker, P. E., Chapman, D. S., 2010. Resistivity Structures of Lahendong and Kamojang Geothermal Systems Revealed from 3-D Magnetotelluric Inversions, A Comparative Study. In: *Proceedings World Geothermal Congress 2005 Antalya, Turkey, 24-29 April 2005*.
- Ranganayaki, R. P., 1984. An interpretive analysis of magnetotelluric data. *Geophysics* 49, 1730–1748.
- Rosenkjær, G. K., Karlsdóttir, R., 2008. MT-mælingar á Reykjanesi 2008 (MT-soundings in Reykjanes 2008) in Icelandic. Tech. rep., Iceland Geosurvey, ÍSOR-2009/002.
- Sasaki, Y., 2004. Three-dimensional inversion of static-shifted magnetotelluric data. *Earth Planets Space* 56, 239–248.
- Sasaki, Y., Meju, M. A., 2006. Three-dimensional joint inversion for magnetotelluric resistivity and static shift distributions in complex media. *Journal of Geophysical Research* 111, B05101.

- Sigmundsson, F., Einarsson, P., Rögnvaldsson, S., Foulger, G. R., Hodgkinson, K. M., Thorbergsson, G., 1997. The 1994-1995 seismicity and deformation at the Hengill triple junction, Iceland: Triggering of earthquakes by minor magma injection in a zone of horizontal shear stress. *J. Geophys. Res.* 102(B7), 15151–15161.
- Simpson, F., Bahr, K., 2005. *Practical MagnetoTellurics*. Cambridge University Press, Cambridge, United Kingdom.
- Spies, B. R., Frischknecht, F. C., 1991. *Electromagnetic Sounding*. Vol. 2. Soc. Expl. Geophysics.
- Spitzer, K., 2001. Magnetotelluric static shift and direct current sensitivity. *Geophys. J. Int.* 144, 289–299.
- Sternberg, B., Washburne, J. C., Pellerin, L., 1988. Correction for the static shift in magnetotellurics using transient electromagnetic soundings. *Geophysics* 53, 1459–1468.
- Tikhonov, A., 1950. Determination of the electrical characteristics of the deep strata of the earth's crust. *Dokl. Akad Nauk SSSR* 73 (2), 295 pp.
- Uchida, T., 2005. Three-Dimensional magnetotelluric investigation in geothermal fields in Japan and Indonesia. In: *Proceedings World Geothermal Congress 2005 Antalya, Turkey, 24-29 April 2005*.
- Ussher, G., Harvey, C., Johnstone, R., Anderson, E., 2000. Understanding the resistivities observed in geothermal systems. *Proceedings World Geothermal Congress 2000 Kyushu - Tohoku, Japan, May 28 - June 10, 2000*.
- Vozoff, K., 1991. *Electromagnetic Methods in Applied Geophysics*. Vol 2, Application. Soc. Expl. Geophys., Tulsa, OK., 972 pp., Ch. The magnetotelluric method.
- Wright, P. M., Ward, S. H., Ross, H. P., West, R. C., 1985. State-of-the-art geophysical exploration for geothermal resources. *Geophysics* 50, 2666–2699.